Microwave Scattering Model for Nonuniform Forest Canopies

by

Pan Liang

A dissertation submitted in partial fulfillment
of the requirements for the degree of
Doctor of Philosophy
(Electrical Engineering)
in The University of Michigan
2005

Doctoral Committee:

Professor Mahta Moghaddam, Co-Chair
Research Scientist Leland E. Pierce, Co-Chair
Professor Fawwaz T. Ulaby
Professor Andrew E. Yagle

ACKNOWLEDGEMENTS

TABLE OF CONTENTS

LIST OF FIGURES

Figure

LIST OF TABLES

Table

Chapter I

INTRODUCTION

1.1 Motivation

Synthetic aperture radar (SAR) systems are capable of producing very high resolution images of the earth, since microwaves have the ability of deeper penetration than optical waves and are weather independent, they are powerful tools to investigate and monitor the earth's environment. Spaceborne and airborne SARs are frequently employed for civilian and military applications such as land cover monitoring and target detection. These sensors produce an enormous amount of data that must be interpreted and utilized. With the development of multi-frequency, polarimetric and interferometric techniques in SAR imaging systems, SAR images with higher spatial resolution and multi-scales are acquired. The effective use of information within SAR images is essential to investigate and monitor the earth's geophysical parameters globally and locally.

Forests are a major part of the earth vegetation coverage. They store a higher proportion of carbon in the form of biomass and contribute greatly to exchange of gases and energy between the atmosphere and the surface. The growth and distribution of forests plays an important role in the global carbon cycle. Characterizing forest canopy properties such as biomass, tree height, and density over large areas is therefore important in understanding and modeling forest state, condition and functioning [68]. Studies estimate that tropical land-use change accounted for approximately one third of the increase of the atmospheric carbon dioxide content [32]. The repetitive global coverage and ground inaccessibility make remote sensing a practical tool to study forest ecosystem dynamics because of the provision of consistent datasets at local to global scales and at appropriate spectral, spatial and temporal resolutions. There are various types of remote sensing instruments that can be used to study forests, each for a different purpose. Landsat data have been used to estimate secondary growth rates and biomass accumulation rates [2]. Although optical/hyperspectral datasets are useful for forest mapping and species/community discrimination, observations are restricted by cloud cover and time of day and the data relates largely to the surface of materials. By contrast, microwave remote sensing has the advantage of penetrating cloud and dense vegetation canopies and microwave frequencies are sensitive to many forest parameters. SAR allows all-weather and night-time observations at high resolution and a range of frequencies and polarizations. Furthermore, active microwaves can provide information on the vertical depth of forests, including the dielectric properties of tree components and their geometric structure.

Over the past two decades, research has increasingly focused on the use of SAR for retrieving biomass and other vegetation properties [18, 33, 40, 48, 49, 55, 56, 67, 70]. Studies have demonstrated the usage of SAR data in different configurations to map vegetation biomass over large regions. However, retrieval using SAR backscattering coefficients is limited by saturation levels of biomass, which vary from 30 Mg/ha to 200 Mg/ha with frequency and polarization as well as community composition and structure [18, 33, 49, 67]. More recently, however, efforts have been made to understand and quantify the relationship between SAR data and the properties of forest components with a view to raising the levels at which biomass and other structural attributes can be retrieved [48, 56, 70].

Many microwave scattering models have been developed to study how microwave signal interacts with forest components and retrieve the forest parameters from SAR measurement. However, the existing models have been developed for monostatic (backscattering) radar systems and therefore are insufficient for studying the bistatic RCS of forest canopies. Moreover, these models are not applicable to forest stands of mixed species composition and structure where multiple layers occur such as the overstory, understory and shrubs.

It is also important to study SAR's response to the inhomogeneity of forests in the horizontal direction. The pixel-level based image models and processing tools are insufficient to represent the target's inhomogeneity in the images. Texture analysis has drawn more interest lately and is becoming increasingly important. Texture of SAR images is caused by the spatial variation of the imaged objects. It is an important property of natural and man-made targets such as rain forests and urban areas, especially in high resolution images; the property of the region is often more important than their individual positions, for example, regions of cultivated vegetation, trees planted in rows and houses along streets. The spatial average over a region does not capture the relevant information optimally. Thus, texture information can generate more accurate understanding of the characteristics of the interested region, as a result, higher accuracy of land cover classification can be achieved.

To explore the advantages of bistatic radars, a bistatic forest scattering model is first developed to simulate bistatic scattering coefficients from forest canopies, the model is based on Michigan Microwave Canopy Scattering (MIMICS) model and uses radiative transfer theory. Furthermore, the bistatic configuration is included in a multi-layer canopy scattering model for mixed species forests, which is developed to account for the complexity of forests in the vertical direction. A Part of this dissertation analyzes and simulates a relatively simple and effective texture model — correlation length and develops a blind deconvolution approach to estimate correlation length of SAR texture, which can be applied to study forest structures' non-uniformity in the horizontal direction. A coherent SAR texture simulator is also utilized to analyze the formation of SAR texture and study SAR image and texture models.

1.2 Background

To better understand how microwave signals interact with forest and other vegetated and non-vegetated components and to thereby assist forest parameter retrieval from SAR measurement, many microwave scattering models have been developed [9, 19, 34, 38, 44, 62, 66, 81, 86]. These models treat forest canopies as infinite horizontal layers over a ground surface. Two usual approaches — field approach and discrete approach are mostly used to model random scattering media. The field approach models the permittivity of the random medium as a continuous function of positions which has a mean value (background) and a a fluctuating part (small particles), this approach is appropriate for weakly scattering media where the fluctuation is small compared to the mean value such as ice or sea water [58]. For forest canopies, a discrete approach is appropriate with respect to the canopy component size, density and microwave frequency. The canopy is characterized as a discrete random medium consisting of tree components (i.e., trunks, branches and foliage) that act as single microwave scatterers. A typical two layer canopy model is often used in these scattering models. Branches and foliage make up the crown layer, underneath that is the trunk layer made of vertical trunks. A rough surface model is used for the ground. These models have been modified and enhanced for various applications and vegetation types. In some crop canopy models, only one layer is considered; at low frequencies (i.e., L- or P-band), foliage is ignored in some models [65, 71]. Modified solutions also introduce gap or cell structures for forests with discontinuous [50, 80, 81].

The majority of models fall into two categories by their developing techniques: (1) Distorted Born Approximation(DBA) [44,72,73] and (2) Radiative Transfer (RT) theory [62, 66, 86]. The DBA approach is an approximate solution of Maxwell's equations of the scattering medium and includes the coherent effect of fields. The RT theory solves energy transport RT equations in the random medium and ignores coherent effects. Most models based on RT theory solve the equation by an iterative approach; some use the Discrete Ordinate and Eigenvalue Method (DOEM) and utilize multiple discretized canopy layers [62].

MIMICS [86] have been developed to model microwave backscatter from vegetation canopies. It represents a first order solution of the RT equations. and uses a crown-trunk canopy model over a ground surface. Discrete approach is applied to model canopy components. MIMICS was developed in three stages. The first version, MIMICS I, is the first order solution and works with a continuous crown layer. MIMICS II is designed to incorporate discontinuous crown layers as well as trunk surface roughness. MIMICS III is proposed to extend the previous versions to second or higher order solutions. Among them, MIMICS I has been mostly implemented and validated. In this dissertation, MIMICS I is referred to MIMICS.

Many methods and models to describe and estimate SAR image texture have been developed. Among them are histogram estimation [37, 85] , image correlation length estimation [37,85], second-order gray-level co-occurrence matrix(GLCM) method [28, 85], lacunarity index [17,54,63], wavelet decomposition [59] and Markov random field (MRF) models [12, 15, 24, 42, 75].

One simple and effective texture model is to fit the pixel values into different histograms [60, 61]. For a homogeneous area, the intensity values of single look SAR images fit in a negative exponential distribution, and their amplitude values fit in a Raleigh distribution, both are characterized by one parameter corresponding to the average radar cross section(RCS). However, when target texture exits, in order to represent the spatial variations of natural scenes, some probability distribution functions(PDF) with two or more parameters have been proposed such as K-distribution, log-normal and Weibull distribution. The additional degree of freedom allows them to represent different contrast in data and the contrast has already been identified as a potential texture discriminant. Many researchers have applied the PDF estimation method on SAR image classification and segmentation processes. A PDF estimation of the normalized texture measure was proposed [60] to classify SAREX-92 data from the Amazon rain forest.

Image correlation length is another effective parameter proposed to represent the texture characteristics of images, it is commonly used in rough surface modeling. It has been shown that the correlation length differs in real SAR images. Ulaby *et al* in [85] shows that images of water surfaces have the shortest correlation length, and images of forest have the largest correlation length while those of urban areas have the medium correlation length. Kurosu *et al* in [37] shows that the texture autocorrelation functions distinguish rice and grass, which are not separable by the first order statistics.

GLCM and lacunarity index are also popular methods to characterize SAR texture. GLCM measures the co-occurrence probabilities of two specific gray-levels at specific positions in terms of the relative direction and distance. Usually applied on binary images, lacunarity measures the deviation of a geometric object from translational invariance at multi-scales. Homogeneous images have lower lacunarity.

With the development of much more capable computers, Markov random field (MRF) texture models have received increasing attention. In these models, the image is described by Markov chains defined in terms of conditional probabilities associated with spatial neighborhoods. There are many MRF models that have been proposed such as Gibbs model, Gaussian model, binomial model, and Gamma model. Many groups have demonstrated MRF models in simulating the remote sensing image texture successfully. The parameters estimated from MRF models are used in image classification, segmentation and registration. The major problem with the MRF models is the high computational complexity.

The methods and models introduced above have been major parts of SAR image processing techniques. There are numerous studies to extract and understand SAR texture. For example, The land-cover classification accuracy based on first order statistical radar cross section (RCS) can be as high as 72% while the second order texture statistics provided a classification accuracy of 88% for Seasat SAR imagery of Oklahoma as shown in [85]. It has been reported that texture is used to classify different tree stands. [37] shows the classification accuracy of JERS-1 single look images was improved by 29% by adding texture features based on the second order statistics.

Like the indeterminate nature of image texture itself, the choice of SAR texture models depends on many factors such as scene properties, sensor, noise level, pixel resolution and scale and computational cost. In this work, we analyze the formation of SAR texture and build a coherent SAR texture simulator to investigate the optimal texture models that are relatively simple yet effective for SAR imagery.

1.3 Overview

The goal of this study is to develop microwave scattering models for nonuniform forest canopies and apply them to actual forest stands, and the models' simulation results are validate by real SAR measurement data. Major contributions include:

① Extend MIMICS to a bistatic microwave canopy scattering model.

② Using a multi-layer canopy model to represent the mixed species forest canopies, which also contains overlapping layers and a tapered trunk model.

③ Build and solve multi-layer radiative transfer equation and implement a bistatic multilayer canopy scattering model.

④ Compare applications of correlation length model and MRF model to SAR images and use a blind deconvolution method to estimate the texture correlation length from SAR images.

⑤ Build a SAR texture simulator to analyze formation of SAR texture, compare the statistical SAR image model and direct coherent summation simulation model.

This dissertation is arranged as follows:

In Chapter II, after a brief overview of the RT theory and the backscattering version of MIMICS on which the bistatic model is based in Section 2.1, the development of Bi-MIMICS is described in Section 2.2. The application of the model is presented next: Section 2.3 describes canopy parameters and bistatic geometry setup while the application of Bi-MIMICS to selected canopies and the simulation results are discussed in Section 2.4. Finally, the chapter is conclude in Section 2.5.

In Chapter III, the first section provides the background and motivation of developing Multi-MIMICS. Section 3.2 presents the multi-layer canopy model and solves RT equations while Section 3.3 analyzes the the first order Multi-MIMICS scattering mechanisms and model's applicability. The implementation of Multi-MIMICS is then presented in Section 3.4 and Section 3.5 summarizes the chapter.

Chapter IV consists of the application of Multi-MIMICS to real mixed forests and analysis of the simulation results. Acquisition of forest data and processing of SAR measurement from the test site are described in Section 4.1. Section 4.2 compares the backscattering coefficients simulated by Multi-MIMICS and MIMICS models and actual SAR data, the multi-layer scattering model is validated by radar measurement. Multi-MIMICS's capabilities and limitations of the models are discussed in Section 4.3. Section 4.4 is the summarization.

In Chapter V, the background of SAR texture is first introduced in in Section 5.1, then Section 5.2 provides the overview about the conventional multiplicative SAR image model and its first and second order statistics. Image correlation length is the texture model of our interest while other well known texture models are also tested as a supplement measurement. Section 5.3 compares two texture model's performance on actual SAR images from tropical forests and suggests correlation length is a simple and effective model for analyzing texture of remote sensing images. A blind deconvolution algorithm developed to estimate the SAR texture correlation is presented in Section 5.4 and Section 5.5 concludes the chapter.

In Chapter VI, Section 6.1 introduces two types of SAR image simulator through statistic approach and direct coherent summation approach. Physical formation of SAR texture is analyzed in Section 6.2, which provides the theoretical background for the coherent texture simulator. Section 6.3 describes the coherent SAR simulator and presents simulation results for different target textures. The result is discussed and summarized in Section 6.4.

Finally, Chapter VII concludes the thesis and proposes the future work.

Chapter II

BISTATIC MICROWAVE CANOPY SCATTERING MODEL

A bistatic forest scattering model is developed to simulate scattering coefficients from forest canopies. It is based on MIMICS (hence called Bi-MIMICS) and uses radiative transfer theory, where the first order fully polarimetric transformation matrix is used. Bistatic radar systems offer advantages over monostatic radar systems because of the additional information provided by the diversity of the geometry. Seven bistatic scattering mechanisms and one specular scattering mechanism are included in the first order Bi-MIMICS solution, and they represent the extinction, scattering and reflection processes of the propagating wave through the canopy. By simulating the forest canopy scattering from multiple viewpoints, we can better understand how the forest scatterers' shape, orientation and density and permittivity affect the canopy scattering.

Bi-MIMICS is parametrized using selected forest stands with different canopy compositions and structure. The simulation results show that bistatic scattering is more sensitive to forest biomass changes than backscattering. Analyzing scattering contributions from different parts of the canopy gives us a better understanding of the microwave's interaction with the tree components. The ground effects can also be studied. Knowledge of the canopy's bistatic scattering behavior combined with additional SAR measurements can be used to improve forest parameter retrievals. The simulation results of the model provide the required information for the design of future bistatic radar systems for forest sensing applications.

In this chapter, Section 2.1 provides a brief background of radiative transfer theory and overview of the backscattering version of MIMICS on which the bistatic model is based. The development of Bi-MIMICS is then presented in Section 2.2. Section 2.3 describes canopy parameters and bistatic geometry setup. The application of Bi-MIMICS to selected canopies and the simulation results are discussed in Section 2.4 and Section 2.5 concludes the chapter.

2.1 Introduction and Background

2.1.1 Forest Canopy Parameters

The Marrakesh Accords define forest by three criteria in [1], they are area of region, tree cover over the area (percent) and tree height [68].

Definition 2.1.1 *A minimum area of land of 0.05 $\sim$ 1.0 ha with tree crown cover, or equivalent stocking level, of more than 10% $\sim$ 30% and containing trees with the potential to reach a minimum height of 2 $\sim$ 5 m at maturity is defined as forest. A forest may consist either of closed forest formations where trees of various storeys and undergrowth cover a high proportion of the ground or open forest.*

The Marrakesh Accords allow countries under the Kyoto Protocol to choose their own parameters within the ranges described above.

Tree crown is the upper part of a tree, which includes branches and foliage. Tree trunk is the main woody stem of a tree above the ground. Crown and trunk are two major structures of forests. To develop microwave scattering models for forest canopies, both the geometric parameters and physical parameters representing the canopy need to be defined.

Canopy geometric parameters are defined in two levels. At canopy level, most important parameters are canopy density (i.e. number of trees per unit area); Crown shape, crown radius and crown depth; Trunk height; So is the ground roughness.

At tree level, there are four types of canopy composition need to be specified. For branches and needles, volume density (i.e. number of branches or needles per unit volume) as well as distribution of the size (stem length and stem radius) and orientation (elevation and azimuth angle) should be provided; For leaves, the size information refers to the distribution of thickness and radius of the leaves. Density and orientation distribution are also needed for leaves; Distribution of trunk's orientation and radius are important too.

Physical parameters are the dielectric constant of every parts of the canopies. Dielectric constants of the four canopy components are related to their moisture content, environment temperature and bulk density. The permittivity of the ground surface is decided by surface type (soil, snow, water), moisture content, soil composition (soil, sand, tilt) and environment temperature.

2.1.2 Canopy Scattering Model and Motivation

Although early stage radars were bistatic systems, they were quickly replaced by monostatic system for practical usage in means of instrument building. Nowadays, most SARS for earth resources applications are backscattering radar systems such as JERS, EOS, RADARSAT, AirSAR, ENVISAT/ASAR, PALSAR. However, over the last decade, increasing attenuation has been paid to bistatic radar systems partly due to the advances in communication and processing technologies, they began to reclaim the arena. Studies and experiments have been reported for bistatic system development and algorithms [53, 76]. Bistatic radar measurements have been taken in the laboratory either using radars on two separate platforms or using a monostatic radar with a reflective plane setup [5, 20, 30, 74, 83]. Some systems have also explored the usage of existing satellite or communication channels as the transmission signals [26, 89].

Because bistatic geometry provides additional information which can't be acquired through backscattering measurement, bistatic/multistatic radar systems offer advantages over monostatic radar systems in the areas of target detection and identification. Targets designed to minimize backscattering Radar Cross Section (RCS) or scattering coefficient (σ^0) may demonstrate a large bistatic RCS, which improves the counter-stealth ability of radar systems. Using passive receivers is important for military applications since the passive receivers are undetectable.

The existing canopy scattering models, however, have been developed for monostatic (backscattering) radar systems and therefore are insufficient for studying the bistatic RCS of forest canopies. To explore the advantages of bistatic radars, our research has focused on the development of a bistatic model, herein referred to as the Bistatic Michigan Microwave Canopy Scattering model (Bi-MIMICS). As the name suggests, the model is based on the original backscattering MIMICS [86]. As with its predecessor and other models, the RT-theory-based canopy scattering model utilizes the discrete scatterer approach and an iterative algorithm to solve the RT equations.

The development of Bi-MIMICS is motivated by the need to design new bistatic systems. The bistatic response of forests can be used in vegetation classification and parameter estimation. By applying the bistatic model to forest canopies at various observation angles, the simulation results enhance the understanding of how a forest's structure, scatterer orientation, density and diversity affect the scattering measurements. As a result, better understanding of the microwave scattering mechanisms of tree components are obtained, which aid studies such as communication channel sensitivity in forested areas as well as detection of targets under the trees. Bi-MIMIC can also be used to study the effects of the underlying ground on total canopy scattering. The simulation results of the model offer the needed information for the design of future bistatic radar systems for forest sensing applications. In this chapter, we apply Bi-MIMICS to a number of canopies at different angles, frequencies, and polarizations. The simulated bistatic RCS is examined for the canopy's scattering signature and the dependency on angle, frequency, and polarization.

2.1.3 Radiative Transfer Theory

In a medium containing random particles, radiating wave energy interacts with the medium by absorption, scattering and emission. The quantity intensity is used to characterizing the radiation field. The definition of intensity has several similar but different forms. In this dissertation, the term intensity is denoted by $\mathbf{I}$ and defined as follow.

Definition 2.1.2 *Intensity is the flux of energy in a given direction per second per unit solid angle per unit area perpendicular to the given direction. Its unit is* $J\, t^{-1}\, sr^{-1}\, m^{-2}$.

In Figure 2.1, $\mathrm{d}\Omega$ is the given direction, which has an angle θ with respect the normal direction n of the unit area $\mathrm{d}A$, the energy falls on the unit area $\mathrm{d}A$ from the direction $\mathrm{d}\Omega$ in the unit time interval $\mathrm{d}t$ is

$$\varepsilon = \mathbf{I} \cos\theta\, \mathrm{d}t\, \mathrm{d}\Omega\, \mathrm{d}A \tag{2.1}$$

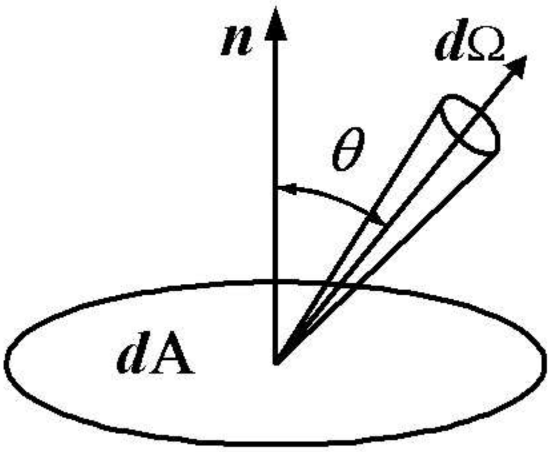

Figure 2.1: Definition of intensity. dΩ is the given direction, which has an angle θ with respect the normal direction n of the unit area dA.

The intensity per frequency interval is called specific intensity. Radiative transfer (RT) theory solves energy transport equations in the random medium by utilizing two processes — extinction and emission to describe the change of propagating microwave intensity in a given direction caused by the medium [8, 50, 85].

Definition 2.1.3 *Extinction refers to the decrease in magnitude of wave intensity along the propagation path either by absorption or scattering into other directions.*

Definition 2.1.4 *Emission refers to the increase in magnitude of wave intensity along the propagation path due to both emission and scattering into the propagating directions from other directions.*

The self thermal emission from the canopy is negligible compared to other sources at the frequencies used in active radar remote sensing.

The electric filed vector $\vec{\mathbf{E}}$ of a plane wave propagating in a medium can be presented by

$$\vec{\mathbf{E}} = (E_v\hat{\mathrm{v}} + E_h\hat{\mathrm{h}})e^{j\vec{k}\cdot\vec{r}} \tag{2.2}$$

where $\vec{k}$ is the wave vector of the field and $\vec{r}$ is the observation position vector. The terms $\hat{\mathrm{v}}$ and $\hat{\mathrm{h}}$ are the unit vertical and horizontal polarization vectors while E_v and E_h are the vertical and horizontal polarized parts of the electrical field vector, respectively. According to Equation (2.2), the polarization state of the intensity is represented by the modified Stokes vector as follow

$$\mathbf{I} = \begin{bmatrix} I_v \\ I_h \\ U \\ V \end{bmatrix} /\eta = \begin{bmatrix} |E_v|^2 \\ |E_h|^2 \\ 2\Re(E_v E_h^*) \\ 2\Im(E_v E_h^*) \end{bmatrix} /\eta \tag{2.3}$$

where the quantity η is the intrinsic impedance.

The incident electrical field $\vec{E_i}$ is scattered by a particle trough a 4×4 scattering matrix S to generate the scattered electrical field $\vec{E_s}$ as

$$\begin{bmatrix} E_{sv} \\ E_{sh} \end{bmatrix} = \frac{e^{jkr}}{r} \begin{bmatrix} S_{vv} & S_{vh} \\ S_{hv} & S_{hh} \end{bmatrix} \begin{bmatrix} E_{iv} \\ E_{ih} \end{bmatrix} \tag{2.4}$$

Therefore through mathematic operations (Equation (2.3)), the intensity scattered $\mathbf{I}_s(\theta_s, \phi_s)$ by a single particle can be related to the incident intensity $\mathbf{I}_i(\theta_i, \phi_i)$ by the modified Mueller matrix $\mathcal{L}_m$

$$\mathbf{I}_s(\theta_s, \phi_s) = \frac{1}{r}\mathcal{L}_m(\theta_s, \phi_s; \theta_i, \phi_i; \theta_k, \phi_k)\mathbf{I}_i(\theta_i, \phi_i) \tag{2.5}$$

where (θ_i, ϕ_i) is the incident angle and (θ_s, ϕ_s) defines the scattering angle. (θ_k, ϕ_k) is the orientation of the particle and r is the distance of the scattered intensity from the particle. The modified Mueller matrix $\mathcal{L}_m$ is defined by the electrical field scattering matrix S of the particle as in Equation (2.6).

$$\mathcal{L}_m = \begin{bmatrix} |S_{vv}|^2 & |S_{vh}|^2 & \Re(S_{vh}^* S_{vv}) & -\Im(S_{vh}^* S_{vv}) \\ |S_{hv}|^2 & |S_{hh}|^2 & \Re(S_{hh}^* S_{hv}) & -\Im(S_{hv} S_{hh}^*) \\ 2\Re(S_{vv} S_{hv}^*) & 2\Re(S_{vh} S_{hh}^*) & \Re(S_{vv} S_{hh}^* + S_{vh} S_{hv}^*) & -\Im(S_{vv} S_{hh}^* - S_{vh} S_{hv}^*) \\ 2\Im(S_{vv} S_{hv}^*) & 2\Im(S_{vh} S_{hh}^*) & \Im(S_{vv} S_{hh}^* + S_{vh} S_{hv}^*) & \Re(S_{vv} S_{hh}^* - S_{vh} S_{hv}^*) \end{bmatrix} / \eta \tag{2.6}$$

For a medium containing random particles, the waves scattered from these particles are random in phase under the RT theory assumption and therefore, the total scattered wave energy can be calculated by incoherent summation over all the particles.

The case $S_{hv} = S_{vh} = 0$ indicates that the medium doesn't depolarize the incident electric field. Some scattering model [43, 44] sets these two quantities to be zero as they assume the summation over a large number of independent scatterers would result in zero, which serves as a means to reduce the computational coat. However, We don't make this assumption in our models, the operation of matrices are conducted through eigen value/vector approach. Therefore, depolarization of the medium is included in the models.

In a semi infinite medium located in the half space $z > 0$, the integral form of the vector RT equation at position (θ, ϕ, z) is [50]

$$\mathbf{I}(\mu, \phi, z) = e^{-\boldsymbol{\kappa} z/\mu} \mathbf{I}(\mu, \phi, 0) + \int_0^z e^{-\boldsymbol{\kappa}(z-z')/\mu} \mathcal{F}(\mu, \phi, z') \mathrm{d}z' \tag{2.7}$$

where $\boldsymbol{\kappa}$ is the extinction matrix of the medium, and $\mathcal{F}$ is the source function. $\mu = \cos\theta$ and is not to be mistaken as the permeability of the medium. The first item is the intensity at the boundary $\mathbf{I}(\mu, \phi, 0)$, reduced in magnitude by the factor $e^{-\boldsymbol{\kappa} z/\mu}$ as it propagates through the distance z/μ in the direction (μ, ϕ) due to the extinction by the medium. The second term accounts for the scattering by the medium along the propagation path. The source function has the form

$$\mathcal{F}(\mu, \phi, z') = \int \mathcal{P}(\theta, \phi; \theta_i, \phi_i)\mathbf{I}(\mu_i, \phi)\mathrm{d}\Omega_i \tag{2.8}$$

In the above equation, $\mathcal{P}(\theta, \phi; \theta_i, \phi_i)$ is the phase matrix transferring the incident intensity in the direction (θ_i, ϕ_i) to the scattered intensity in the direction (θ, ϕ).

For a medium containing one type of scatterers whose size s_k and orientation (θ_k, ϕ_k) can be described by certain distribution $f(s_k; \theta_k, \phi_k)$, its phase matrix is given by

$$\mathcal{P}(\theta_s, \phi_s; \theta_i, \phi_i) = N_k \int\int\int f(s_k; \theta_k, \phi_k)\mathcal{L}_m(\theta_s, \phi_s; \theta_i, \phi_i; \theta_k, \phi_k)\mathrm{d}s_k\mathrm{d}\theta_k\mathrm{d}\phi_k \tag{2.9}$$

where N_k is the scatterer number density. If the medium contains more type of scatterers, the total phase matrix of the medium is the summation of phase matrices over all types [50].

The extinction matrix of a medium containing random scatterers [50] is given by Equation (2.10) and (2.11). Where K is the total type of scatterers in the medium, N_k is the number density of type k and $\langle S_{pqk}(\theta_s, \phi_s; \theta_i, \phi_i; \theta_k, \phi_k)\rangle_k$ is the average scattering amplitude coefficient of type k scatterers at pq polarization, and k_0 is the free space wave number.

$$\boldsymbol{\kappa} = \begin{bmatrix} -2\Re(M_{vv}) & 0 & -\Re(M_{vh}) & -\Im(M_{vh}) \\ 0 & -2\Re(M_{hh}) & -\Re(M_{hv}) & \Im(M_{v}) \\ -2\Re(M_{hv}) & -2\Re(M_{vh}) & -\Re(M_{vv}+M_{hh}) & \Im(M_{vv}-M_{hh}) \\ 2\Im(M_{hv}) & -2\Im(M_{vh}) & -\Im(M_{vv}-M_{hh}) & -\Re(M_{vv}+M_{hh}) \end{bmatrix} \tag{2.10}$$

where

$$M_{pq} = \sum_{k=1}^{K} \frac{j2\pi N_k}{k_0}\langle S_{pqk}(\theta_s, \phi_s; \theta_i, \phi_i; \theta_k, \phi_k)\rangle_k; \qquad p, q = v, h \tag{2.11}$$

Under the incoherent assumption of RT theory, the extinction and emission processes within the medium can be represented mathematically by both the average extinction and source matrices of the medium. A 4×4 transformation matrix $\mathcal{T}$ is introduced to transform the incident intensity $\mathbf{I}_i$ to the scattered intensity $\mathbf{I}_s$ by the medium.

$$\mathbf{I}_s(\theta_s, \phi_s) = \mathcal{T}(\theta_s, \phi_s; \theta_i, \phi_i)\mathbf{I}_i(\theta_i, \phi_i) \tag{2.12}$$

The linearly polarized scattering coefficient can be obtained from $\mathcal{T}$ through

$$\begin{aligned} \sigma_{0vv} &= 4\pi \cos\theta_s \mathcal{T}_{11} \qquad \sigma_{0hv} = 4\pi \cos\theta_s \mathcal{T}_{12} \\ \sigma_{0hv} &= 4\pi \cos\theta_s \mathcal{T}_{21} \qquad \sigma_{0hh} = 4\pi \cos\theta_s \mathcal{T}_{22} \end{aligned} \tag{2.13}$$

and scattering coefficient of other polarization combinations can be computed from $\mathcal{T}$ using wave synthesis technique.

2.1.4 Introduction to MIMICS

Michigan Microwave Canopy Scattering (MIMICS) model [86] has been developed to model microwave backscattering from vegetation canopies. The model is based on the RT theory. The vertical canopy structure is modeled as two cascading independent horizontal vegetation layers over a dielectric ground surface. The top crown layer is composed of an ensemble of leaves, needles and branches while tree trunks make up the lower trunk layer. All the tree components are treated like single microwave scatterers: leaves are modeled as flat circular disks, branches and needles are modeled as dielectric cylinders or prolate spheroids, and trunks are again modeled as large cylinders. The underlying ground is modeled as a rough dielectric surface that is specified by an RMS height and a correlation length. Trees are assumed uniformly distributed over the ground and the scattering components within each layer are characterized by the statistics of their sizes, positions, orientations and densities.

Incident wave intensity undergoes the extinction and emission processes by the crown layer and trunk layer along its propagating path, which can be described by the RT equations for the layers. The incident intensity is also reflected and backscattered by the ground surface, which are denoted by reflectivity and scattering matrices. The diffuse boundary condition assumes that the wave intensities across the interfaces are continuous. MIMICS solves the RT equations to find the transformation matrix relating the incident intensity and the scattering intensity. Seven terms [86], which represent the seven scattering mechanisms (Figure 2.2) for wave energy propagating through the canopy down to the ground surface, reflected and backscattered from the ground surface, and propagating back through the canopy, are included in the first order MIMICS solution.

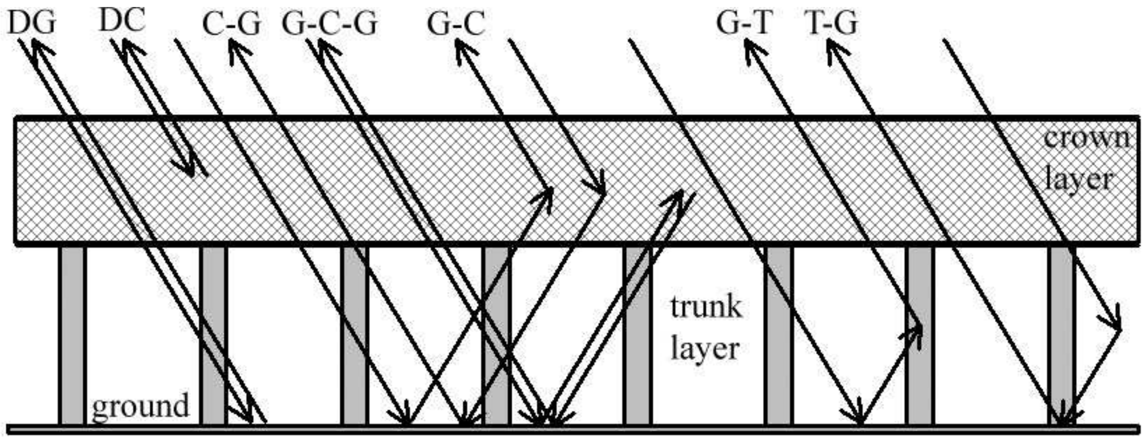

Figure 2.2: Seven backscattering terms in the first order MIMICS solution based on radiative transfer theory, including DG: direct ground; DC: direct crown backscattering; C-G: crown scattering and ground reflection; G-C: ground reflection and crown scattering; G-C-G: ground reflection and crown scattering and ground reflection; T-G: trunk scattering and ground reflection; G-T: ground reflection and trunk scattering.

There are four backscatter sources in the crown layer:

- DC: Direct backscattering from the crown layer. This mechanism indicates the incident intensity is attenuated and scattered back by the components in the crown layer without reaching the trunk layer.

- C-G: Crown specular scattering followed by ground reflection. The downward incident intensity is first scattered by the crown layer to the specular direction, then it penetrates the trunk layer and reaches the ground, finally, it is reflected by the ground and travels up through the two canopy layers to the air.

- G-C: Ground reflection followed by crown specular scattering. It is the complement of the C-G mechanisms. The incident intensity propagates through the canopy layers and attenuated by them before it hits and ground and gets reflected to the specular direction, the upward reflected intensity penetrates the trunk layer and scattered by the crown layer.

- G-C-G: Double bounce by ground reflection and crown backscattering and ground reflection. The incident intensity is first reflected by the ground surface, the upward wave reaches the crown layer and is backscattered by the crown layer and propagates in the downward direction, which is again is reflected by the round and travels through the canopy.

In the trunk layer, for the near-vertical oriented large cylindrical trunks, backscattering vanishes. Direct backscattering from the trunk layer and double bounce terms become insignificant, hence, only two mechanisms are included. They are

- T-G: Trunk specular scattering followed by ground reflection. This mechanisms is similar to the C-G mechanism, however, the scattering process occurs in the trunk layer instead of the crown layer, and the crown layer acts as a attenuating layer.

- G-T: Ground reflection followed by trunk specular scattering. As a complement of the T-G mechanisms, this mechanisms is similar to the G-C mechanism. The down incident intensity is first reflected into upward direction, then it is scattered by the trunk layer and continues traveling up to the top canopy surface.

One additional item included in the total scattering mechanisms is the backscattering from the ground surface DG. The incident intensity that propagates trough the canopy layers is attenuated but not scattered, and the ground surface scatters the downward intensity to the backscattering direction and the upward undergoes the similar attenuation process before it reaches the air.

The input parameters of MIMICS is a file that contains the microwave sensor information, the environment condition and grounds surface parameters, more importantly, it has a complete list of the structural characteristics of the canopies, which includes two levels: (1) Canopy level parameters such as tree height, crown depth, trunk height, canopy densities etc. (2) Tree level parameters such as geometric distributions of the the canopy components' type, size. density and orientation as well as their permittivities. MIMICS's outputs consists of the full polarimetric total transform matrix as well as the contributing components of the seven mechanisms, and it also computes the transmission loss of the each layer.

MIMICS is valid in the range of $0.5 \sim 10$ GHz at incidence angles greater than $10°$. The model has been validated and widely applied to estimate the microwave backscattering coefficients of various canopies in many studies. In a scatterometer experiment presented in [51,52], MIMICS simulated the L-band backscattering coefficient from a walnut orchard and was validated by measurements, although the simulation results showed some discrepancies with X-band. The problem was attributed to higher order scattering contributions and the discontinuity of the canopy. MIMICS has also been applied to the Alaskan Boreal Forest [16] to study the effects of thawing and freezing soil on the radar backscatter. Although it is developed for forest canopies, MIMICS has also been successfully applied to other types of vegetation such as corn fields [84].

2.2 Bistatic MIMICS Model Development

2.2.1 Bistatic Radiative Transfer Equation Solution

MIMICS built the general RT equation using bistatic geometry in order to derive the transformation matrix, which was explained in [86]. However, only the backscattering solution was implemented. More factors need to be considered for the bistatic scattering model. Consider the geometry of Figure 2.3, the downward incident intensity $\mathbf{I}_i$ impinges on the top surface of the canopy at an angle (θ_i, ϕ_i). The upward scattering intensity $\mathbf{I}_s$ is in the direction (θ_s, ϕ_s).

The incidence azimuth angle ϕ_i is set to be zero to reduce the number of variables of Bi-MIMICS model. Three angle parameters defining the incidence and scattering angle are shown in Figure 2.3. $\vec{k_i}$ is the wave vector of the downward incident wave and defined by $(\theta_i, 0)$ while $\vec{k_s}$ is the wave vector of the upward scattering wave and defined by (θ_s, ϕ_s). Under this definition, the set $\{\theta_s = \theta_i,\ \phi_s = 180°\}$ indicates backscattering, $\{\theta_s = \theta_i,\ \phi_s = 0\}$ stands for specular scattering and $\{\theta_s = \pi - \theta_i,\ \phi_s = 0\}$ denotes forward scattering.

The canopy is modeled as two parallel layers over a ground surface as in MIMICS. On top of the ground surface, is a trunk layer, above which is the the crown layer containing branches and foliage. The bistatic radiative transfer equations are written for each layer. Under the assumption of diffuse interfaces among layers, the equations

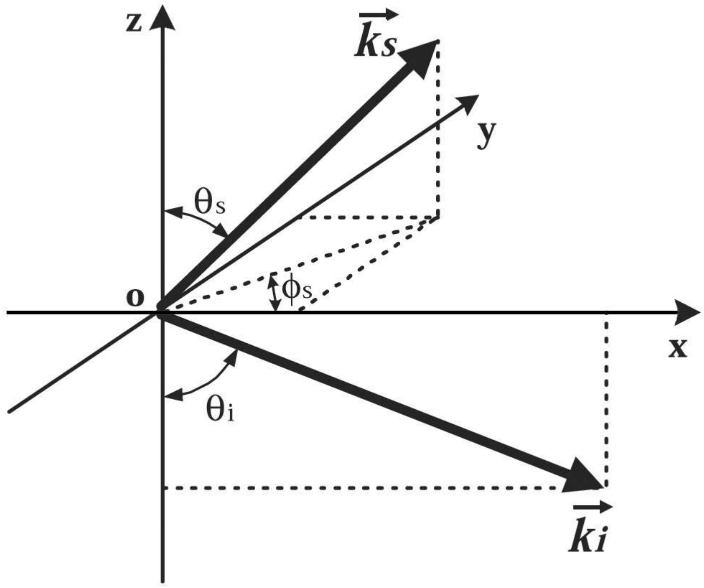

Figure 2.3: Bistatic Simulation Angles. Incident direction (downward) is in the x-z plane and defined by incidence angle θ_i and $\phi_i = 0$; Scattering direction (upward) is defined by θ_s and ϕ_s.

are solved using iterative approach.

In Bi-MIMICS, the first order bistatic transformation matrix $\mathcal{T}$ transforms the incident intensity into the scattering intensity by

$$\mathbf{I}_s(\mu_s, \phi_s) = \mathcal{T}(\mu_s, \phi_s; \mu_i, \phi_i)\mathbf{I}_i(\mu_i, \phi_i) \tag{2.14}$$

where $(\mu_i = \cos\theta_i, \phi_i)$ defines the incidence direction and $(\mu = \cos\theta, \phi)$ is the scattered direction. The seven scattering mechanisms described in backscattering MIMICS still exist but they are measured in bistatic directions as shown in Figure 2.4. In addition, the ground reflection in the specular direction needs to be included in the case of specular scattering. Figure 2.4 also shows the canopy structure above the ground. The depths of the crown and trunk layer are denoted by d and H, respectively. The transformation matrix $\mathcal{T}$ (shown in Equation 2.15) is given by solving the bistatic RT equations using similar approach as in MIMICS [50], so detailed steps

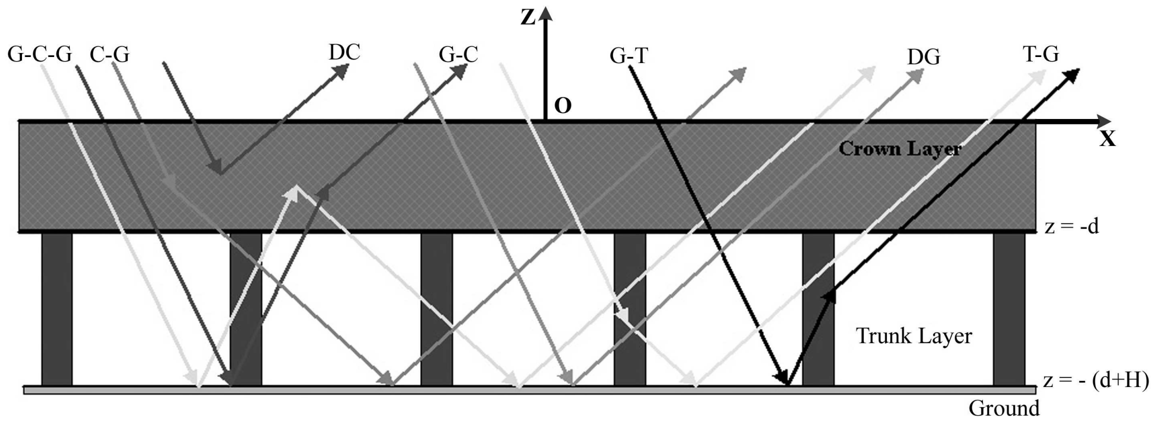

Figure 2.4: Scattering mechanisms in the first order Bi-MIMICS solution based on RT theory, including G-C-G: ground reflection and crown scattering and ground reflection; C-G: crown scattering and ground reflection; DC: direct crown backscattering; G-C: ground reflection and crown scattering; G-T: ground reflection and trunk scattering. DG: direct ground; T-G: trunk scattering and ground reflection; The specular ground reflection is not shown in the figure. Crown layer depth = d, Trunk layer height = H.

are not given here.

$$
\begin{aligned}
\mathcal{T}(\mu_s, \phi_s; \mu_i, \phi_i) &= e^{-\boldsymbol{\kappa}_c^+ d/\mu} e^{-\boldsymbol{\kappa}_t^+ H/\mu} \mathcal{R}(\mu_s) e^{-\boldsymbol{\kappa}_t^- H/\mu} e^{-\boldsymbol{\kappa}_c^- d/\mu} \delta(\mu - \mu_i)\delta(\phi - \phi_i) \\
&+ \frac{1}{\mu} e^{-\boldsymbol{\kappa}_c^+ d/\mu} e^{-\boldsymbol{\kappa}_t^+ H/\mu} \mathcal{R}(\mu_s) e^{-\boldsymbol{\kappa}_t^- H/\mu} \mathcal{A}_{gcg}(-\mu_s, \phi_s; \mu_i, \phi_i) \\
&\quad e^{-\boldsymbol{\kappa}_t^+ H/\mu_i} \mathcal{R}(\mu_i) e^{-\boldsymbol{\kappa}_t^- H/\mu_i} e^{-\boldsymbol{\kappa}_c^- d/\mu_i} \\
&+ \frac{1}{\mu} e^{-\boldsymbol{\kappa}_c^+ d/\mu} e^{-\boldsymbol{\kappa}_t^+ H/\mu} \mathcal{R}(\mu_s) e^{-\boldsymbol{\kappa}_t^- H/\mu} \mathcal{A}_{cg}(-\mu_s, \phi_s; -\mu_i, \phi_i) \\
&+ \frac{1}{\mu} \mathcal{A}_{gc}(\mu_s, \phi_s; \mu_i, \phi_i) e^{-\boldsymbol{\kappa}_t^+ H/\mu_i} \mathcal{R}(\mu_i) e^{-\boldsymbol{\kappa}_t^- H/\mu_i} e^{-\boldsymbol{\kappa}_c^- d/\mu_i} \\
&+ \frac{1}{\mu} \mathcal{A}_{dc}(\mu_s, \phi_s; -\mu_i, \phi_i) \\
&+ \frac{1}{\mu} e^{-\boldsymbol{\kappa}_c^+ d/\mu} e^{-\boldsymbol{\kappa}_t^+ H/\mu} \mathcal{R}(\mu_s) \mathcal{A}_{tg}(-\mu_s, \phi_s; -\mu_i, \phi_i) e^{-\boldsymbol{\kappa}_c^- d/\mu_i} \delta(\mu - \mu_i) \\
&+ \frac{1}{\mu} e^{-\boldsymbol{\kappa}_c^+ d/\mu} \mathcal{A}_{gt}(\mu_s, \phi_s; \mu_i, \phi_i) \mathcal{R}(\mu_i) e^{-\boldsymbol{\kappa}_t^- H/\mu_i} e^{-\boldsymbol{\kappa}_c^- d/\mu_i} \delta(\mu - \mu_i) \\
&+ e^{-\boldsymbol{\kappa}_c^+ d/\mu} e^{-\boldsymbol{\kappa}_t^+ H/\mu} \mathcal{G}(\mu_s, \phi_s; -\mu_i, \phi_i) e^{-\boldsymbol{\kappa}_t^- H/\mu} e^{-\boldsymbol{\kappa}_c^- d/\mu} \qquad (2.15)
\end{aligned}
$$

where the upward extinction matrix and the downward extinction matrix are denoted by $\boldsymbol{\kappa}^+$ and $\boldsymbol{\kappa}^-$, respectively. The subscripts c and l indicate the crown and trunk layer, respectively. The quantity $\mathcal{R}$ is the reflectivity matrix of the specular ground surface and $\mathcal{G}$ represents the ground scattering matrix. The $\mathcal{A}$ notations represent the scattering occurring in the crown and trunk layer, which could be obtained by proper phase matrices and extinction matrices [50].

The first term in $\mathcal{T}$ denotes the specular ground reflection, which exists only in the specular direction (i.e. $\theta_s = \theta_i$, $\phi_s = \phi_i$). Proper attenuation is applied to the intensity as it penetrates twice through the canopy. The next four terms are contributions from the crown layer corresponding to the mechanisms of G-C-G, C-G, G-C and DC, although we use the same notions as in MIMICS to describe the crown layer's contribution, they represent the general case of bistatic scattering system. Two types of ground-trunk interaction T-G and G-T are represented by the sixth and seventh term and the last term is the direct bistatic scattering from the rough ground surface DG.

The term $\mathcal{A}_{gcg}$ indicates the scattering contribution to the Ground — Scatterer — Ground mechanism. The term $\mathcal{A}_{cg}$ accounts for the Scatterer — Ground effect by the crown layer; The term $\mathcal{A}_{gc}$ is the complement of $\mathcal{A}_{cg}$ and shows that the incident intensity is first reflected by the ground and then scattered into the direction (μ_s, ϕ_s) by the crown layer. The term $\mathcal{A}_{dc}$ shows the direct bistatic scattering by the crown layer. The terms $\mathcal{A}_{tg}$ and $\mathcal{A}_{gt}$ represent the scattering by the trunk layer and ground interactions, similar to $\mathcal{A}_{cg}$ and $\mathcal{A}_{gc}$.

The term $\mathcal{A}_{gcg}$ integrates the wave intensity that is scattered from the upward direction $(\mu_i, 0)$ to the downward direction $(-\mu_s, \phi_s)$ through the crown layer, which is also attenuated along the propagation path. Similar approaches are applied to get the other $\mathcal{A}$ integrals as shown in Equation (2.16), where $\mathcal{P}_c$ and $\mathcal{P}_t$ are the average phase matrices for the crown and trunk layer, respectively, in which the angle argument of $(\mu_s, \phi_s, \mu_i, \phi_i)$ indicates that the wave intensity is scattered from the (μ_i, ϕ_i) direction to the (μ_s, ϕ_s) direction.

$$
\begin{aligned}
\mathcal{A}_{cgc}(-\mu_s, \phi_s; \mu_i, \phi_i) &= \int_{-d}^{0} e^{-\boldsymbol{\kappa}_c^-(d+z')/\mu} \mathcal{P}_c(-\mu_s, \phi_s; \mu_i, \phi_i) e^{-\boldsymbol{\kappa}_c^+(z'+d)/\mu_i} \mathrm{d}z' \\
\mathcal{A}_{cg}(-\mu_s, \phi_s; -\mu_i, \phi_i) &= \int_{-d}^{0} e^{-\boldsymbol{\kappa}_c^-(d+z')/\mu} \mathcal{P}_c(-\mu_s, \phi_s; -\mu_i, \phi_i) e^{\boldsymbol{\kappa}_c^- z'/\mu_i} \mathrm{d}z' \\
\mathcal{A}_{gc}(\mu_s, \phi_s; \mu_i, \phi_i) &= \int_{-d}^{0} e^{\boldsymbol{\kappa}_c^+ z'/\mu} \mathcal{P}_c(\mu_s, \phi_s; \mu_i, \phi_i) e^{-\boldsymbol{\kappa}_c^+(z'+d)/\mu_i} \mathrm{d}z' \\
\mathcal{A}_{dc}(\mu_s, \phi_s; -\mu_i, \phi_i) &= \int_{-d}^{0} e^{\boldsymbol{\kappa}_c^+ z'/\mu} \mathcal{P}_c(\mu_s, \phi_s; -\mu_i, \phi_i) e^{\boldsymbol{\kappa}_c^- z'/\mu_i} \mathrm{d}z' \qquad (2.16) \\
\mathcal{A}_{tg}(-\mu_s, \phi_s; -\mu_i, \phi_i) &= \int_{-(d+H)}^{-d} e^{-\boldsymbol{\kappa}_t^-(H+z')/\mu} \mathcal{P}_t(-\mu_s, \phi_s; -\mu_i, \phi_i) e^{\boldsymbol{\kappa}_t^-(z'+d)/\mu_i} \mathrm{d}z' \\
\mathcal{A}_{gt}(\mu_s, \phi_s; \mu_i, \phi_i) &= \int_{-(d+H)}^{-d} e^{\boldsymbol{\kappa}_t^+(d+z')/\mu} \mathcal{P}_t(\mu_s, \phi_s; \mu_i, \phi_i) e^{-\boldsymbol{\kappa}_t^+(z'+d+H)/\mu_i} \mathrm{d}z'
\end{aligned}
$$

The reflectivity matrix of the specular ground surface at angle $\mu = \cos\theta$ is given by

$$
\mathcal{R}(\mu) = \begin{bmatrix} |r_v|^2 & 0 & 0 & 0 \\ 0 & |r_h|^2 & 0 & 0 \\ 0 & 0 & \Re(r_v r_h^*) & -\Im(r_v r_h^*) \\ 0 & 0 & \Im(r_v r_h^*) & \Re(r_v r_h^*) \end{bmatrix} \qquad (2.17)
$$

where r_v and r_h

$$
\begin{aligned}
r_v &= \frac{\epsilon_r \cos\theta - \sqrt{\epsilon_r - \sin\theta^2}}{\epsilon_r \cos\theta + \sqrt{\epsilon_r - \sin\theta^2}} \\
r_h &= \frac{\cos\theta - \sqrt{\epsilon_r - \sin\theta^2}}{\cos\theta + \sqrt{\epsilon_r - \sin\theta^2}} \qquad (2.18)
\end{aligned}
$$

are the specular reflection coefficients at vertical and horizontal polarizations, respectively. ϵ_r is the relative dielectric constant of the ground. The ground scattering matrix $\mathcal{G}$ is calculated from rough surface scattering models.

In this section, the mathematic solution of Bi-MIMICS RT equations are derived, and the terms in the solution are analyzed for the physical bistatic scattering mechanisms. The implementation of the solution is then described in the next section.

2.2.2 Bi-MIMICS Model Implementation

2.2.2.1 Scattering Models For Canopy Compositions

For every type of canopy component, several analytical and empirical models are provided for different regions of validity with respect to their shapes and sizes [50] and they are adopted in Bi-MIMICS.

- Trunks are modeled as homogeneous dielectric cylinders with mean length l and mean diameter d. An appropriate approximation is derived from the infinitely long large cylinder scattering model.

- Branch are also modeled as dielectric cylinders with mean length l and mean diameter d. Prolate Rayleigh spheroids are used to model small cylinders ($l << \lambda$) such as small branches. For many types of intermediate size branches, a long ($l >> \lambda$) and thin ($d << \lambda$) cylinder model is used. As for large branches, an approximation of a infinitely cylinder scattering model is used.

- Leaves are modeled as dielectric circular disks with a thickness and diameter. Two scattering models are used for leaves — an oblate Rayleigh spheroid or a physical optics model, depending on the disk diameter d. If the disk diameter is small compared to the wavelength ($d << \lambda$), the Rayleigh spheroid model is appropriate. otherwise, the physical optics model is suitable.

- Needle are modeled as small cylinders, for which a prolate Rayleigh spheroid model is used.

All the scattering models are parametrized by the canopy components' shape, size and orientation as well as the incidence and scattering angles and dielectric constants. They provide the electrical field scattering matrices which are the bases for computing individual extinction and phase metrics for all types of canopy scatterers.

2.2.2.2 Scattering Models For Ground Surface

The ground underneath the canopy layer is modeled as a rough dielectric surface that is characterized by the RMS height and correlation length. Three rough surface models, Geometrical Optics (GO), Physical Optics (PO), and Small Perturbation (SP) model are provided to simulate different roughness scales of the ground. Surface roughness and the observation angle and microwave frequency together affect the scattering behavior of the ground. The GO model is usually appropriate for very rough surface and the SP model is preferred when the surface's correlating length is small, while the PO model falls in the middle and is ideal for the intermediate scale of roughness. The polarized electric field scattering matrix of the ground surface can be computed by these models and as a result, the modified Mueller matrix of the ground is obtained through Equation (2.6).

The bistatic scattering simulation of three rough surface scattering models has been validated at X-band. The bistatic radar RCS measurements taken for surfaces with artificial roughness using a 10 GHz bistatic system [14] are consistent with rough surface models' simulations.

2.2.2.3 Permittivity Model

The dielectric constants of various canopy constituents are determined from their moisture contents through analytical and empirical models. For canopy components with known gravimetric moisture content and the dry material density, given the environment temperature and the microwave frequency, their permittivities can be calculated from the established relationships. So for the ground surface, since soil usually contains major constitutes such as clay, sand and silt, the composition of day soil and the volumetric moisture constant as well as the environment parameters build the empirical model for the soil dielectric constant. The permittivities for various canopy parts and soil can also be acquired during field measurements.

2.2.2.4 Model Parameters and Processes

Two angle parameters θ_s and ϕ_s are added as compared with backscattering MIMICS. In the calculation of the upward and downward extinction matrices for the crown and trunk layers, both directions are needed instead of one direction as in backscattering MIMICS. Therefore, four types of angle combinations are chosen to calculate the attenuating extinction matrices: two upward directions $(\theta_i, 0)$ and (θ_s, ϕ_s), and two downward directions $(\pi - \theta_i, 0)$ and $(\pi - \theta_s, \phi_s)$. Similarly, this is also done for the phase matrices. Four angle transformations are necessary to calculate the phase matrices: from $(\theta_i, 0)$ to (θ_s, ϕ_s), from (θ_i, i) to $(\pi - \theta_s, \phi_s)$, from $(\pi - \theta_i, 0)$ to (θ_s, ϕ_s) and from $(\pi - \theta_i, 0)$ to $(\pi - \theta_s, \phi_s)$. When we calculate the $\mathcal{A}$ integrals, unlike the backscattering case, the extinction matrices $\boldsymbol{\kappa}$ before scattering are not in the parallel direction to those after scattering, therefore the azimuthal symmetry of canopy (i.e., $\boldsymbol{\kappa}(\mu_0, 0) = \boldsymbol{\kappa}(\mu_0, \pi)$) is only valid for the special backscattering case, and for the general cases both the angles of θ_i and θ need to be calculated.

The downward microwave intensities are reflected by the ground surface at two angles related to the location from which the scattering happens: If the wave is first scattered by the crown or trunk layer from $(-\mu_i, 0)$ direction to $(-\mu_s, \phi_s)$ direction before it penetrates the canopy, the ground reflection angle is then θ_s and the ground reflectivity matrix is $\mathcal{R}(\mu_s)$. However, if the penetrating wave is first reflected by the ground and then scattered by the vegetation layers, the ground reflection angle is then θ_i and the ground reflectivity matrix is $\mathcal{R}(\mu_i)$. For the crown double bounce scattering mechanism, θ_i is the first ground reflection angle and θ_s is for the second ground reflection. Therefore, two ground reflectivity matrices $\mathcal{R}(\mu_i)$ and $\mathcal{R}(\mu_s)$ are needed as compared to MIMICS, which only calculates $\mathcal{R}(\mu_i)$.

In conclusion, Bi-MIMICS calculates the average bistatic extinction matrices and phase matrices of the combination of scatterers in the crown and trunk layer, reflectivity matrices and scattering matrices of the ground at certain angles, and then places them together through proper attenuation and scattering to get the total canopy transformation matrix.

2.3 Model Simulation Parameter Configuration

2.3.1 Sensor Parameters

We simulate the fully-polarized microwave scattering (HH, HV, VH, VV) for the canopies at L-, C- and X-bands using Bi-MIMICS. The frequencies are 1.62GHz, 4.75GHz and 10GHz, respectively. These frequencies are chosen for studying the scattering from different part of the canopy, since L-band has the strongest penetration while X band is most scattered by the top part of the canopy, and C-band has the moderate penetration and attenuation compared to other two frequencies.

Various bistatic observation angle combinations are simulated. Backscattering plane, specular scattering plane, and specular direction cone surface are paid special attention because the trunk scattering is the strongest on these surfaces. When the observation direction is outside of these surfaces, the trunk layer functions only as an attenuating layer since the trunk scattering is very weak. The specular direction cone surface is shown in Figure 2.5. The elevation angles θ_i and θ_s change from 10° to 70° while the azimuth angle ϕ_s rotates from 0° to 180° to cover the backscattering and specular scattering direction.

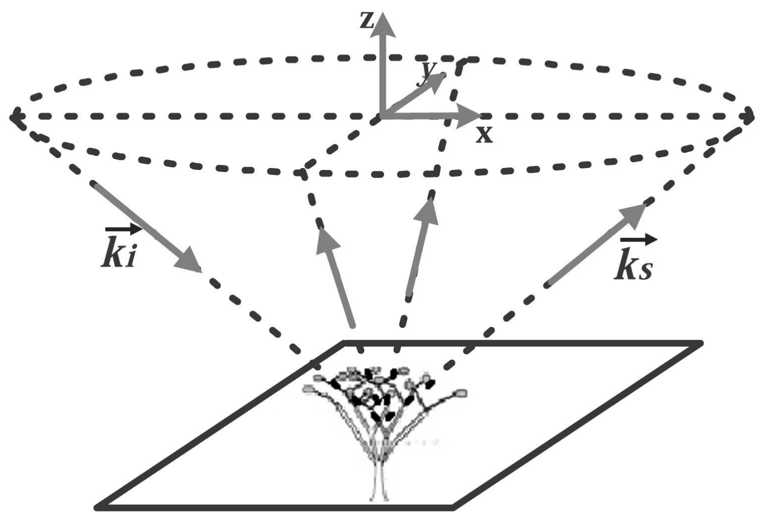

Figure 2.5: Specular Direction Cone Surface. Incidence angle θ_i = scattering angle θ_s, $0 \geq \phi_s \geq 360°$ forms a cone surface.

2.3.2 Canopy Parameters

Two types of canopies are chosen for the bistatic scattering simulation. One is a deciduous tree stand of defoliated aspen. The other is a conifer tree stand of white spruce. The relevant canopy parameters are listed in Table 2.1. The canopy data are collected from [86]. A Physical Optics (PO) model is used for the ground surface.

The orientations of the canopy branches are assumed to be uniformly distributed in the horizontal direction. For the aspen stand, the branch angle probability density

Table 2.1: Canopy Parameters for Simulations

Parameters	Aspen	White Spruce
Canopy Density	$0.11m^{-2}$	$0.2m^{-2}$
Trunk Height	8m	16m
Trunk Diameter	24cm	20.8cm
Trunk Moisture	0.5	0.6
Crown Depth	2m	11m
Leaf Density (gravimetric)	0	$85000m^{-}3$
Leaf Moisture	-	0.8
LAI (single sided)	0	11.9
Branch Density (gravimetric)	$4.1m^{-3}$	$3.4m^{-3}$
Branch Length	0.75m	2.0m
Branch Diameter	0.7cm	2.0 cm
Branch Moisture	0.4	0.6
Soil RMS Height	0.45cm	0.45cm
Correlation Length	18.75cm	18.75cm
Soil Moisture (volumetric)	0.15	0.15
Soil % Sand	10	20
Soil % Silt	30	70
Soil % Clay	60	10

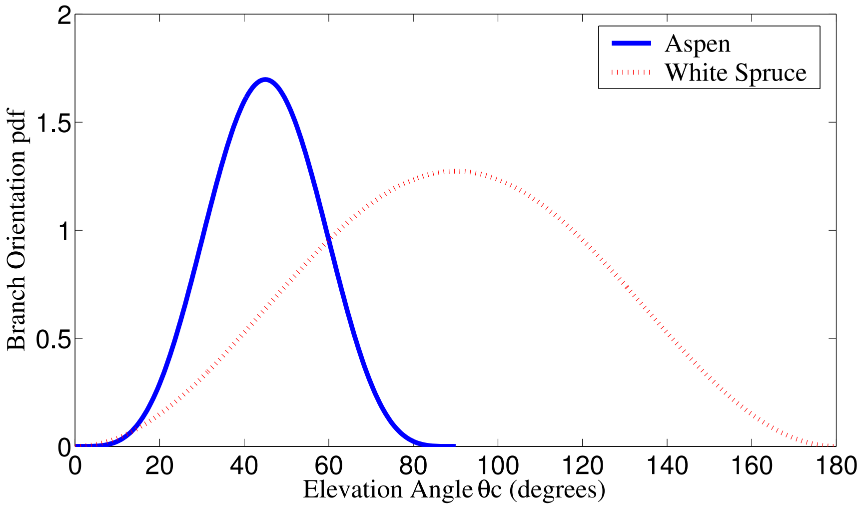

Figure 2.6: Branch orientation pdf in the vertical direction of the aspen stand and white spruce stand.

function (pdf) in the vertical direction is chosen as

$$p(\theta_c) = \frac{\sin^4(2\theta_c)}{\int_0^{\frac{\pi}{2}} \sin^4(2\theta_c)\mathrm{d}\theta_c} = \frac{16}{3\pi}\sin^4(2\theta_c), \qquad 0 \leq \theta_c \leq \frac{\pi}{2} \tag{2.19}$$

which results in a center at $\theta_c = \frac{\pi}{4}$.

For the white spruce stand, the branch orientation pdf in the vertical direction is chosen as

$$p(\theta_c) = \frac{\sin^2(\theta_c)}{\int_0^{\pi} \sin^2(\theta_c)\mathrm{d}\theta_c} = \frac{2}{\pi}\sin^2(\theta_c), \qquad 0 \leq \theta_c \leq \pi \tag{2.20}$$

which is centered at $\theta_c = \frac{\pi}{2}$. Figure 2.6 shows the pdfs of the branch orientation of the two stands.

Trunk of both stands are vertical and orientation of needles of the white spruce stand is assumed uniform in both the elevation and azimuth directions.

At an environment temperature of 20°C, the permittivities for the ground and components are calculated and listed in Table 2.2.

Table 2.2: Permittivities of Canopies

Stand	Soil	Trunk	Branch	Foliage
Aspen	5.99 -j 0.99	14.49 -j 4.76	10.19 -j 3.36	-
White Spruce	6.27 -j 1.55	16.45 -j 7.31	16.45 -j 7.31	27.00 -j12.43

2.4 Simulation Results and Analysis

2.4.1 Comparison with Backscattering MIMICS

For each canopy and incidence angle, we compare the backscattering σ^0 simulated by Bi-MIMICS and standard MIMICS. Two models provide the same results. Although we don't have measured bistatic data and hence can't validate the Bi-MIMICS simulated bistatic σ^0 with existing radar measurement, backscattering MIMICS has been verified on actual forest inventory data and SAR data by over the years [16, 51, 52]. The consistence between two models indicates that Bi-MIMICS is an effective canopy scattering model for the special backscattering case.

2.4.2 Bistatic Scattering Simulation for A Aspen Stand

Based on the model input parameters, simulation of the SAR scattering at all frequencies and polarizations is undertaken using Bi-MIMICS for multiple observation angles.

The VV-polarized total scattering from the aspen stand is shown in Figure 2.7. Subfigures 2.7(a) and 2.7(c) are for the backscattering and specular cases respectively, when the elevation angle θ_s is in the range of $10°$ to $70°$. In Figure 2.7(b), the angles $\theta_i = 30°$, $\phi_s = 120°$ are fixed while θ_s changes from $10°$ to $70°$. Figure 2.7(d) plots the observation made in the plane perpendicular to ($\theta_s = \theta_i$, $\phi_s = 90°$) the incident direction. The figures show that the overall scattering in the specular direction is the strongest, as expected. Figure 2.7(b) indicates that this aspen stand is a trunk-dominated canopy since we observe a scattering peak at $\theta_s = \theta_i = 30°$, which includes the trunk's contribution. At other angles of θ_s, the much lower level of the scattering coefficient is from the crown layer and ground. Figure 2.7(a), 2.7(c) and 2.7(d) also indicate the more canopy VV-polarized scattering occurs at higher frequencies because of much stronger scattering from the trunk-ground interaction and crown-ground interaction. However, the strongest direct crown scattering and double bounce scattering between the crown and ground occur at C-band due to lower volume scattering at L-band and more crown attenuation at X-band, which is shown by Figure 2.7(b), the figure shows that C-band has the highest bistatic scattering coefficient σ^0 when the trunk scattering is not present.

As for the cross polarization, VH-polarized σ^0 demonstrates a different canopy response at the observation angles as shown in Figure 2.8. The component contributions to the total scattering at L-band are shown in Figure 2.9. The C-band VH-polarized backscattering RCS exceeds the X-band result (Figure 2.8(a)) in contrast to the other three configurations, in which the X-band gives the strongest scattering coefficient. Figure 2.8 and 2.9 also demonstrate that crown-ground interactions are the major part of VH-backscattering RCS, and C-band has the largest value for moderate scattering and moderate attenuation compared to the other two bands. The trunk-ground interactions provide little VH polarization scattering contribution in the backscattering and specular direction as in Figure 2.9(a) and 2.9(c), the trunk and ground scattering are two low to be shown in the figures. In contrast, the trunk-ground interactions dominate the total scattering as in Figure 2.9(d).

Figures 2.10 and 2.11 present the HH-polarized component scattering contributions from the trunk, crown, and ground layer at L- and X-bands, respectively. Both

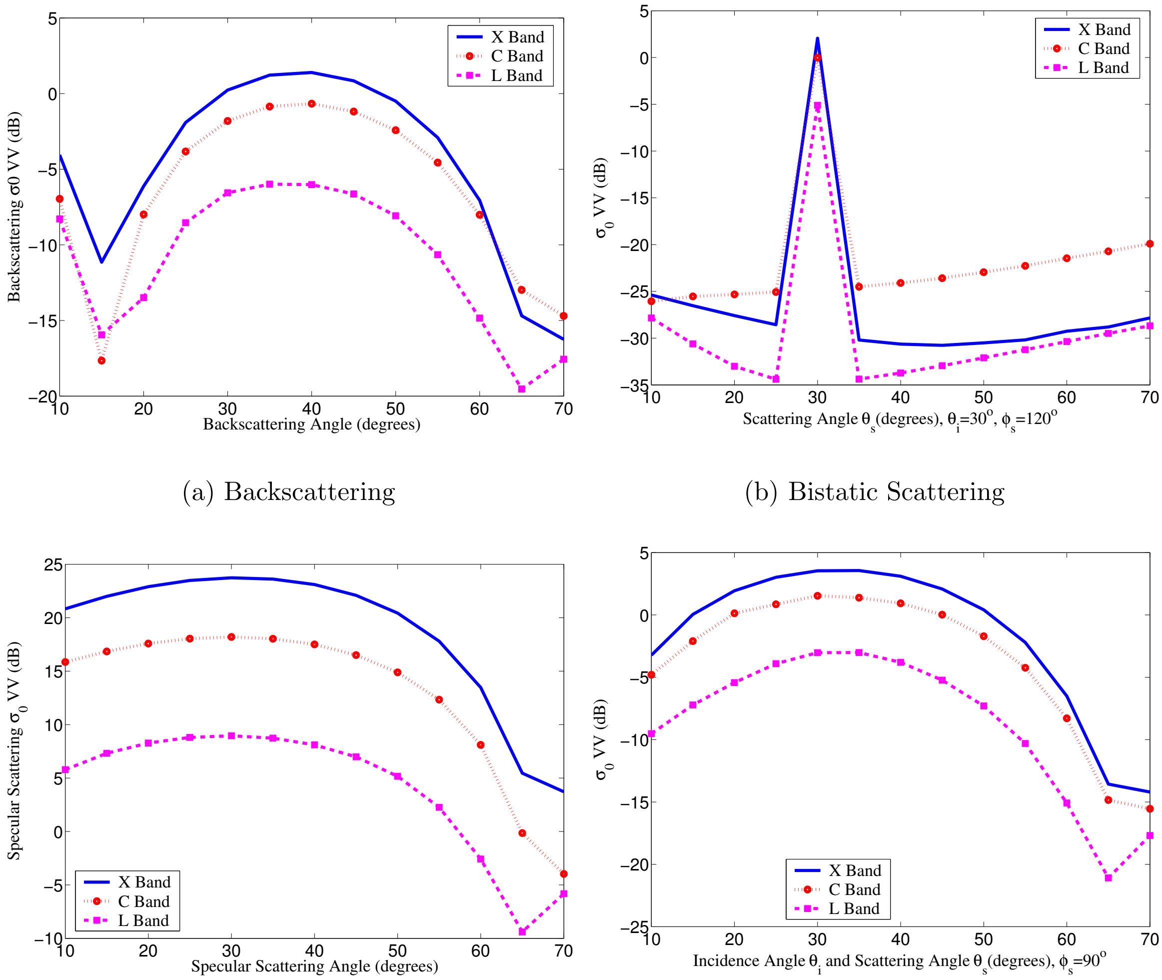

(a) Backscattering

(b) Bistatic Scattering

(c) Specular Scattering

(d) Perpendicular Plane

Figure 2.7: VV-polarized canopy scattering cross section vs. scattering angle from aspen for L-, C- and X-bands at (a) Backscattering plane. (b) $\theta_i = 30°$ and $\phi_s = 120°$. (c) Specular plane. (d) Perpendicular plane ($\theta_s = \theta_i$, $\phi_s = 90°$).

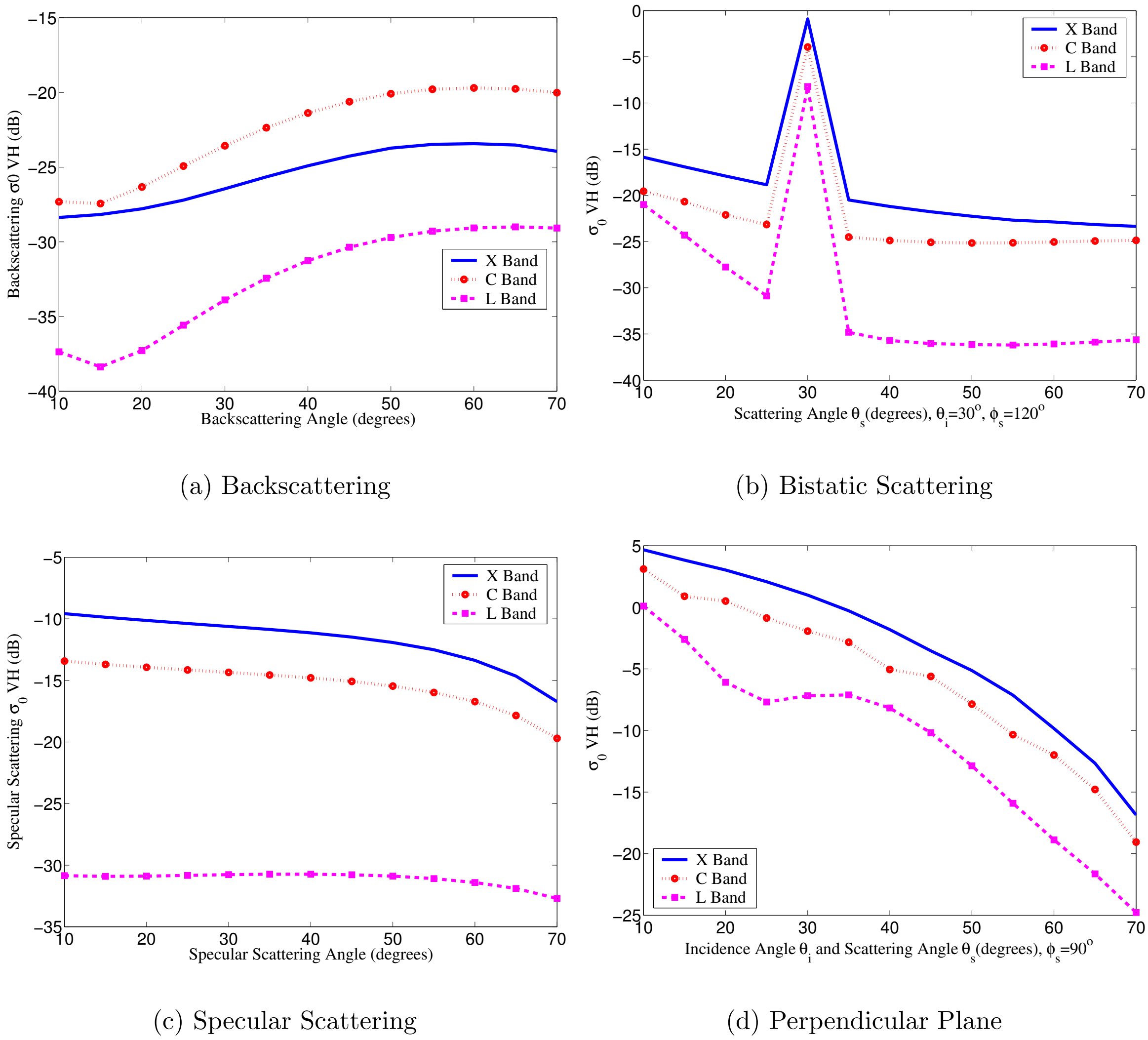

(a) Backscattering

(b) Bistatic Scattering

(c) Specular Scattering

(d) Perpendicular Plane

Figure 2.8: VH-polarized canopy scattering cross section vs. scattering angle from aspen for L-, C- and X-bands at (a) Backscattering plane. (b) $\theta_i = 30°$ and $\phi_s = 120°$. (c) Specular plane. (d) Perpendicular plane ($\theta_s = \theta_i$, $\phi_s = 90°$).

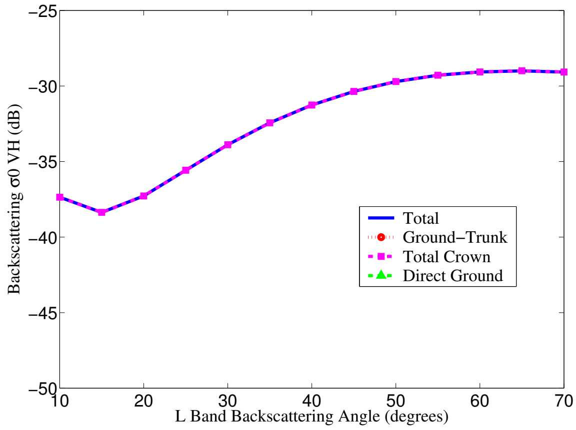

(a) Backscattering

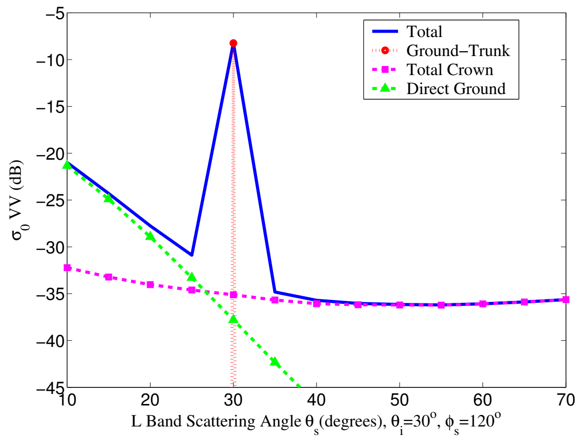

(b) Bistatic Scattering

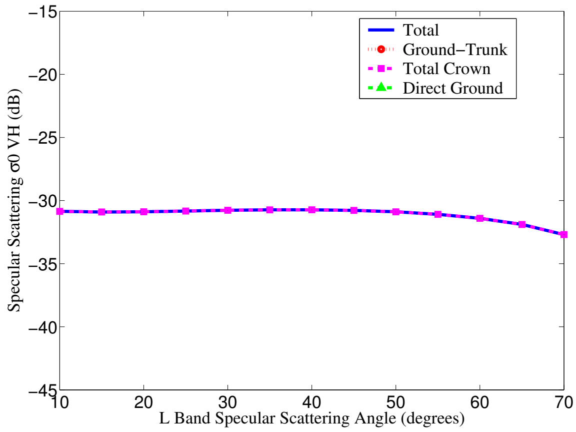

(c) Specular Scattering

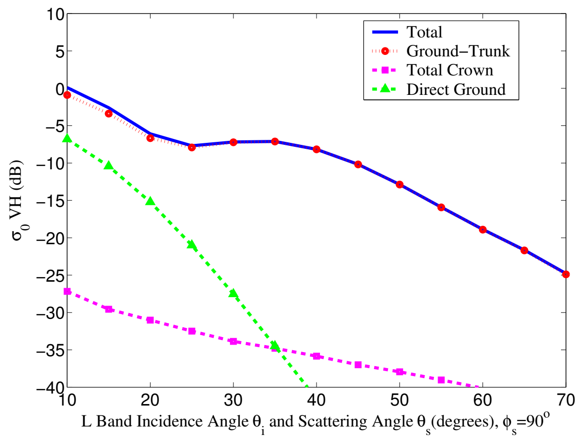

(d) Perpendicular Plane

Figure 2.9: L-band VH-polarized canopy scattering component contributions vs. scattering angle from aspen at (a) Backscattering plane. (b) $\theta_i = 30°$ and $\phi_s = 120°$. (c) Specular plane. (d) Perpendicular plane ($\theta_s = \theta_i$, $\phi_s = 90°$).

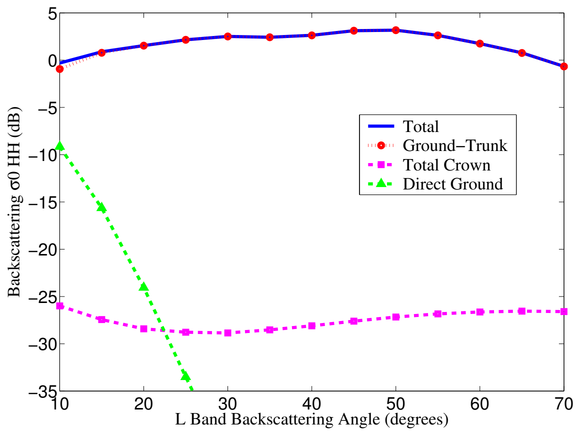

(a) Backscattering

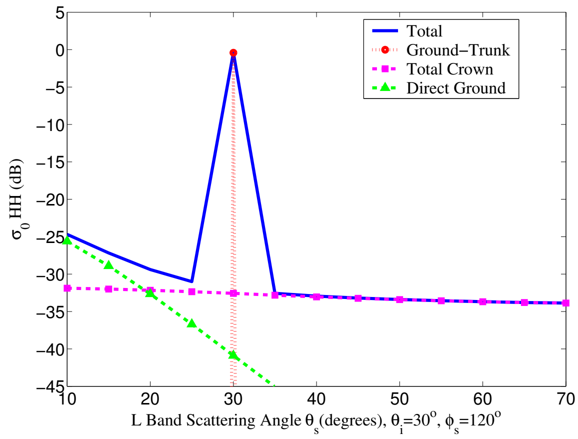

(b) Bistatic Scattering

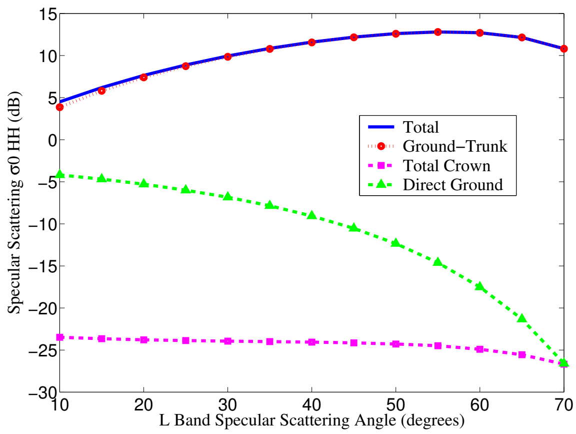

(c) Specular Scattering

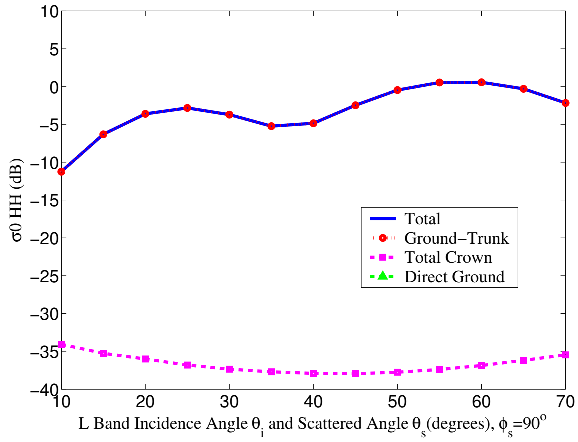

(d) Perpendicular Plane

Figure 2.10: L-band HH-polarized canopy scattering component contributions vs. scattering angle from aspen at (a) Backscattering plane. (b) $\theta_i = 30°$ and $\phi_s = 120°$. (c) Specular plane. (d) Perpendicular plane ($\theta_s = \theta_i$, $\phi_s = 90°$).

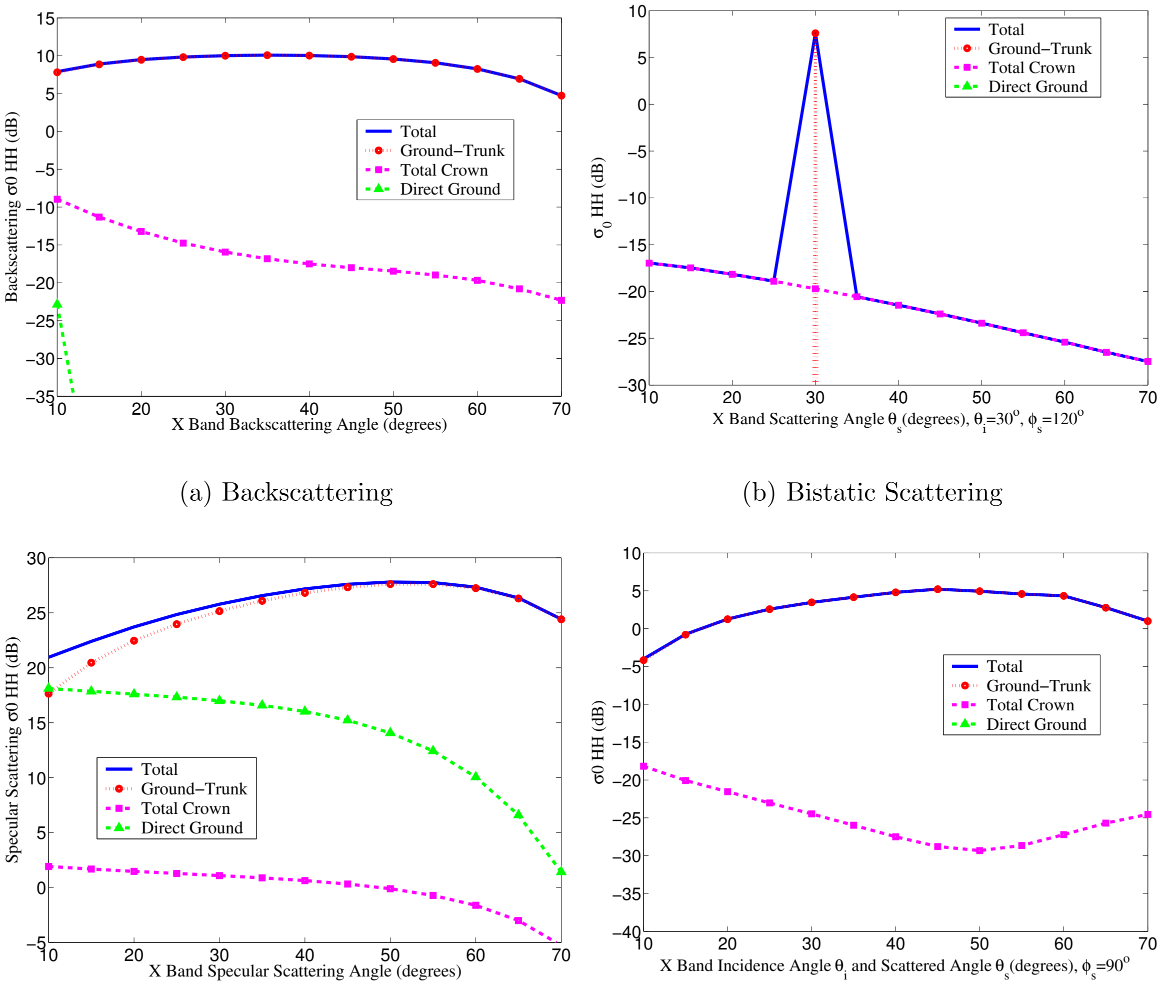

(a) Backscattering

(b) Bistatic Scattering

(c) Specular Scattering

(d) Perpendicular Plane

Figure 2.11: X-band HH-polarized canopy scattering component contribution vs. scattering angle from aspen at (a) Backscattering plane. (b) $\theta_i = 30°$ and $\phi_s = 120°$. (c) Specular plane. (d) Perpendicular plane ($\theta_s = \theta_i$, $\phi_s = 90°$).

Table 2.3: Trunk and Branch Diameter for Four Aspen Stands

	Stand 1	Stand 2	Stand 3	Stand 4
Trunk Diameter	24cm	30cm	24cm	30cm
Branch Diameter	0.7cm	0.7cm	0.9cm	0.9cm

figures show that the aspen stand is trunk dominated since the ground-trunk scattering mechanism contributes most to the total scattering. Direct ground scattering decreases when the scattering angle θ_s increases. As for multiple frequencies, in the backscattering cases, the ground scattering decreases when the frequencies increase, but in the specular scattering cases, the figures show the opposite trend. Moreover, at L-band, scattering at small angles $\theta_s < 20°$, the ground scattering contribution is greater than the crown layer scattering in Figure 2.10(a) and 2.10(b) while ground scattering is much lower than the crown scattering at X-band in Figures 2.11(a) and 2.11(b). The crown layer scattering is much stronger at X-band than at L-band.

2.4.3 Scattering Angle Sensitivity to Canopy Parameters

The bistatic scattering's sensitivity to the canopy parameter changes is of great interest in optimizing radar system designs. In this section, we change various canopy parameters and analyze the results for L-band.

2.4.3.1 Aspen stands

In this experiment, we simulate the microwave scattering in a specular direction cone surface ($\theta_s = \theta_i = 45°$, $0 \leq \phi_s \leq 180°$) for four aspen stands with different trunk and branch diameters, which means the biomass of these four stands are different. While the other parameters are the same as in Table 2.1, Table 2.3 lists the aspen's trunk and branch diameters.

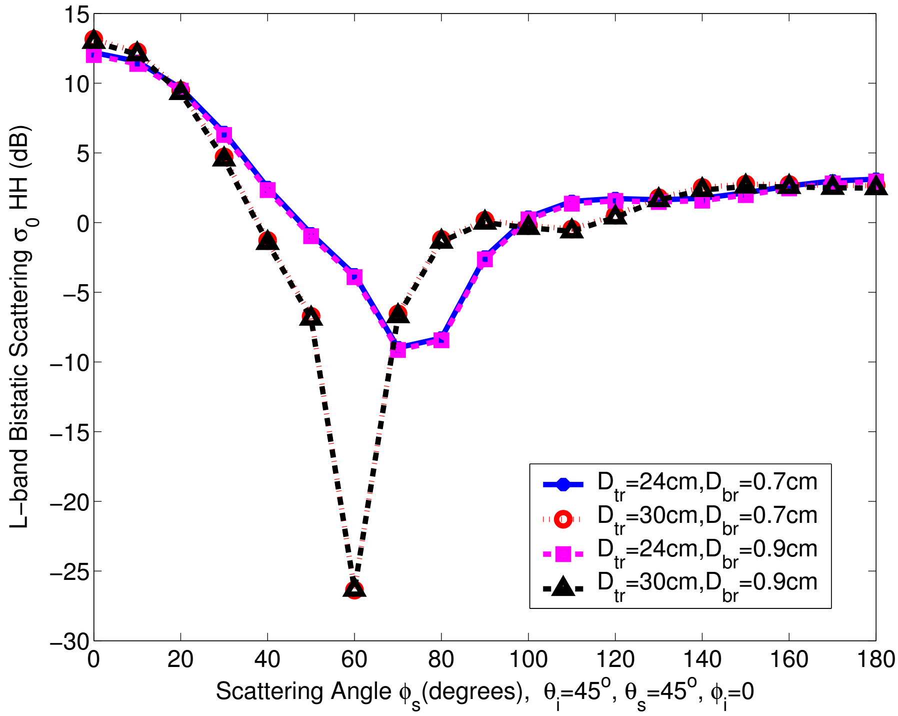

Figure 2.12: L-band HH-polarized canopy scattering cross section vs. scattering angle for four aspen stands. $\theta_s = \theta_i = 45°$, and the azimuth angle ϕ_s is form 0 to 180°.

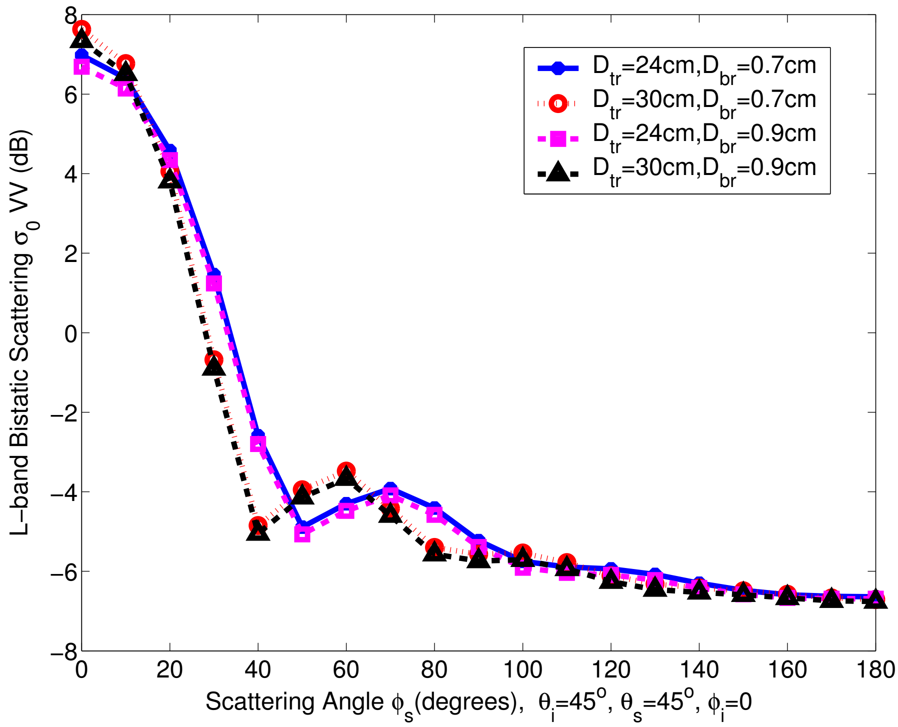

Figure 2.13: L-band VV-polarized canopy scattering cross section vs. scattering angle for four aspen stands. $\theta_s = \theta_i = 45°$, and the azimuth angle ϕ_s is form 0 to 180°.

L-band HH-polarized bistatic simulation results for the four aspen stands are shown in Figure 2.12. The direction $\phi_s = 0$ is the specular direction and $\phi_s = 180°$ stands for backscattering. In the backscattering and specular scattering directions, the changes of biomass can not be captured by the simulated scattering coefficient σ^0. However, large differences among the four curves are observed at the ϕ_s range of $30° \sim 100°$. Most of the differences of σ^0 are contributed by trunk and ground interaction scattering. Figure 2.12 also indicates that they are trunk-dominated canopies since the different branch sizes have little effect on the total scattering level, which is the reason that we can not distinguish the two curves with same trunk diameters but different branch diameters. Larger biomass density doesn't always generate high scattering coefficient as shown in Figure 2.12, where the stands with small trunk diameters have larger σ^0 at angles of $30° \leq \phi_s < 70°$ and $100° \leq \phi_s \leq 120°$. However, there is not significant improvement to distinguish four stands using VV-polarized bistatic measurement as demonstrated by Figure 2.13, where the difference between the four curves has a small dynamic range with respect to the angle.

2.4.3.2 White Spruce Stands

A similar approach is applied to four white spruce stands as in the last section, however, instead of changing the tree size parameters, we reduce the tree density from 2000 trees/ha to 1000 trees/ha, 6667 trees/ha and 500 trees/ha. Therefore, we have four stands of white spruce with the parameters listed in Table 2.1 except for the tree number density. This experiment is to simulate the Forest density's effect on bistatic RCS. By decreasing the tree number density, we decrease the biomass density of the stands. The L-band HH-polarized simulation results in the specu-

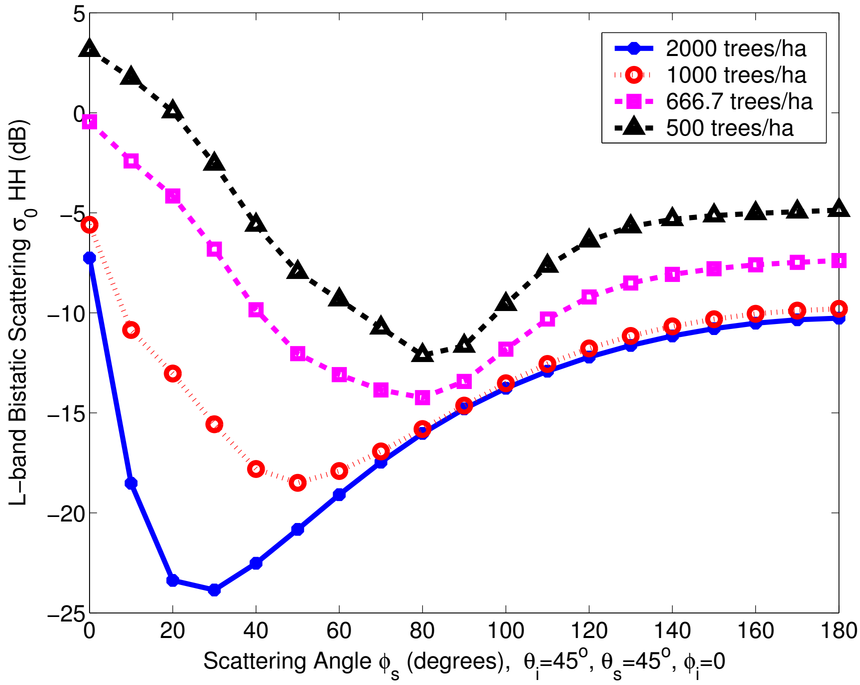

Figure 2.14: L-band HH-polarized canopy scattering cross section vs. scattering angle for four white spruce stands. $\theta_s = \theta_i = 45°$, and the azimuth angle ϕ is form 0 to 180°.

lar direction cone surface are shown in Figure 2.14. The largest dynamic range 21.3dB occurs around $\phi_s = 30°$, which indicates that for these four stands of white spruce, the biomass differences can best be captured at $\phi_s = 30°$. The dynamic range for backscattering coefficients are 6.6 dB and 10.4dB for specular scattering. The smallest dynamic range is found to be 2.1dB at $\phi_s = 90°$, therefore, it would be inappropriate to place a receiver in the plane perpendicular to the incident direction for HH-polarized scattering coefficients if trying to measure biomass. The VH-polarized bistatic scattering coefficient is also shown to be sensitive to the variation of tree density as shown in Figure 2.15.

It is note worthy that the increased biomass density does not always cause higher microwave scattering. In Figure 2.14, the stand with the highest tree density has the lowest scattering coefficient while the stand with the lowest tree density has the

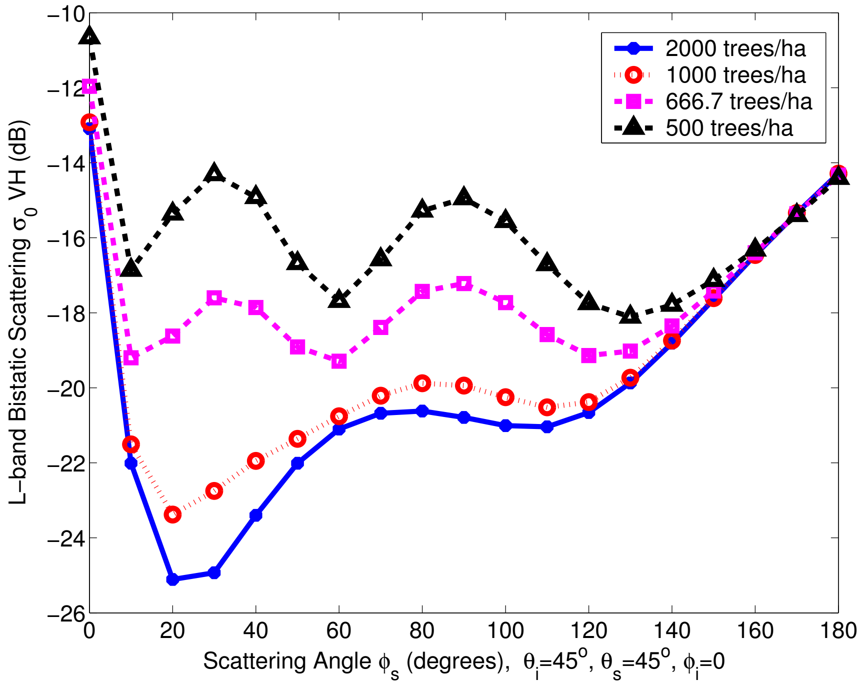

Figure 2.15: L-band VH-polarized canopy scattering cross section vs. scattering angle for four white spruce stands. $\theta_s = \theta_i = 45°$, and the azimuth angle ϕ_s is form 0 to 180°.

strongest scattering coefficient. To explain this phenomenon, we need to probe into the complete scattering process of the forest canopy.

Less dense crown layers cause less attenuation from the upper level canopy, more energy can penetrate the crown layer and so the trunk layer's contribution becomes more important. As a result, we expect more scattering from less dense canopy stands if large tree trunks are present. Moreover, with fewer trunks, the ground reflection of the crown scattering experiences less attenuation, as does the double bounce crown scattering component. In addition, there is more ground scattering through the sparse canopies. All these factors together cancel the effect of the low tree density, hence increasing the total canopy scattering.

Figure 2.16 shows the L-band HH-polarized canopy scattering component contributions to the total scattering for all stands in the specular direction cone surface.

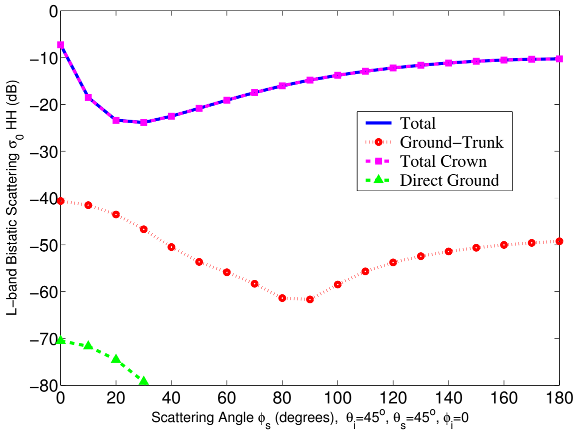

(a) 2000 tree/ha

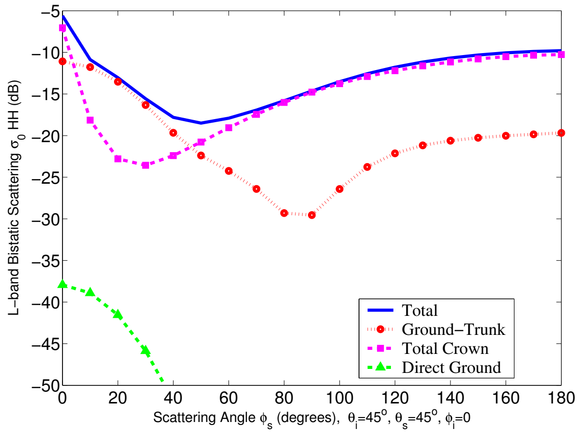

(b) 1000 trees/ha

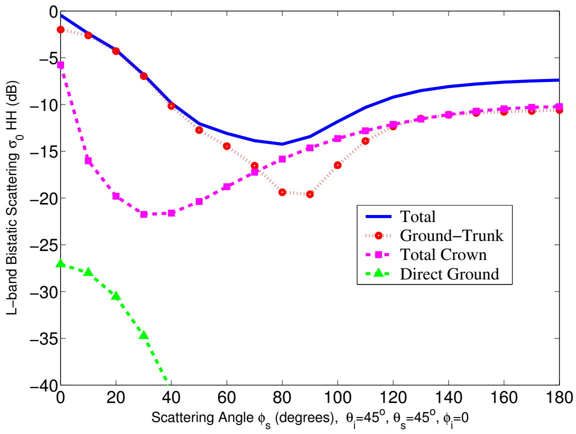

(c) 666.7 trees/ha

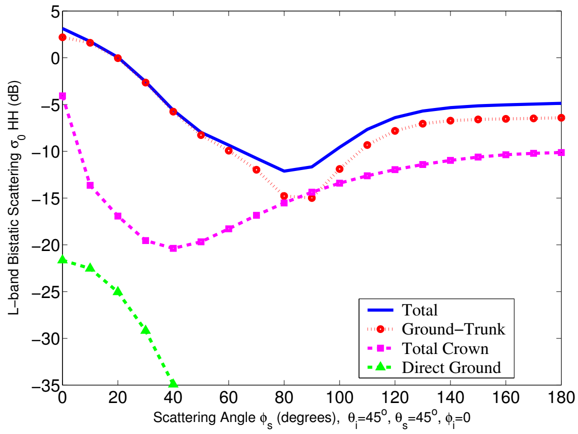

(d) 500 trees/ha

Figure 2.16: L-band HH-polarized canopy scattering component contributions vs. scattering angle for four white spruce stands. $\theta_s = \theta_i = 45°$, and the azimuth angle ϕ_s is form 0 to 180°.

In Figure 2.16(a), the large tree number density (2000 tree/ha) makes the stand a crown-dominated canopy, and the scattering from the trunk layer and ground are almost negligible. However, at half of this tree density (1000 tree/ha), the crown layer scattering contribution decreases, while the trunk layer scattering contribution increases, especially at small angles as shown in Figure 2.16(b). When we further decrease the tree density (667 trees/ha), the trunk's contribution becomes more significant as shown in Figure 2.16(c). Finally in Figure 2.16(d), with only a quarter of the original tree density (500 trees/ha), the canopy becomes a trunk dominated canopy and the crown scattering becomes almost negligible. The ground surface scattering also rises as we decrease the canopy density, however, it is still very low compared to the trunk and crown layer scattering.

Not only do the canopies change from crown dominant to trunk dominant, the four components of crown scattering contributions also change. We plot the component contribution within the crown layer in Figure 2.17. As can be seen from Figure 2.17(a), direct scattering from the crown layer is the major contributor for the dense stand, the double bounce effect is too insignificant to be shown in the plot. In Figure 2.17(b), the direct crown scattering is still dominant, but the crown-ground interaction scattering increases. In Figure 2.17(c), the direct scattering and the crown-ground interaction are comparable for small ϕ_s angles. As in Figure 2.17(d), the crown ground scattering exceeds the direct crown scattering for small ϕ_s angles and the double bounce scattering is much higher. The ground-crown-ground double bounce scattering is the weakest for all four cases.

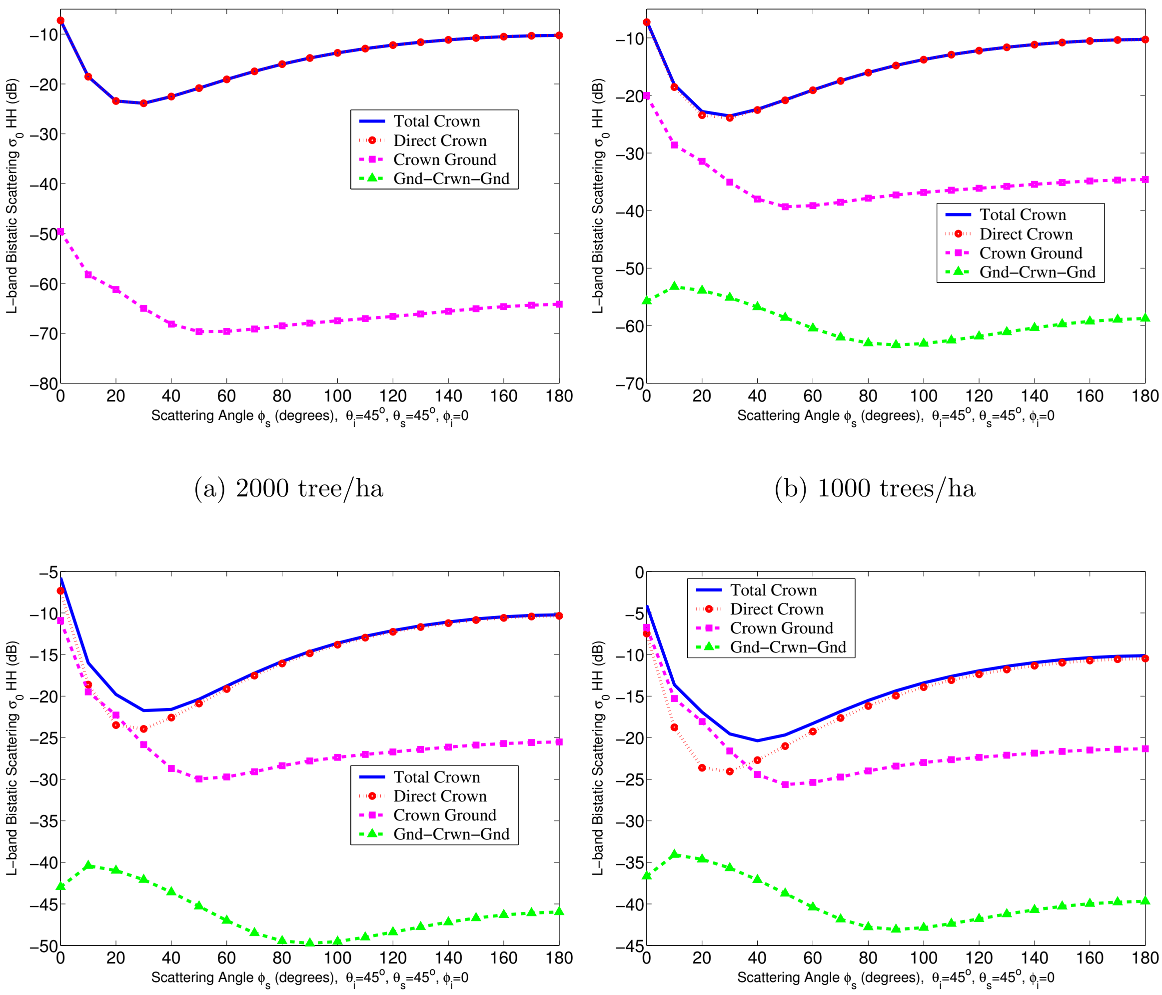

(a) 2000 tree/ha

(b) 1000 trees/ha

(c) 666.7 trees/ha

(d) 500 trees/ha

Figure 2.17: L-band HH-polarized crown component scattering contributions vs. scattering angle for four white spruce stands. $\theta_s = \theta_i = 45°$, and the azimuth angle ϕ_s is form 0 to 180°.

2.4.4 Discussion

We use the same canopy stands as in the technical report on backscattering MIMICS [86] to validate our bistatic scattering model for the the special case of backscattering. Simulation results by the two models are shown to be consistent.

Bistatic RCS provides significantly much more information about the mechanisms of canopy scattering and composition compared to backscattering RCS. When $\theta_s = \theta_i$ is fixed and the azimuth angle ϕ_s is rotated around the target, the largest bistatic RCS is generally found at the specular receiving angles. For the trunk layer, HH-polarized trunk-ground interaction scattering is the strongest in the specular direction and weakest around the plane perpendicular to the incident direction. In contrast, VV-polarized trunk-ground scattering shows a slow decreasing trend as the scattering angle ϕ_s changes from the specular direction to the backscattering direction.

Specular scattering from the rough ground surface is the greatest, whereas the direct backscattering from the ground is the lowest. The rough surface also causes more scattering at the small elevation angles ($\theta_s < 20°$) and less scattering at the large elevation angles ($\theta_s > 50°$). The ground effect on the total scattering cross section is larger at low frequencies where there is less attenuation by the crown and trunk layer.

Bi-MIMICS shows distinct sensitivities to the dimensions, density, angular distribution, and permittivity of the forest components and also to ground surface attributes. Changes of the parameters cause the canopy dominant components to vary and the scattering compositions to change. Bistatic RCS offers more information than backscattering RCS due to the additional dimensions. Model simulations show that there are optimal angles for extracting canopy parameters that are superior to the backscattering angles, which are determined by the canopy composition and parameter distribution.

The simulation results presented in this chapter represent a first order RT-based model. The current first order solution doesn't include multiple scattering mechanisms among scatterers; the coherent effects, such as enhanced backscatter, are not therefore considered. However, multiple scattering among canopy elements is expected, particularly at high frequencies, where branch and foliage volume scattering dominates, and may cause an underestimation of RCS at high frequencies.

At this moment, no actual bistatic SAR measurement data from vegetation are available to us for comparison with the model's simulation. Our future work includes conducting bistatic radar measurements on scaled forest models using our existing bistatic measurement facilities.

2.5 Conclusion

Forest scattering modeling provides a tool to study the relationship between radar measurement and forest structures by simulating the scattering processing of microwave interaction with different components of the forest. In this chapter, we present a bistatic microwave scattering model, which complements the existing backscattering MIMICS. It is based on RT theory and is designed to accommodate the bistatic scattering simulation capability in anticipation of perspective bistatic radar systems.

Bi-MIMICS simulates SAR bistatic scattering for forest canopies characterized by input dimensional, geometrical, and dielectric parameters. As such, the model can be used to analyze the relationship between canopy parameters and the scattering coefficient, especially with the advantage of multiple observation angles. From the model, differences in tree height, moisture content, and biomass can be simulated by simply changing the model inputs and by analyzing the contribution of each individual layer to the bistatic RCS.

Bi-MIMICS is parameterized to selected tree canopies with different canopy structures and density. A number of bistatic RCS values are simulated at various bistatic angles. The simulation results demonstrate the bistatic scattering mechanisms and the potential application of bistatic measurement. Scattering behavior of canopy components are varied with respect to the bistatic geometry to show their respective sensitivities.

Radar response at multiple measurement angles, in addition to multiple frequencies and polarizations, can be used to study the potential retrieval of forest biomass and other vegetation parameters, which is the goal of our ongoing work. Our future work also includes performing laboratory bistatic measurement for model validation, and extending the current solution to higher orders.

Bi-MIMICS prepares us for the next chapter, in which a multi-layer canopy scattering model is developed and it accommodates the bistatic scattering simulation ability.

Chapter III

MULTI-MIMICS FOR MIXED SPECIES FORESTS

In this chapter, a multi-layer canopy scattering model is developed for mixed species forests. The multi-layer canopy model represents nonuniform forests in the vertical direction and provides a significantly enhanced representation of actual complex forest structures compared to the conventional canopy-trunk layer models. Multi-layer Michigan Microwave Canopy Scattering model (Multi-MIMICS) allows overlapping layer configuration and a tapered trunk model applicable to forests of mixed species and/or mixed growth stages. The multi-layer model is the first order solution to a set of radiative transfer equations and includes layer interactions between overlapping layers. Bistatic scattering mechanisms are included in the model as a successor to Bi-MIMICS. It simulates SAR bistatic scattering coefficients based on input dimensional, geometrical and dielectric variables of forest canopies. Multiple canopy layers are divided by vertically grouping the forest scattering components with relatively uniform distributions and densities. The number of layers are decided by the best representation of the actual canopy composition.

The first section in the chapter provides a brief background and motivation of developing Multi-MIMICS. Section 3.2 presents the multi-layer canopy model and solves radiative transfer equations while Section 3.3 analyzes the first order Multi-MIMICS solution and model's applicability of complex canopy structures — overlapping layers and tapered trunks. The implementation of Multi-MIMICS is then presented Section 3.4. Finally, Section 3.5 summarizes the chapter.

3.1 Introduction

Most existing canopy scattering models are developed for single stand canopies and have therefore been validated on and applied to single forest stand or stands with similar structures where a distinctive line can be drawn between the crown layer and the trunk layer. The models are not applicable to forest stands of mixed species composition and structure where multiple layers occur such as the overstory, understory and shrubs. For this reason, our research has focused on the development of a multi-layer model, herein referred to as the Multi-Layer Michigan Microwave Canopy Scattering (Multi-MIMICS) model. As it's name suggests, the model is based on the original two-layer MIMICS model. As with its predecessor and other models, the canopy modeling still utilizes the discrete scatterer approach. However, the layers are instead divided by vertically grouping the forest scattering components with relatively uniform distributions and densities. The RT-based model can handle multiple layers, with the number dependent on what best represents the actual canopy composition. Unlike other models, overlapping between layers is allowed and a tapered trunk model has been introduced.

Multiple layer RT equations are generally used to study thermodynamics of the atmosphere, which emphases the frequency dependence. The only other multilayer canopy modeling we are aware of is of [62], which differs from Multi-MIMICS in the following aspects:

- Multi-MIMICS addresses the vertical heterogeneity of mixed-stand forests while [62] emphasizes the multiple scattering for cross-polarized backscattering coefficients σ^0;

- Multi-MIMICS is the first order full polarimetric solution to the integral form of the RT equation and is solved by an iterative approach. The solution also contains several scattering terms that have definite physical interpretations. Higher order solutions are necessary for more multiple scattering mechanisms and have more terms in the formulation; the DOEM method uses the differential form of the RT equation and solves it directly. Multiple layer structure is a necessity to build the differential RT equation. Although DOEM is free of the limitation of order, its formulation cannot be decomposed into scattering mechanisms nor readily interpreted. Furthermore, it only gives cross polarized HV σ^0 from the even mode solution; HH and VV σ^0 are not provided;

- Canopy layers in Multi-MIMICS are allowed to overlap and therefore provide a better representation of the vertical complexity of the canopy. DOEM, by contrast, divides the canopy for mathematical computation and does not include overlapping layers;

- Tapered trunks are especially treated in Multi-MIMICS for correlated positions among layers whereas DOEM doesn't consider the correlation factor.

Multi-MIMICS simulates SAR bistatic scattering for forest canopies characterized by input dimensional, geometrical, and dielectric parameters. As such, the model can be used to analyze the relationship between canopy parameters and bistatic scattering coefficient, especially applied to natural forest where stands commonly contain a mix of structures as a consequence of their species composition, growth stage, competition between individuals and environmental conditions (e.g., soil, topography). The multi-layered nature of the scattering model means that Multi-MIMICS is a more efficient realization of the actual forest structure and can be shaped for any specific arrangement of forest parameters. From the model, differences in tree height, moisture content and biomass can be simulated by simply changing the model inputs and by analyzing the contribution of each individual layer, a better understanding of forest composition effects on scattering coefficients can be gained.

3.2 Multi-layer Canopy Model and Radiative Transfer Equations

3.2.1 Mixed Forest Structures and Multi-layer Canopy Model

The motivation for developing multi-MIMICS is that the crown-trunk-ground canopy model is too restrictive for actual forests, particularly those that are in a relatively natural state. In these forests, a mixture of different tree species occur and groups of these differ in their structural form. As a result, trees are of varying density, size and height; trunks of taller trees overlap with the crowns of short trees; extended trunks grow into crown layers. The understory level is typically composed of saplings, immature trees and/or tall shrubs that are often completely submerged under the canopy. In many cases, these can be divided further into two distinct layers (crowns and trunks). Above the understory, several layers of trees may occur, with each supporting a crown and trunk layer. Trunks and crowns may extend between layers. In such cases, it is extremely difficult to describe the forest in terms of just a crown and a trunk layer as the forest is simply too complex. The complex nature of these mixed forests is highlighted in Figure 3.1 [7], which shows a picture of a primary tropical rain forest. The forest would be vertically modeled as five layers, which are the overstory, the canopy, the understory, the shrub layer, and the forest

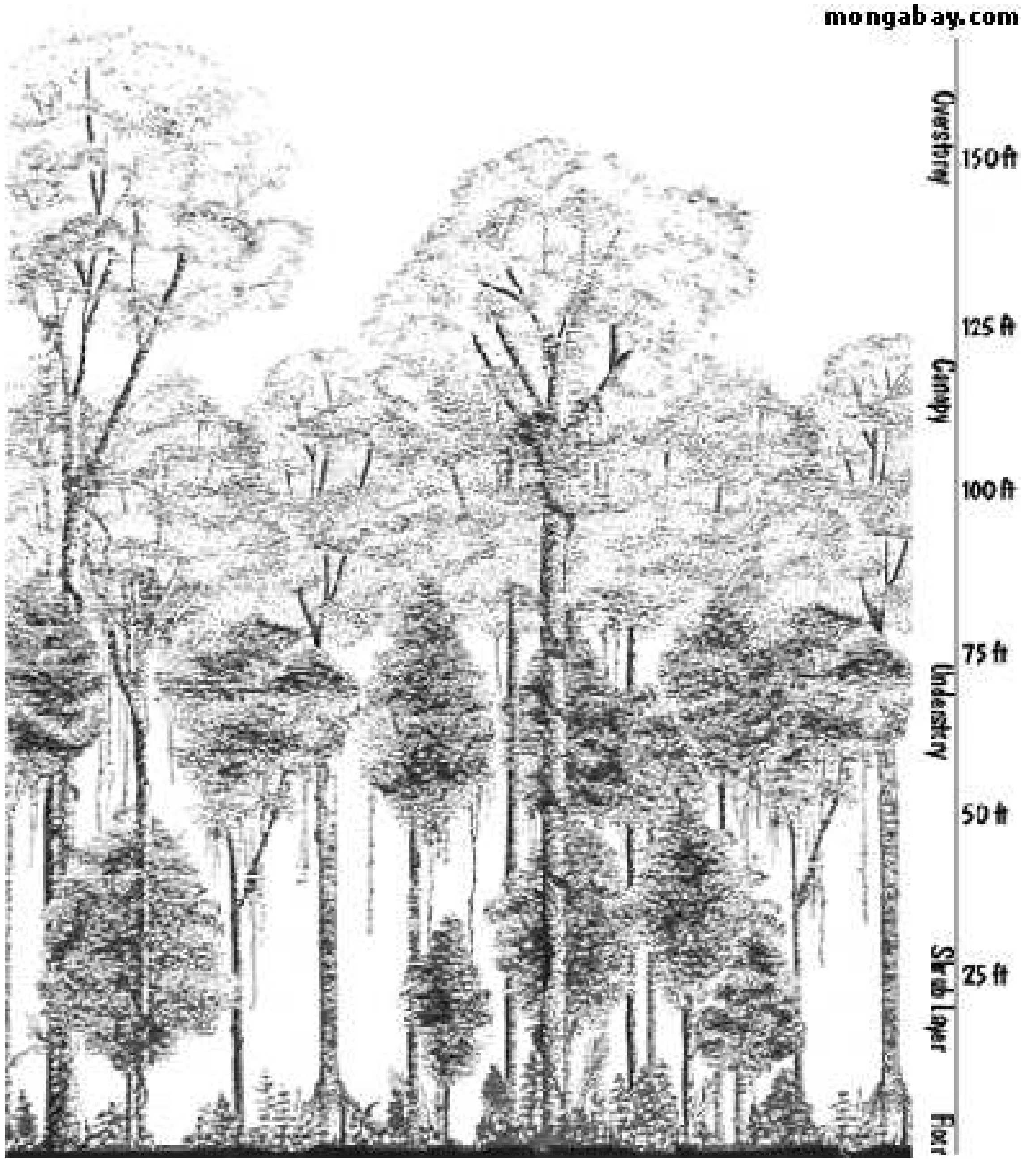

Figure 3.1: Layer properties of a tropical rain forest.
Source: http://www.mongabay.com/0401.htm.

floor.

The conventional models are therefore inappropriate for application to natural forests. For this reason, we develop the Multi-MIMICS model to remove the two-layer canopy restriction. Furthermore, there was also a need to handle an arbitrary number of layers depending upon the complexity of the forest. Rather than assigning definite names to the layers, we chose to divide the forest volume into multiple vertical layers and treat all layers as part of the vertical profile. Within each layer, any combination of branches, foliage or trunks can occur. While the composition of each layer is distinct from the others, the type and distribution of scatterers inside each are considered to be homogeneous.

Multi-MIMICS allows overlapped layers to account for the situations such as the mixtures of tall tree trunks and short tree crowns and trunk growing into crown. Furthermore, instead of using a uniform stem truncated at the crown layer bottom as in the Bi-MIMICS, a tapered trunk model is introduced by cascading layers with increasing trunk radius.

3.2.2 Multi-layer Radiative Transfer Equations and First Order Solution

To solve the RT equations of Multi-MIMICS, we use an L-layer canopy over a reflective ground surface model as shown in Figure 3.2. The depth of the $l-th$ layer is denoted by d_l. Overlapping layers are not included in the derivation of first order solution. The incident intensity $\mathbf{I}_i$ impinges on the top surface of the canopy at an angle (θ_i, ϕ_i). To obtain the scattering intensity $\mathbf{I}_s(\theta_s, \phi_s)$, we need to solve the RT equations of all layers.

To describe the RT mechanism mathematically, we denote the upward radiation intensity in each layer by $\mathbf{I}_l^+$ and the downward radiation intensity by $\mathbf{I}_l^-$ with l as

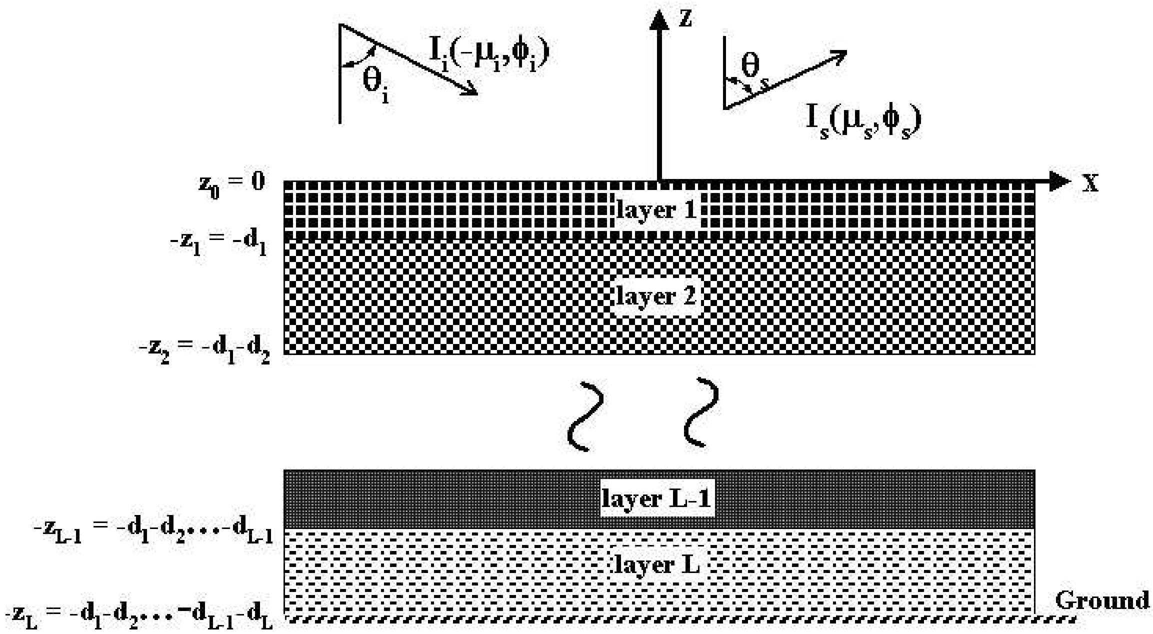

Figure 3.2: Multi-layer canopy model. The canopy is divided into L layers with labels $1, 2, ...l, ..., L$. The depth of the $l - th$ layer is denoted by d_l. Top canopy surface is located at $z = 0$ and the ground surface is at $-(d_1 + d_2 + ... + d_L)$. The microwave incidence angle is (θ_i, ϕ_i) and the scattering angle is (θ_s, ϕ_s).

the layer index. Similarly, $\mathcal{F}_l^+$ and $\boldsymbol{\kappa}_l^+$ and $\mathcal{P}_l^+$ represent the upward radiation source function, extinction matrix and phase matrix respectively; and $\mathcal{F}_l^-$ and $\boldsymbol{\kappa}_l^-$ and $\mathcal{P}_l^-$ are for downward expressions.

The radiation intensities in all layers of the L-layer canopy model make up a set of RT equations. The interfaces among canopy layers and air-canopy interface are assumed diffuse, thus we have the boundary conditions that the intensities across the interfaces are continuous. These boundary conditions are

$$\mathbf{I}_1^-(-\mu_s, \phi_s, 0) = \mathbf{I}_i^-(-\mu_i, \phi_i, 0)\delta(\mu_s - \mu_i)\delta(\phi_s - \phi_i) \tag{3.1}$$

$$\mathbf{I}_l^-(-\mu_s, \phi_s, -z_l) = \mathbf{I}_{l+1}^-(-\mu_s, \phi_s, -z_l) \qquad 1 < l < L \tag{3.2}$$

$$\mathbf{I}_L^+(\mu_s, \phi_s, -z_L) = \mathcal{R}(\mu_s)\mathbf{I}_L^-(-\mu_s, \phi_s, -z_L) \tag{3.3}$$

$$\mathbf{I}_l^+(\mu_s, \phi_s, -z_l) = \mathbf{I}_{l+1}^+(\mu_s, \phi_s, -z_l) \qquad 1 < l < L \tag{3.4}$$

$$\mathbf{I}_s(\mu_s, \phi, 0) = \mathbf{I}_1^+(\mu_s, \phi_s, 0) \tag{3.5}$$

Equation (3.1) indicates that the downward intensity at top surface of the canopy is the incident intensity that impinges on the canopy. Equation (3.2) shows that the downward intensities at the bottom of the up layer is equal to that at the top of the lower layer. Ground reflection of the downward intensity is represented by Equation (3.3). Equation (3.4) explains that the upward intensities are continuous across the canopy interfaces and Equation (3.5) shows the upward intensity at the top surface is the total scattered intensity.

By applying the boundary conditions, the downward intensity in Layer 1 is written as

$$\begin{aligned}\mathbf{I}_1^-(-\mu_s, \phi_s, z) &= e^{\boldsymbol{\kappa}_1^- z/\mu_s}\mathbf{I}_i(-\mu_i, \phi_i, 0)\delta(\mu_s - \mu_i)\delta(\phi_s - \phi_i) \\ &\quad + \int_z^0 e^{\boldsymbol{\kappa}_1^-(z-z')/\mu_s}\mathcal{F}_1^-(-\mu_s, \phi_s, z')\mathrm{d}z' \end{aligned} \tag{3.6}$$

The first part in Equation (3.6) represents the extinction process in Layer 1 while the second part shows the emission process. The incident intensity is attenuated along the propagation path by extinction, and the emitted intensity by Layer 1 in the desired direction is integrated over the depth of the layer. The emission is cause by canopy scattering that transforms the wave intensity in all directions to the desired direction.

The wave then propagates into Layer 2

$$\begin{aligned}
\mathbf{I}_2^-(-\mu_s,\phi_s,z) &= e^{\boldsymbol{\kappa}_2^-(z+z_1)/\mu_s}\mathbf{I}_1^-(-\mu_s,\phi_s,-z_1) + \int_z^{-z_1} e^{\boldsymbol{\kappa}_2^-(z-z')/\mu_s}\mathcal{F}_2^-(-\mu_s,\phi_s,z')\mathrm{d}z' \\
&= e^{\boldsymbol{\kappa}_2^-(z+z_1)/\mu_s}e^{-\boldsymbol{\kappa}_1^- d_1/\mu_s}\mathbf{I}_i(-\mu_i,\phi_i,0)\delta(\mu_s-\mu_i)\delta(\phi_s-\phi_i) \\
&\quad + e^{\boldsymbol{\kappa}_2^-(z+z_1)/\mu_s}\int_{-z_1}^{0} e^{-\boldsymbol{\kappa}_1^-(z_1+z')/\mu_s}\mathcal{F}_1^-(-\mu_s,\phi_s,z')\mathrm{d}z' \\
&\quad + \int_z^{-z_1} e^{\boldsymbol{\kappa}_2^-(z-z')/\mu_s}\mathcal{F}_2^-(-\mu_s,\phi_s,z')\mathrm{d}z' \qquad (3.7)
\end{aligned}$$

Similar extinction and emission processes as in Layer 1 are applied to Layer 2, the continuous boundary condition $\mathbf{I}_2^-(-\mu_s,\phi_s,-z_1) = \mathbf{I}_1^-(-\mu_s,\phi_s,-z_1)$ is used as the initial condition.

As downward intensity travels down into lower layers , the terms in the representation increases, in the $3rd$ layer

$$\begin{aligned}
\mathbf{I}_3^-(-\mu_s,\phi_s,z) &= e^{\boldsymbol{\kappa}_3^-(z+z_2)/\mu}\mathbf{I}_2^-(-\mu_i,\phi_i,-z_2) + \int_z^{-z_2} e^{\boldsymbol{\kappa}_3^-(z-z')/\mu_s}\mathcal{F}_3^-(-\mu_s,\phi_s,z')\mathrm{d}z' \\
&= e^{\boldsymbol{\kappa}_3^-(z+z_2)/\mu_s}e^{-\boldsymbol{\kappa}_2^- d_2/\mu_s}e^{-\boldsymbol{\kappa}_1^- d_1/\mu_s}\mathbf{I}_i(-\mu_i,\phi_i,0)\delta(\mu_s-\mu_i)\delta(\phi_s-\phi_i) \\
&\quad + e^{\boldsymbol{\kappa}_3^-(z+z_2)/\mu_s}e^{-\boldsymbol{\kappa}_2^- d_2/\mu_s}\int_{-z_1}^{0} e^{-\boldsymbol{\kappa}_1^-(z_1+z')/\mu_s}\mathcal{F}_1^-(-\mu_s,\phi_s,z')\mathrm{d}z' \\
&\quad + e^{\boldsymbol{\kappa}_3^-(z+z_2)/\mu_s}\int_{-z_2}^{-z_1} e^{-\boldsymbol{\kappa}_2^-(z_2+z')/\mu_s}\mathcal{F}_2^-(-\mu_s,\phi_s,z')\mathrm{d}z' \\
&\quad + \int_z^{-z_2} e^{\boldsymbol{\kappa}_3^-(z-z')/\mu_s}\mathcal{F}_3^-(-\mu_s,\phi_s,z')\mathrm{d}z' \qquad (3.8)
\end{aligned}$$

Finally, the total downward intensity in the bottom layer has $L+1$ terms to account for the extinction attenuation and scattering of the incident intensity along the propagation path

$$
\begin{aligned}
\mathbf{I}_L^-(-\mu_s,\phi_s,z) &= e^{\boldsymbol{\kappa}_L^-(z+z_{L-1})/\mu_s}\mathbf{I}_{L-1}^-(-\mu_i,\phi_i,-z_{L-1}) \\
&+ \int_z^{-z_{L-1}} e^{\boldsymbol{\kappa}_L^-(z-z')/\mu_s}\mathcal{F}_L^-(-\mu_s,\phi_s,z')\mathrm{d}z' \\
= \quad & e^{\boldsymbol{\kappa}_L^-(z+z_{L-1})/\mu_s}\Big(\prod_{m=1}^{L-1} e^{-\boldsymbol{\kappa}_l^- d_l/\mu_s}\Big)\mathbf{I}_i(-\mu_i,\phi_i,0)\delta(\mu_s-\mu_i)\delta(\phi_s-\phi_i) \\
&+ e^{\boldsymbol{\kappa}_L^-(z+z_{L-1})/\mu_s}\Big(\prod_{l=2}^{L-1} e^{-\boldsymbol{\kappa}_l^- d_l/\mu_s}\Big)\int_{-z_1}^{0} e^{-\boldsymbol{\kappa}_1^-(z_1+z')/\mu_s}\mathcal{F}_1^-(-\mu_s,\phi_s,z')\mathrm{d}z' \\
&+ e^{\boldsymbol{\kappa}_L^-(z+z_{L-1})/\mu_s}\Big(\prod_{l=3}^{L-1} e^{-\boldsymbol{\kappa}_l^- d_l/\mu_s}\Big)\int_{-z_2}^{-z_1} e^{-\boldsymbol{\kappa}_2^-(z_2+z')/\mu_s}\mathcal{F}_2^-(-\mu_s,\phi_s,z')\mathrm{d}z' \\
&+ \cdots \\
&+ e^{\boldsymbol{\kappa}_L^-(z+z_{L-1})/\mu_s}e^{-\boldsymbol{\kappa}_{L-1}^- d_{L-1}/\mu_s}\int_{-z_{L-2}}^{-z_{L-3}} e^{-\boldsymbol{\kappa}_{L-2}^-(z_{L-2}+z')/\mu_s}\mathcal{F}_{L-2}^-(-\mu_s,\phi_s,z')\mathrm{d}z' \\
&+ e^{\boldsymbol{\kappa}_L^-(z+z_{L-1})/\mu_s}\int_{-z_{L-1}}^{-z_{L-2}} e^{-\boldsymbol{\kappa}_{L-1}^-(z_{L-1}+z')/\mu_s}\mathcal{F}_{L-1}^-(-\mu_s,\phi_s,z')\mathrm{d}z' \\
&+ \int_z^{-z_{L-1}} e^{\boldsymbol{\kappa}_L^-(z-z')/\mu_s}\mathcal{F}_L^-(-\mu_s,\phi_s,z')\mathrm{d}z' \\
= \quad & e^{\boldsymbol{\kappa}_L^-(z+z_{L-1})/\mu_s}\Big(\prod_{m=1}^{L-1} e^{-\boldsymbol{\kappa}_l^- d_l/\mu_s}\Big)\mathbf{I}_i(-\mu_i,\phi_i,0)\delta(\mu_s-\mu_i)\delta(\phi_s-\phi_i) + e^{\boldsymbol{\kappa}_L^-(z+z_{L-1})/\mu_s} \\
& \sum_{m=1}^{L-1}\Big[\Big(\prod_{l=m+1}^{L-1} e^{-\boldsymbol{\kappa}_l^- d_l/\mu_s}\Big)\int_{-z_m}^{-z_{m-1}} e^{-\boldsymbol{\kappa}_m^-(z_m+z')/\mu_s}\mathcal{F}_m^-(-\mu_s,\phi_s,z')\mathrm{d}z'\Big] \\
&+ \int_z^{-z_{L-1}} e^{\boldsymbol{\kappa}_L^-(z-z')/\mu_s}\mathcal{F}_L^-(-\mu_s,\phi_s,z')\mathrm{d}z' \qquad (3.9)
\end{aligned}
$$

So at the ground surface $z=-z_L$, the downward intensity becomes

$$
\begin{aligned}
\mathbf{I}_L^-(-\mu_s,\phi_s,-z_L) \; &= \; \Big(\prod_{m=1}^{L} e^{-\boldsymbol{\kappa}_l^- d_l/\mu_s}\Big)\mathbf{I}_i(-\mu_i,\phi_i,0)\delta(\mu_s-\mu_i)\delta(\phi_s-\phi_i) \\
&+ \sum_{m=1}^{L}\Big[\Big(\prod_{l=m+1}^{L} e^{-\boldsymbol{\kappa}_l^- d_l/\mu_s}\Big)\int_{-z_m}^{-z_{m-1}} e^{-\boldsymbol{\kappa}_m^-(z_m+z')/\mu_s}\mathcal{F}_m^-(-\mu_s,\phi_s,z')\mathrm{d}z'\Big] \qquad (3.10)
\end{aligned}
$$

Ground specular reflection occurs at the ground surface $z=-z_L$ by the reflectivity matrix $\mathcal{R}(\mu_s)$, and the upward intensity in the bottom layer is

$$\begin{aligned}
\mathbf{I}_L^+(\mu_s, \phi_s, z) &= e^{-\boldsymbol{\kappa}_L^+(z+z_L)/\mu_s}\mathbf{I}_L^+(-\mu_s, \phi_s, -z_L) \\
&\quad + \int_{-z_L}^{z} e^{-\boldsymbol{\kappa}_L^+(z-z')/\mu_s}\mathcal{F}_L^+(\mu_s, \phi_s, z')\mathrm{d}z'
\end{aligned} \tag{3.11}$$

where the initial condition $\mathbf{I}_L^+(-\mu_s, \phi_s, -z_L)$ is solve by

$$\mathbf{I}_L^+(-\mu_s, \phi_s, -z_L) = \mathcal{R}_f(\mu_s)\mathbf{I}_L^-(-\mu_s, \phi_s, -z_L) \tag{3.12}$$

and the reflectivity matrix $\mathcal{R}_f(\mu_s)$ at incidence angle θ_s of the specular ground surface is given by

$$\mathcal{R}(\mu_s) = \begin{bmatrix} |r_v|^2 & 0 & 0 & 0 \\ 0 & |r_h|^2 & 0 & 0 \\ 0 & 0 & \mathrm{Re}(r_v r_h^*) & -\mathrm{Im}(r_v r_h^*) \\ 0 & 0 & \mathrm{Im}(r_v r_h^*) & \mathrm{Re}(r_v r_h^*) \end{bmatrix} \tag{3.13}$$

where r_v and r_h are the specular reflectivity coefficients at vertical and horizontal polarizations, respectively.

Like the downward intensity, the upward intensity undergoes the similar extinction and scattering process. The upward intensity in Layer $L-1$ is

$$\begin{aligned}
\mathbf{I}_{L-1}^+(\mu_s, \phi_s, z) &= e^{-\boldsymbol{\kappa}_{L-1}^+(z+z_{L-1})/\mu_s}\mathbf{I}_L^+(\mu_s, \phi_s, -z_{L-1}) \\
&\quad + \int_{-z_{L-1}}^{z} e^{-\boldsymbol{\kappa}_{L-1}^+(z-z')/\mu_s}\mathcal{F}_{L-1}^+(\mu_s, \phi_s, z')\mathrm{d}z' \\
&= e^{-\boldsymbol{\kappa}_{L-1}^+(z+z_{L-1})/\mu_s}e^{-\boldsymbol{\kappa}_L^+(z+z_L)}\mathcal{R}_f(\mu_s)\mathbf{I}_L^-(-\mu_s, \phi_s, -z_L) \\
&\quad + e^{-\boldsymbol{\kappa}_{L-1}^+(z+z_{L-1})/\mu_s}\int_{-z_L}^{z_{L-1}} e^{-\boldsymbol{\kappa}_L^+(z-z')/\mu_s}\mathcal{F}_L^+(\mu_s, \phi_s, z')\mathrm{d}z' \\
&\quad + \int_{-z_{L-1}}^{z} e^{-\boldsymbol{\kappa}_{L-1}^+(z-z')/\mu_s}\mathcal{F}_{L-1}^+(\mu_s, \phi_s, z')\mathrm{d}z'
\end{aligned} \tag{3.14}$$

Then in the next upper layer, four terms are in this layer's RT equation

$$
\begin{aligned}
\mathbf{I}^+_{L-2}(\mu_s,\phi_s,z) &= e^{-\boldsymbol{\kappa}^+_{L-2}(z+z_{L-2})/\mu_s}\mathbf{I}^+_{L-1}(\mu_s,\phi_s,-z_{L-2}) \\
&+ \int_{-z_{L-2}}^{z} e^{-\boldsymbol{\kappa}^+_{L-2}(z-z')/\mu_s}\mathcal{F}^+_{L-2}(\mu_s,\phi_s,z')\mathrm{d}z' \\
= \quad & e^{-\boldsymbol{\kappa}^+_{L-2}(z+z_{L-2})/\mu_s}e^{-\boldsymbol{\kappa}^+_{L-1}d_{L-1}/\mu_s}e^{-\boldsymbol{\kappa}^+_{L}d_{L}/\mu_s}\mathcal{R}(\mu_s)\mathbf{I}^-_L(-\mu_s,\phi_s,-z_L) \\
&+ e^{-\boldsymbol{\kappa}^+_{L-2}(z+z_{L-2})/\mu_s}e^{-\boldsymbol{\kappa}^+_{L-1}d_{L-1}/\mu_s}\int_{-z_L}^{-z_{L-1}} e^{\boldsymbol{\kappa}^+_{L}(z_{L-1}+z')/\mu_s}\mathcal{F}^+_{L}(\mu_s,\phi_s,z')\mathrm{d}z' \\
&+ e^{-\boldsymbol{\kappa}^+_{L-2}(z+z_{L-2})/\mu_s}\int_{-z_{L-1}}^{-z_{L-2}} e^{\boldsymbol{\kappa}^+_{L-1}(z_{L-2}+z')/\mu_s}\mathcal{F}^+_{L-1}(\mu_s,\phi_s,z')\mathrm{d}z' \\
&+ \int_{-z_{L-2}}^{z} e^{-\boldsymbol{\kappa}^+_{L-2}(z-z')/\mu_s}\mathcal{F}^+_{L-2}(\mu_s,\phi_s,z')\mathrm{d}z' \qquad (3.15)
\end{aligned}
$$

Finally, the total upward intensity in the top layer is composed of $L+1$ terms representing the extinction and scattering of the reflected intensity along the propagation path:

$$
\begin{aligned}
\mathbf{I}^+_{1}(\mu_s,\phi_s,z) &= e^{-\boldsymbol{\kappa}^+_{1}(z+z_1)/\mu_s}\Big(\prod_{l=2}^{L} e^{-\boldsymbol{\kappa}^+_{l}d_l/\mu_s}\Big)\mathcal{R}(\mu_s)\mathbf{I}^-_L(-\mu_s,\phi_s,-z_L) \\
&+ e^{-\boldsymbol{\kappa}^+_{1}(z+z_1)/\mu_s}\sum_{m=2}^{L}\left[\Big(\prod_{l=2}^{m-1} e^{-\boldsymbol{\kappa}^+_{l}d_l/\mu_s}\Big)\int_{-z_m}^{-z_{m-1}} e^{\boldsymbol{\kappa}^+_{m}(z_{m-1}+z')/\mu_s}\mathcal{F}^+_{m}(\mu_s,\phi_s,z')\mathrm{d}z'\right] \\
&+ \int_{-z_1}^{z} e^{-\boldsymbol{\kappa}^+_{1}(z-z')/\mu_s}\mathcal{F}^+_{1}(\mu_s,\phi_s,z')\mathrm{d}z' \qquad (3.16)
\end{aligned}
$$

Then, the canopy scattered intensity is the upward intensity at the top surface $z=0$. In (3.17), it is written in terms of the incident intensity, extinction matrices, reflectivity matrices and source matrices.

$$
\begin{aligned}
\mathbf{I}_1^+(\mu_s,\phi_s,0) &= e^{-\boldsymbol{\kappa}_1^+ d_1/\mu}\Big(\prod_{l=2}^{L} e^{-\boldsymbol{\kappa}_l^+ d_l/\mu_s}\Big)\mathcal{R}(\mu_s)\mathbf{I}_L^-(-\mu_s,\phi_s,-z_L)\\
&+ e^{-\boldsymbol{\kappa}_1^+ d_1/\mu}\sum_{m=2}^{L}\Big[\Big(\prod_{l=2}^{m-1} e^{-\boldsymbol{\kappa}_l^+ d_l/\mu_s}\Big)\int_{-z_m}^{-z_{m-1}} e^{\boldsymbol{\kappa}_m^+(z_{m-1}+z')/\mu_s}\mathcal{F}_m^+(\mu_s,\phi_s,z')\mathrm{d}z'\Big]\\
&+ \int_{-z_1}^{0} e^{\boldsymbol{\kappa}_1^+ z'/\mu_s}\mathcal{F}_1^+(\mu_s,\phi_s,z')\mathrm{d}z'\\
&= \Big(\prod_{m=1}^{L} e^{-\boldsymbol{\kappa}_l^+ d_l/\mu}\Big)\mathcal{R}(\mu_s)\mathbf{I}_L^-(-\mu,\phi_s,-z_L)\\
&+ \sum_{m=1}^{L}\Big[\Big(\prod_{m=1}^{m-1} e^{-\boldsymbol{\kappa}_l^+ d_l/\mu}\Big)\int_{-z_m}^{-z_{m-1}} e^{\boldsymbol{\kappa}_m^+(z_{m-1}+z')/\mu}\mathcal{F}_m^+(\mu,\phi_s,z')\mathrm{d}z'\Big]\\
&= \Big(\prod_{m=1}^{L} e^{-\boldsymbol{\kappa}_l^+ d_l/\mu_s}\Big)\mathcal{R}(\mu_s)\Big(\prod_{m=1}^{L} e^{-\boldsymbol{\kappa}_l^- d_l/\mu_s}\Big)\mathbf{I}_i(-\mu_i,\phi_i,0)\delta(\mu_s-\mu_i)\delta(\phi_s-\phi_i)\\
&+ \Big(\prod_{m=1}^{L} e^{-\boldsymbol{\kappa}_l^+ d_l/\mu_s}\Big)\mathcal{R}(\mu_s)\sum_{m=1}^{L}\Big[\Big(\prod_{l=m+1}^{L} e^{-\boldsymbol{\kappa}_l^- d_l/\mu_s}\Big)\\
&\quad \int_{-z_m}^{-z_{m-1}} e^{-\boldsymbol{\kappa}_m^-(z_m+z')/\mu_s}\mathcal{F}_m^-(-\mu_s,\phi_s,z')\mathrm{d}z'\Big]\\
&+ \sum_{m=1}^{L}\Big[\Big(\prod_{m=1}^{m-1} e^{-\boldsymbol{\kappa}_l^+ d_l/\mu_s}\Big)\int_{-z_m}^{-z_{m-1}} e^{\boldsymbol{\kappa}_m^+(z_{m-1}+z')/\mu_s}\mathcal{F}_m^+(\mu_s,\phi_s,z')\mathrm{d}z'\Big]
\end{aligned}
\tag{3.17}
$$

The first term in (3.17) accounts for the round trip extinction and ground reflection effects on the incident intensity; the second term is the sum of the reflected downward intensity that is scattered by all the layers, it also has been attenuated because of the extinction along the radiation path. The last term is the sum of all the attenuated upward scattered intensity by all the layers.

To solve these $2\times L$ RT equations, we use an iterative approach. The The iterative approach is chosen for two reasons: (1) It is easy to understand and be implemented for the lower order solutions; (2) The solution can be decomposed to several parts which have physical interpretations, therefore, the physical scattering mechanisms can be separated and readily analyzed. The drawback of the iterative approach is its high computation cost for higher order solutions.

zeroth-order solutions is obtained by setting all the source matrices to be zero. Then the zeroth-order source matrices can be obtained by taking the zeroth-order solution into the RT equation set, which in turn gives the first order solution. Higher order solutions can be obtained by the same approach.

First, source matrices in all canopy layers are set to be zero

$$\mathcal{F}_l^- = \mathcal{F}_l^+ = 0 \qquad 1 \le l \le L \tag{3.18}$$

and get the zeroth-order solutions

$$\mathbf{I}_1^{(0)-}(-\mu_s,\phi_s,z) = e^{\boldsymbol{\kappa}_1^- z/\mu_s}\mathbf{I}_i(-\mu_i,\phi_i,0)\delta(\mu_s-\mu_i)\delta(\phi_s-\phi_i) \tag{3.19}$$

$$\begin{aligned}\mathbf{I}_l^{(0)-}(-\mu_s,\phi_s,z) &= e^{\boldsymbol{\kappa}_l^-(z+z_{l-1})/\mu_s}\Big(\prod_{m=1}^{l-1} e^{-\boldsymbol{\kappa}_m^- d_m/\mu_s}\Big) \\ &\quad \mathbf{I}_i(-\mu_i,\phi_i,0)\delta(\mu_s-\mu_i)\delta(\phi_s-\phi_i) \quad 2\le l\le L-1\end{aligned} \tag{3.20}$$

$$\begin{aligned}\mathbf{I}_L^{(0)-}(-\mu,\phi,z) &= e^{\boldsymbol{\kappa}_L^-(z+z_{L-1})/\mu}\Big(\prod_{m=1}^{L-1} e^{-\boldsymbol{\kappa}_m^- d_m/\mu}\Big) \\ &\quad \mathbf{I}_i(-\mu_i,\phi_i,0)\delta(\mu_s-\mu_i)\delta(\phi_s-\phi_i)\end{aligned} \tag{3.21}$$

$$\begin{aligned}\mathbf{I}_L^{(0)+}(\mu_s,\phi_s,z) &= e^{-\boldsymbol{\kappa}_L^+(z+z_L)/\mu_s}\mathcal{R}(\mu_s)\Big(\prod_{m=1}^{L} e^{-\boldsymbol{\kappa}_m^- d_m/\mu_s}\Big) \\ &\quad \mathbf{I}_i(-\mu_i,\phi_i,0)\delta(\mu_s-\mu_i)\delta(\phi_s-\phi_i)\end{aligned} \tag{3.22}$$

$$\begin{aligned}\mathbf{I}_l^{(0)+}(\mu_s,\phi_s,z) &= e^{-\boldsymbol{\kappa}_l^+(z+z_l)/\mu_s}\Big(\prod_{m=l+1}^{L} e^{-\boldsymbol{\kappa}_m^+ d_m/\mu_s}\Big)\mathcal{R}(\mu_s)\Big(\prod_{m=1}^{L} e^{-\boldsymbol{\kappa}_m^- d_m/\mu_s}\Big) \\ &\quad \mathbf{I}_i(-\mu_i,\phi_i,0)\delta(\mu_s-\mu_i)\delta(\phi_s-\phi_i) \quad 2\le l\le L-1\end{aligned} \tag{3.23}$$

$$\begin{aligned}\mathbf{I}_1^{(0)+}(\mu_s,\phi_s,z) &= e^{-\boldsymbol{\kappa}_1^+(z+z_1)/\mu_s}\Big(\prod_{m=2}^{L} e^{-\boldsymbol{\kappa}_m^+ d_m/\mu_s}\Big)\mathcal{R}(\mu_s)\Big(\prod_{m=1}^{L} e^{-\boldsymbol{\kappa}_m^- d_m/\mu_s}\Big) \\ &\quad \mathbf{I}_i(-\mu_i,\phi_i,0)\delta(\mu_s-\mu_i)\delta(\phi_s-\phi_i)\end{aligned} \tag{3.24}$$

Then the zeroth-order source matrices can be obtained by taking the zeroth-order solutions into Equation (2.8), which integrates the scattered intensities from all the incidence directions (μ', ϕ'). In the top layer, we get the upward and downward zeroth-order source matrices

$$\begin{aligned}
\mathcal{F}_1^{(0)+}(\mu_s, \phi_s, z) &= \frac{1}{\mu_s}\Big[\int_0^{2\pi}\int_0^1 \mathcal{P}_1(\mu_s, \phi_s; \mu', \phi')\mathbf{I}_1^{(0)+}(\mu', \phi', z)\mathrm{d}\Omega' \\
&+ \int_0^{2\pi}\int_0^1 \mathcal{P}_1(\mu_s, \phi_s; -\mu', \phi')\mathbf{I}_1^{(0)-}(-\mu', \phi', z)\mathrm{d}\Omega'\Big] \\
&= \frac{1}{\mu_s}\Big[\mathcal{P}_1(\mu_s, \phi_s; \mu_i, \phi_i)e^{-\boldsymbol{\kappa}_1^+(z+z_1)/\mu_i}\Big(\prod_{m=2}^{L} e^{-\boldsymbol{\kappa}_m^+ d_m/\mu_i}\Big)\mathcal{R}(\mu_i)\Big(\prod_{m=1}^{L} e^{-\boldsymbol{\kappa}_m^- d_m/\mu_i}\Big) \\
&+ \mathcal{P}_1(\mu_s, \phi_s; -\mu_i, \phi_i)e^{\boldsymbol{\kappa}_1^- z/\mu_i}\Big]\mathbf{I}_i(-\mu_i, \phi_i, 0)
\end{aligned} \tag{3.25}$$

$$\begin{aligned}
\mathcal{F}_1^{(0)-}(-\mu_s, \phi_s, z) &= \frac{1}{\mu_s}\Big[\int_0^{2\pi}\int_0^1 \mathcal{P}_1(-\mu_s, \phi_s; \mu', \phi')\mathbf{I}_1^{(0)+}(\mu', \phi', z)\mathrm{d}\Omega' \\
&+ \int_0^{2\pi}\int_0^1 \mathcal{P}_1(-\mu_s, \phi_s; -\mu', \phi')\mathbf{I}_1^{(0)-}(-\mu', \phi', z)\mathrm{d}\Omega'\Big] \\
&= \frac{1}{\mu_s}\Big[\mathcal{P}_1(-\mu_s, \phi_s; \mu_i, \phi_i)e^{-\boldsymbol{\kappa}_1^+(z+z_1)/\mu_i}\Big(\prod_{m=2}^{L} e^{-\boldsymbol{\kappa}_m^+ d_m/\mu_i}\Big)\mathcal{R}(\mu_i)\Big(\prod_{m=1}^{L} e^{-\boldsymbol{\kappa}_m^- d_m/\mu_i}\Big) \\
&+ \mathcal{P}_1(-\mu_s, \phi_s; -\mu_i, \phi_i)e^{\boldsymbol{\kappa}_1^- z/\mu_i}\Big]\mathbf{I}_i(-\mu_i, \phi_i, 0)
\end{aligned} \tag{3.26}$$

The scattering contributions from both the upward and downward intensities are included in the above source matrices. Similarly, the zeroth-order source matrices in Layer l $(2 \le l \le L-1)$ are

$$\begin{aligned}
\mathcal{F}_l^{(0)+}(\mu_s, \phi_s, z) &= \frac{1}{\mu_s}\Big[\int_0^{2\pi}\int_0^1 \mathcal{P}_l(\mu_s, \phi_s; \mu', \phi')\mathbf{I}_l^{(0)+}(\mu', \phi', z)\mathrm{d}\Omega' \\
&+ \int_0^{2\pi}\int_0^1 \mathcal{P}_l(\mu_s, \phi_s; -\mu', \phi')\mathbf{I}_l^{(0)-}(-\mu', \phi', z)\mathrm{d}\Omega'\Big] \\
&= \frac{1}{\mu_s}\Big[\mathcal{P}_l(\mu_s, \phi_s; \mu_i, \phi_i)e^{-\boldsymbol{\kappa}_l^+(z+z_l)/\mu_i}\Big(\prod_{m=l+1}^{L} e^{-\boldsymbol{\kappa}_m^+ d_m/\mu_i}\Big)\mathcal{R}(\mu_i)\Big(\prod_{m=1}^{L} e^{-\boldsymbol{\kappa}_m^- d_m/\mu_i}\Big) \\
&+ \mathcal{P}_l(\mu_s, \phi_s; -\mu_i, \phi_i)e^{\boldsymbol{\kappa}_l^-(z+z_{l-1})/\mu_i}\Big(\prod_{m=1}^{l-1} e^{-\boldsymbol{\kappa}_m^- d_m/\mu_i}\Big)\Big]\mathbf{I}_i(-\mu_i, \phi_i, 0)
\end{aligned} \tag{3.27}$$

$$\mathcal{F}_l^{(0)-}(-\mu_s,\phi_s,z) = \frac{1}{\mu_s}\Big[\int_0^{2\pi}\int_0^1 \mathcal{P}_l(-\mu_s,\phi_s;\mu',\phi')\mathbf{I}_l^{(0)+}(\mu',\phi',z)\mathrm{d}\Omega'$$
$$+\int_0^{2\pi}\int_0^1 \mathcal{P}_l(-\mu_s,\phi_s;-\mu',\phi')\mathbf{I}_l^{(0)-}(-\mu',\phi',z)\mathrm{d}\Omega'\Big]$$
$$= \frac{1}{\mu_s}\Big[\mathcal{P}_l(-\mu_s,\phi_s;\mu_i,\phi_i)e^{-\boldsymbol{\kappa}_l^+(z+z_l)/\mu_i}\Big(\prod_{m=l+1}^{L} e^{-\boldsymbol{\kappa}_m^+ d_m/\mu_i}\Big)\mathcal{R}(\mu_i)\Big(\prod_{m=1}^{L} e^{-\boldsymbol{\kappa}_m^- d_m/\mu_i}\Big)$$
$$+\mathcal{P}_l(-\mu_s,\phi_s;-\mu_i,\phi_i)e^{\boldsymbol{\kappa}_l^-(z+z_{l-1})/\mu_i}\Big(\prod_{m=1}^{l-1} e^{-\boldsymbol{\kappa}_m^- d_m/\mu_i}\Big)\Big]\mathbf{I}_i(-\mu_i,\phi_i,0) \qquad (3.28)$$

Similarly, in the bottom canopy layer

$$\mathcal{F}_L^{(0)+}(\mu_s,\phi_s,z) = \frac{1}{\mu_s}\Big[\int_0^{2\pi}\int_0^1 \mathcal{P}_L(\mu_s,\phi_s;\mu',\phi')\mathbf{I}_L^{(0)+}(\mu',\phi',z)\mathrm{d}\Omega'$$
$$+\int_0^{2\pi}\int_0^1 \mathcal{P}_L(\mu_s,\phi_s;-\mu',\phi')\mathbf{I}_L^{(0)-}(-\mu',\phi',z)\mathrm{d}\Omega'\Big]$$
$$= \frac{1}{\mu_s}\Big[\mathcal{P}_L(\mu_s,\phi_s;\mu_i,\phi_i)e^{-\boldsymbol{\kappa}_L^+(z+z_L)/\mu_i}\mathcal{R}(\mu_i)\Big(\prod_{m=1}^{L} e^{-\boldsymbol{\kappa}_m^- d_m/\mu_i}\Big)$$
$$+\mathcal{P}_L(\mu_s,\phi_s;-\mu_i,\phi_i)e^{\boldsymbol{\kappa}_L^-(z+z_{L-1})/\mu_i}\Big(\prod_{m=1}^{L-1} e^{-\boldsymbol{\kappa}_m^- d_m/\mu_i}\Big)\Big]\mathbf{I}_i(-\mu_i,\phi_i,0) \qquad (3.29)$$

$$\mathcal{F}_L^{(0)-}(-\mu_s,\phi_s,z) = \frac{1}{\mu_s}\Big[\int_0^{2\pi}\int_0^1 \mathcal{P}_L(-\mu_s,\phi_s;\mu',\phi')\mathbf{I}_L^{(0)+}(\mu',\phi',z)\mathrm{d}\Omega'$$
$$+\int_0^{2\pi}\int_0^1 \mathcal{P}_L(-\mu_s,\phi_s;-\mu',\phi')\mathbf{I}_L^{(0)-}(-\mu',\phi',z)\mathrm{d}\Omega'\Big]$$
$$= \frac{1}{\mu_s}\Big[\mathcal{P}_L(-\mu_s,\phi_s;\mu_i,\phi_i)e^{-\boldsymbol{\kappa}_L^+(z+z_L)/\mu_i}\mathcal{R}(\mu_i)\Big(\prod_{m=1}^{L} e^{-\boldsymbol{\kappa}_m^- d_m/\mu_i}\Big)$$
$$+\mathcal{P}_L(-\mu_s,\phi_s;-\mu_i,\phi_i)e^{\boldsymbol{\kappa}_L^-(z+z_{L-1})/\mu_i}\Big(\prod_{m=1}^{L-1} e^{-\boldsymbol{\kappa}_m^- d_m/\mu_i}\Big)\Big]\mathbf{I}_i(-\mu_i,\phi_i,0) \qquad (3.30)$$

By submitting the source matrices in the $2L$ equations (3.6) to (3.17) with the above zeroth-order results, the first order Mi-MIMICS solution for downward intensity in the top layer is given by

$$
\begin{aligned}
\mathbf{I}_1^-(-\mu_s,\phi_s,z) = \Big\{ & e^{\boldsymbol{\kappa}_1^- z/\mu_s}\delta(\mu_s-\mu_i)\delta(\phi_s-\phi_i) \\
& + \frac{1}{\mu_s}\Big[\int_z^0 e^{\boldsymbol{\kappa}_1^-(z-z')/\mu_s}\mathcal{P}_1(-\mu_s,\phi_s;\mu_i,\phi_i)e^{-\boldsymbol{\kappa}_1^+(z'+z_1)/\mu_i}\mathrm{d}z'\Big] \\
& \cdot\Big(\prod_{m=2}^{L} e^{-\boldsymbol{\kappa}_m^+ d_m/\mu_i}\Big)\mathcal{R}(\mu_i)\Big(\prod_{m=1}^{L} e^{-\boldsymbol{\kappa}_m^- d_m/\mu_i}\Big) \\
& + \frac{1}{\mu_s}\Big[\int_z^0 e^{\boldsymbol{\kappa}_1^-(z-z')/\mu_s}\mathcal{P}_1(-\mu_s,\phi_s;-\mu_i,\phi_i)e^{\boldsymbol{\kappa}_1^- z'/\mu_i}\mathrm{d}z'\Big]\Big\}\mathbf{I}_i(-\mu_i,\phi_i,0)
\end{aligned}
\tag{3.31}
$$

and for the bottom layer, the downward intensity is

$$
\begin{aligned}
\mathbf{I}_L^-(-\mu_s,\phi_s,z) = \Big\{ & e^{\boldsymbol{\kappa}_L^-(z+z_{L-1})/\mu_s}\Big(\prod_{m=1}^{L-1} e^{-\boldsymbol{\kappa}_m^- d_m/\mu_s}\Big)\delta(\mu_s-\mu_i)\delta(\phi_s-\phi_i) \\
& + e^{\boldsymbol{\kappa}_L^-(z+z_{L-1})/\mu_s}\sum_{m=1}^{L-1}\Big\{\Big(\prod_{l=m+1}^{L-1} e^{-\boldsymbol{\kappa}_l^- d_l/\mu_s}\Big)\Big[\\
& \frac{1}{\mu_s}\Big[\int_{-z_m}^{-z_{m-1}} e^{-\boldsymbol{\kappa}_m^-(z_m+z')/\mu_s}\mathcal{P}_m(-\mu_s,\phi_s;\mu_i,\phi_i)e^{-\boldsymbol{\kappa}_l^+(z'+z_{m-1})/\mu_i}\mathrm{d}z'\Big] \\
& \Big(\prod_{l=m+1}^{L} e^{-\boldsymbol{\kappa}_l^+ d_l/\mu_i}\Big)\mathcal{R}(\mu_i)\Big(\prod_{l=1}^{L} e^{-\boldsymbol{\kappa}_l^- d_l/\mu_i}\Big) \\
& + \frac{1}{\mu_s}\Big[\int_{-z_m}^{-z_{m-1}} e^{-\boldsymbol{\kappa}_m^-(z_m+z')/\mu_s}\mathcal{P}_m(-\mu_s,\phi_s;-\mu_i,\phi_i)e^{\boldsymbol{\kappa}_m^-(z'+z_{m-1})/\mu_i}\mathrm{d}z'\Big] \\
& \Big(\prod_{l=1}^{m-1} e^{-\boldsymbol{\kappa}_l^- d_l/\mu_i}\Big)\Big]\Big\} \\
& + \frac{1}{\mu_s}\Big[\int_z^{-z_{L-1}} e^{\boldsymbol{\kappa}_L^-(z-z')/\mu_s}\mathcal{P}_L(-\mu_s,\phi_s;\mu_i,\phi_i)e^{-\boldsymbol{\kappa}_L^+(z'+z_L)/\mu_i}\mathrm{d}z'\Big] \\
& \cdot\mathcal{R}(\mu_i)\Big(\prod_{m=1}^{L} e^{-\boldsymbol{\kappa}_m^- d_m/\mu_i}\Big) \\
& + \frac{1}{\mu_s}\Big[\int_z^{-z_{L-1}} e^{\boldsymbol{\kappa}_L^-(z-z')/\mu_s}\mathcal{P}_L(-\mu_s,\phi_s;-\mu_i,\phi_i)e^{\boldsymbol{\kappa}_L^-(z'+z_{L-1})/\mu_i}\mathrm{d}z'\Big] \\
& \cdot\Big(\prod_{m=1}^{L-1} e^{-\boldsymbol{\kappa}_m^- d_m/\mu_i}\Big)\Big\}\mathbf{I}_i(-\mu_i,\phi_i,0)
\end{aligned}
\tag{3.32}
$$

Therefore, the downward intensity at the ground surface $z = -z_L$ is

$$
\begin{aligned}
\mathbf{I}_L^-(-\mu_s, \phi_s, -z_L) = & \Bigg\{ \Big(\prod_{m=1}^{L} e^{-\boldsymbol{\kappa}_m^- d_m/\mu_s} \Big) \delta(\mu_s - \mu_i)\delta(\phi_s - \phi_i) \\
& + \sum_{m=1}^{L} \Bigg\{ \Big(\prod_{l=m-1}^{L} e^{-\boldsymbol{\kappa}_l^- d_l/\mu_s} \Big) \Bigg[\\
& \frac{1}{\mu_s} \Big[\int_{-z_m}^{-z_{m-1}} e^{-\boldsymbol{\kappa}_m^-(z_m+z')/\mu_s} \mathcal{P}_m(-\mu_s, \phi_s; \mu_i, \phi_i) e^{-\boldsymbol{\kappa}_m^+(z'+z_m)/\mu_i} \mathrm{d}z' \Big] \\
& \Big(\prod_{l=m-1}^{L} e^{-\boldsymbol{\kappa}_l^+ d_l/\mu_i} \Big) \mathcal{R}(\mu_i) \Big(\prod_{l=1}^{L} e^{-\boldsymbol{\kappa}_l^- d_l/\mu_i} \Big) \\
& + \frac{1}{\mu_s} \Big[\int_{-z_m}^{-z_{m-1}} e^{-\boldsymbol{\kappa}_m^-(z_m+z')/\mu_s} \mathcal{P}_m(-\mu_s, \phi_s; -\mu_i, \phi_i) e^{\boldsymbol{\kappa}_m^-(z'+z_{m-1})/\mu_i} \mathrm{d}z' \Big] \\
& \Big(\prod_{l=1}^{m-1} e^{-\boldsymbol{\kappa}_l^- d_l/\mu_i} \Big) \Bigg] \Bigg\} \Bigg\} \mathbf{I}_i(-\mu_i, \phi_i, 0)
\end{aligned}
\tag{3.33}
$$

The $L - th$ layer's upward intensity after the ground reflection is then

$$
\begin{aligned}
\mathbf{I}_L^+(\mu_s, \phi_s, z) = & e^{-\boldsymbol{\kappa}_L^+(z+z_L)/\mu_s} \mathcal{R}(\mu_s) \mathbf{I}_L^-(-\mu_s, \phi_s, -z_L) \\
& + \Bigg\{ \frac{1}{\mu_s} \Big[\int_{-z_L}^{z} e^{-\boldsymbol{\kappa}_L^+(z-z')/\mu_s} \mathcal{P}_L(\mu_s, \phi_s; \mu_i, \phi_i) e^{-\boldsymbol{\kappa}_L^+(z'+z_L)/\mu_i} \mathrm{d}z' \Big] \\
& \cdot \mathcal{R}(\mu_i) \Big(\prod_{m=1}^{L} e^{-\boldsymbol{\kappa}_m^- d_m/\mu_i} \Big) \\
& + \frac{1}{\mu_s} \Big[\int_{-z_L}^{z} e^{-\boldsymbol{\kappa}_L^+(z-z')/\mu_s} \mathcal{P}_L(\mu_s, \phi_s; -\mu_i, \phi_i) e^{\boldsymbol{\kappa}_L^-(z'+z_{L-1})/\mu_i} \mathrm{d}z' \Big] \\
& \cdot \Big(\prod_{m=1}^{L-1} e^{-\boldsymbol{\kappa}_m^- d_m/\mu_i} \Big) \Bigg\} \mathbf{I}_i(-\mu_i, \phi_i, 0)
\end{aligned}
\tag{3.34}
$$

Then in the top layer, the upward intensity is given by

$$\begin{aligned}
\mathbf{I}_1^+(\mu_s,\phi_s,z) &= e^{-\boldsymbol{\kappa}_1^+(z+z_1)/\mu_s}\Big(\prod_{m=2}^{L} e^{-\boldsymbol{\kappa}_m^+ d_m/\mu_s}\Big)\mathcal{R}(\mu_s)\mathbf{I}_L^-(-\mu_s,\phi_s,-z_L)\\
&+\Bigg\{e^{-\boldsymbol{\kappa}_1^+(z+z_1)/\mu_s}\sum_{m=2}^{L}\Bigg\{\Big(\prod_{l=2}^{m-1} e^{-\boldsymbol{\kappa}_l^+ d_l/\mu_s}\Big)\Bigg[\\
&\frac{1}{\mu_s}\Big[\int_{-z_m}^{-z_{m-1}} e^{\boldsymbol{\kappa}_m^+(z_{m-1}+z')/\mu_s}\mathcal{P}_m(\mu_s,\phi_s;\mu_i,\phi_i)e^{-\boldsymbol{\kappa}_m^+(z'+z_m)/\mu_i}\mathrm{d}z'\Big]\\
&\Big(\prod_{l=m+1}^{L} e^{-\boldsymbol{\kappa}_l^+ d_l/\mu_i}\Big)\mathcal{R}(\mu_i)\Big(\prod_{l=1}^{L} e^{-\boldsymbol{\kappa}_l^- d_l/\mu_i}\Big)\\
&+\frac{1}{\mu_s}\Big[\int_{-z_m}^{-z_{m-1}} e^{\boldsymbol{\kappa}_m^+(z_{m-1}+z')/\mu_s}\mathcal{P}_m(\mu_s,\phi_s;-\mu_i,\phi_i)e^{\boldsymbol{\kappa}_m^-(z'+z_{m-1})/\mu_i}\mathrm{d}z'\Big]\\
&\Big(\prod_{l=1}^{m-1} e^{-\boldsymbol{\kappa}_l^- d_l/\mu_i}\Big)\Bigg]\Bigg\}\\
&+\frac{1}{\mu_s}\Big[\int_{-z_1}^{z} e^{-\boldsymbol{\kappa}_1^+(z-z')/\mu_s}\mathcal{P}_1(\mu_s,\phi_s;\mu_i,\phi_i)e^{-\boldsymbol{\kappa}_1^+(z'+z_1)/\mu_i}\mathrm{d}z'\Big]\\
&\Big(\prod_{m=2}^{L} e^{-\boldsymbol{\kappa}_m^+ d_m/\mu_i}\Big)\mathcal{R}(\mu_i)\Big(\prod_{m=1}^{L} e^{-\boldsymbol{\kappa}_m^- d_m/\mu_i}\Big)\\
&+\frac{1}{\mu_s}\Big[\int_{-z_1}^{z} e^{-\boldsymbol{\kappa}_1^+(z-z')/\mu_s}\mathcal{P}_1(\mu_s,\phi_s;-\mu_i,\phi_i)e^{\boldsymbol{\kappa}_1^- z'/\mu_i}\mathrm{d}z'\Big]\\
&\Bigg\}\cdot\mathbf{I}_i(-\mu_i,\phi_i,0)
\end{aligned}\tag{3.35}$$

Set $z=0$, the upward intensity at the top canopy surface is solved

$$\begin{aligned}
\mathbf{I}_1^+(\mu_s,\phi_s,0) &= \Big(\prod_{m=1}^{L} e^{-\boldsymbol{\kappa}_m^+ d_m/\mu_s}\Big)\mathcal{R}(\mu_s)\mathbf{I}_L^-(-\mu_s,\phi_s,-z_L)\\
&+\Bigg\{\sum_{m=1}^{L}\Bigg\{\Big(\prod_{l=1}^{m-1} e^{-\boldsymbol{\kappa}_l^+ d_l/\mu_s}\Big)\Bigg[\\
&\frac{1}{\mu_s}\Big[\int_{-z_m}^{-z_{m-1}} e^{\boldsymbol{\kappa}_m^+(z_{m-1}+z')/\mu_s}\mathcal{P}_m(\mu_s,\phi_s;\mu_i,\phi_i)e^{-\boldsymbol{\kappa}_m^+(z'+z_m)/\mu_i}\mathrm{d}z'\Big]\\
&\Big(\prod_{l=m+1}^{L} e^{-\boldsymbol{\kappa}_l^+ d_l/\mu_i}\Big)\mathcal{R}(\mu_i)\Big(\prod_{l=1}^{L} e^{-\boldsymbol{\kappa}_l^- d_l/\mu_i}\Big)\\
&+\frac{1}{\mu_s}\Big[\int_{-z_m}^{-z_{m-1}} e^{\boldsymbol{\kappa}_m^+(z_{m-1}+z')/\mu_s}\mathcal{P}_m(\mu_s,\phi_s;-\mu_i,\phi_i)e^{\boldsymbol{\kappa}_m^-(z'+z_{m-1})/\mu_i}\mathrm{d}z'\Big]\\
&\Big(\prod_{l=1}^{m-1} e^{-\boldsymbol{\kappa}_l^- d_l/\mu_i}\Big)\Bigg]\Bigg\}\Bigg\}\cdot\mathbf{I}_i(-\mu_i,\phi_i,0)
\end{aligned}\tag{3.36}$$

A transform matrix $\mathcal{T}_{canopy}(\mu_s, \phi_s; -\mu_i, \phi_i)$ is defined as

$$\mathcal{T}_{canopy}(\mu_s, \phi_s; -\mu_i, \phi_i) = \frac{\mathbf{I}_s(\mu_s, \phi_s, 0)}{\mathbf{I}_i(-\mu_i, \phi_i, 0)} = \frac{\mathbf{I}_1^+(\mu_s, \phi_s, 0)}{\mathbf{I}_i(-\mu_i, \phi_i, 0)} \tag{3.37}$$

From Equations (3.33), (3.36) and (3.37), the total canopy bistatic scattering transformation matrix $\mathcal{T}_{canopy}(\mu_s, \phi_s; -\mu_i, \phi_i)$ can be organized as

$$\begin{aligned}
&\mathcal{T}_{canopy}(\mu_s, \phi_s; -\mu_i, \phi_i) = \\
&\quad \Big(\prod_{m=1}^{L} e^{-\boldsymbol{\kappa}_l^+ d_l/\mu_s}\Big)\mathcal{R}(\mu_s)\Big(\prod_{m=1}^{L} e^{-\boldsymbol{\kappa}_l^- d_l/\mu_s}\Big)\delta(\mu_s - \mu_i)\delta(\phi_s - \phi_i) \\
&+ \sum_{m=1}^{L}\Bigg\{\Big(\prod_{l=1}^{L} e^{-\boldsymbol{\kappa}_l^+ d_l/\mu_s}\Big)\mathcal{R}(\mu_s)\Big(\prod_{l=m+1}^{L} e^{-\boldsymbol{\kappa}_l^- d_l/\mu_s}\Big)\Bigg[\\
&\quad \frac{1}{\mu_s}\Big[\int_{-z_m}^{-z_{m-1}} e^{-\boldsymbol{\kappa}_m^-(z_m+z')/\mu_s}\mathcal{P}_m(-\mu_s, \phi_s; \mu_i, \phi_i)e^{-\boldsymbol{\kappa}_m^+(z'+z_m)/\mu_i}\mathrm{d}z'\Big] \\
&\quad \Big(\prod_{l=m+1}^{L} e^{-\boldsymbol{\kappa}_l^+ d_l/\mu_i}\Big)\mathcal{R}(\mu_i)\Big(\prod_{l=1}^{L} e^{-\boldsymbol{\kappa}_l^- d_l/\mu_i}\Big) \\
&+ \frac{1}{\mu_s}\Big[\int_{-z_m}^{-z_{m-1}} e^{-\boldsymbol{\kappa}_m^-(z_m+z')/\mu_s}\mathcal{P}_m(-\mu_s, \phi_s; -\mu_i, \phi_i)e^{\boldsymbol{\kappa}_m^-(z'+z_{m-1})/\mu_i}\mathrm{d}z'\Big] \\
&\quad \Big(\prod_{l=1}^{m-1} e^{-\boldsymbol{\kappa}_l^- d_l/\mu_i}\Big)\Bigg]\Bigg\} \\
&+ \sum_{m=1}^{L}\Bigg\{\Big(\prod_{l=1}^{m-1} e^{-\boldsymbol{\kappa}_l^+ d_l/\mu_s}\Big)\Bigg[\\
&\quad \frac{1}{\mu_s}\Big[\int_{-z_m}^{-z_{m-1}} e^{\boldsymbol{\kappa}_m^+(z_{m-1}+z')/\mu_s}\mathcal{P}_m(\mu_s, \phi_s; \mu_i, \phi_i)e^{-\boldsymbol{\kappa}_m^+(z'+z_m)/\mu_i}\mathrm{d}z'\Big] \\
&\quad \Big(\prod_{l=m+1}^{L} e^{-\boldsymbol{\kappa}_l^+ d_l/\mu_i}\Big)\mathcal{R}(\mu_i)\Big(\prod_{m=1}^{L} e^{-\boldsymbol{\kappa}_l^- d_l/\mu_i}\Big) \\
&+ \frac{1}{\mu_s}\Big[\int_{-z_m}^{-z_{m-1}} e^{\boldsymbol{\kappa}_m^+(z_{m-1}+z')/\mu_s}\mathcal{P}_m(\mu_s, \phi_s; -\mu_i, \phi_i)e^{\boldsymbol{\kappa}_m^-(z'+z_{m-1})/\mu_i}\mathrm{d}z'\Big] \\
&\quad \Big(\prod_{l=1}^{m-1} e^{-\boldsymbol{\kappa}_l^- d_l/\mu_i}\Big)\Bigg]\Bigg\}
\end{aligned} \tag{3.38}$$

The above solution is rearranged in the form of Equation (3.39). It shows that in addition to the specular refection part by the ground surface, every layer contributes to the total canopy scattered intensity in four ways:

$$
\begin{aligned}
&\mathcal{T}_{canopy}(\mu_s, \phi_s; -\mu_i, \phi_i) = \\
&\quad \Big(\prod_{m=1}^{L} e^{-\boldsymbol{\kappa}_m^{+} d_m/\mu_s}\Big)\mathcal{R}(\mu_s)\Big(\prod_{m=1}^{L} e^{-\boldsymbol{\kappa}_m^{-} d_m/\mu_s}\Big)\delta(\mu_s - \mu_i)\delta(\phi_s - \phi_i) \\
&+ \sum_{m=1}^{L}\Big[\mathcal{T}_{gmg}(\mu_s, \phi_s; -\mu_i, \phi_i) + \mathcal{T}_{mg}(\mu_s, \phi_s; -\mu_i, \phi_i) \\
&+ \mathcal{T}_{gm}(\mu_s, \phi_s; -\mu_i, \phi_i) + \mathcal{T}_{mdir}(\mu_s, \phi_s; -\mu_i, \phi_i)\Big]
\end{aligned} \tag{3.39}
$$

where $\mathcal{T}_{gmg}$ is the contribution of Ground reflection — Canopy scattering — Ground reflection mechanism by the $m-th$ layer.

$$
\begin{aligned}
\mathcal{T}_{gmg}(\mu_s, \phi_s; -\mu_i, \phi_i) \;=\; & \frac{1}{\mu_s}\Big(\prod_{l=1}^{L} e^{-\boldsymbol{\kappa}_l^{+} d_l/\mu_s}\Big)\mathcal{R}(\mu_s)\Big(\prod_{l=m+1}^{L} e^{-\boldsymbol{\kappa}_l^{-} d_l/\mu_s}\Big) \\
\mathcal{A}_{gmg}(\mu_s, \phi_s; \mu_i, \phi_i)&\Big(\prod_{l=m+1}^{L} e^{-\boldsymbol{\kappa}_l^{+} d_l/\mu_i}\Big)\mathcal{R}(\mu_i)\Big(\prod_{l=1}^{L} e^{-\boldsymbol{\kappa}_l^{-} d_l/\mu_i}\Big)
\end{aligned} \tag{3.40}
$$

The factors in the above product explain the scattering mechanism in the order of from right to left

① $\prod_{l=1}^{L} e^{-\boldsymbol{\kappa}_l^{-} d_l/\mu_i}$: Product of transmissivity values from the top to the bottom layers. The downward intensity is attenuated by this amount in the incident direction $(-\mu_i, \phi_i)$ as it passes through all the L canopy layers. For vector expressions, the indexes of transmissivity matrices follow the order $L, L-1, \cdots, 2, 1$.

② $\mathcal{R}(\mu_i)$: Reflectivity matrix at the angle of θ_i since the wave intensity remains in the original incident direction when it reaches the gourd surface.

③ $\prod_{l=m+1}^{L} e^{-\boldsymbol{\kappa}_l^{+} d_l/\mu_i}$: Product of transmissivity values from all the layers underneath Layer m. The reflected intensity is attenuated by this amount in (μ_i, ϕ_i) direction as it passes through all those layers. For vector expressions, the indexes of transmissivity matrices follow the order $m+1, m+2, \cdots, L$.

④ $\mathcal{A}_{gmg}(\mu_s, \phi_s; \mu_i, \phi_i)$: The upward intensity reflected by the ground reaches and is scattered by the $m-th$ layer into $(-\mu_s, \phi_s)$ direction and becomes downward again.

⑤ $\prod_{l=m+1}^{L} e^{-\boldsymbol{\kappa}_l^- d_l/\mu_s}$: Product of transmissivity values from all the layers underneath Layer m. The reflected intensity is attenuated by this amount in $(-\mu_s, \phi_s)$ direction as it passes through all those layers. For vector expressions, the indexes of transmissivity matrices follow the order $L, L-1, \cdots, m+2, m+1$.

⑥ $\mathcal{R}(\mu_s)$: Reflectivity matrix at the angle of θ_s since the wave intensity is in the direction of $(-\mu_s, \phi_s)$ when it reaches the gourd surface.

⑦ $\prod_{l=1}^{L} e^{-\boldsymbol{\kappa}_l^+ d_l/\mu_s}$: Product of transmissivity values from the top to the bottom layers. The upward intensity is attenuated by this amount in the scattering direction (μ_s, ϕ_s) as it passes through all the L canopy layers. For vector expressions, the indexes of transmissivity matrices follow the order $1, 2, \cdots, L-1, L$.

$\mathcal{T}_{mg}$ accounts for Canopy scattering — Ground reflection contribution by the $m-th$ layer

$$\begin{aligned} \mathcal{T}_{mg}(\mu_s, \phi_s; -\mu_i, \phi_i) &= \frac{1}{\mu_s}\Big(\prod_{l=1}^{L} e^{-\boldsymbol{\kappa}_l^+ d_l/\mu_s}\Big)\mathcal{R}(\mu_s)\Big(\prod_{l=m+1}^{L} e^{-\boldsymbol{\kappa}_l^- d_l/\mu_s}\Big) \\ & \mathcal{A}_{mg}(\mu_s, \phi_s; \mu_i, \phi_i)\Big(\prod_{l=1}^{m-1} e^{-\boldsymbol{\kappa}_l^- d_l/\mu_i}\Big) \end{aligned} \tag{3.41}$$

The factors in the above product explain the scattering mechanism in the order of from right to left as follow

① $\prod_{l=1}^{m-1} e^{-\boldsymbol{\kappa}_l^- d_l/\mu_i}$: Product of transmissivity values from the top to the $(m-1)-th$layer. The downward intensity is attenuated by this amount in the incident direction $(-\mu_i, \phi_i)$ as it passes through all the L canopy layers. For vector expressions, the indexes of transmissivity matrices follow the order $m-1, m-2, \cdots, 2, 1$.

② $\mathcal{A}_{mg}(\mu_s, \phi_s; \mu_i, \phi_i)$: The incident intensity reflected by the ground reaches and is scattered by the $m-th$ layer into $(-\mu_s, \phi_s)$ direction and still propagates downward.

③ $\prod_{l=m+1}^{L} e^{-\boldsymbol{\kappa}_l^- d_l/\mu_s}$: Product of transmissivity values from all the layers underneath Layer m. The scattered downward intensity is attenuated by this amount in $(-\mu_s, \phi_s)$ direction as it passes through all those layers. For vector expressions, the indexes of transmissivity matrices follow the order $L, L-1, \cdots, m+2, m+1$.

④ $\mathcal{R}(\mu_s)$: Reflectivity matrix at the angle of θ_s since the wave intensity is in the direction of $(-\mu_s, \phi_s)$ when it reaches the gourd surface.

⑤ $\prod_{l=1}^{L} e^{-\boldsymbol{\kappa}_l^+ d_l/\mu_s}$: Product of transmissivity values from the top to the bottom layers. The upward intensity is attenuated by this amount in the scattering direction (μ_s, ϕ_s) as it passes through all the L canopy layers. For vector expressions, the indexes of transmissivity matrices follow the order $1, 2, \cdots L-1, L$.

$\mathcal{T}_{gm}$ is the complement of $\mathcal{T}_{mg}$, it shows how the incident intensity is first reflected by the ground and then scattered into the direction (μ_s, ϕ) by the $m-th$ layer

$$\begin{aligned}\mathcal{T}_{gm}(\mu_s, \phi_s; -\mu_i, \phi_i) \quad = \quad & \frac{1}{\mu_s}\Big(\prod_{l=1}^{m-1} e^{-\boldsymbol{\kappa}_l^+ d_l/\mu_s}\Big)\mathcal{A}_{gm}(\mu_s, \phi_s; \mu_i, \phi_i) \\ & \Big(\prod_{l=m+1}^{L} e^{-\boldsymbol{\kappa}_l^+ d_l/\mu_i}\Big)\mathcal{R}(\mu_i)\Big(\prod_{l=1}^{L} e^{-\boldsymbol{\kappa}_l^- d_l/\mu_i}\Big) \qquad (3.42)\end{aligned}$$

Similarly, this scattering mechanism can be explained by terms of the factors in th product

① $\prod_{l=1}^{L} e^{-\boldsymbol{\kappa}_l^- d_l/\mu_i}$: Product of transmissivity values from the top to the bottom layers. The downward intensity is attenuated by this amount in the incident direction $(-\mu_i, \phi_i)$ as it passes through all the L canopy layers. For vector expressions, the indexes of transmissivity matrices follow the order $L, L-1, \cdots, 2, 1$.

② $\mathcal{R}(\mu_i)$: Reflectivity matrix at the angle of θ_i since the wave intensity remains in the original incident direction when it reaches the gourd surface.

③ $\prod_{l=m+1}^{L} e^{-\boldsymbol{\kappa}_l^+ d_l/\mu_i}$: Product of transmissivity values from all the layers underneath Layer m. The reflected intensity is attenuated by this amount in (μ_i, ϕ_i) direction as it passes through all those layers. For vector expressions, the indexes of transmissivity matrices follow the order $m+1, m+2, \cdots, L$.

④ $\mathcal{A}_{gm}(\mu_s, \phi_s; \mu_i, \phi_i)$: The upward intensity reflected by the ground reaches and is scattered by the $m-th$ layer into (μ_s, ϕ_s) direction and still propagates upward.

⑤ $\prod_{l=1}^{m-1} e^{-\boldsymbol{\kappa}_l^+ d_l/\mu_s}$): Product of transmissivity values from layers above the $m-th$ layer. The upward intensity is attenuated by this amount in the scattering direction (μ_s, ϕ_s) as it passes through all the L canopy layers. For vector expressions, the indexes of transmissivity matrices follow the order $1, 2, \cdots, m-2, m-1$.

$\mathcal{T}_{mdir}$ stands for the direct scattering by the $m-th$ layer

$$\mathcal{T}_{mdir}(\mu_s, \phi_s; -\mu_i, \phi_i) = \frac{1}{\mu_s}\Big(\prod_{l=1}^{m-1} e^{-\boldsymbol{\kappa}_l^+ d_l/\mu_s}\Big)\mathcal{A}_{mdir}(\mu_s, \phi_s; \mu_i, \phi_i)\Big(\prod_{l=1}^{m-1} e^{-\boldsymbol{\kappa}_l^- d_l/\mu_i}\Big) \tag{3.43}$$

where the product can be decomposed into

① $\prod_{l=1}^{m-1} e^{-\boldsymbol{\kappa}_l^- d_l/\mu_i}$: Product of transmissivity values from the top to the $(m-1)-th$layer. The downward intensity is attenuated by this amount in the incident direction $(-\mu_i, \phi_i)$ as it passes through all the L canopy layers. For vector expressions, the indexes of transmissivity matrices follow the order $m-1, m-2, \cdots, 2, 1$.

② $\mathcal{A}_{mdir}(\mu_s, \phi_s; \mu_i, \phi_i)$: The downward incident intensity reaches and is scattered by the $m-th$ layer into (μ_s, ϕ_s) direction and becomes upward.

③ $\prod_{l=1}^{m-1} e^{-\boldsymbol{\kappa}_l^+ d_l/\mu_s}$): Product of transmissivity values from layers above the $m-th$ layer. The upward intensity is attenuated by this amount in the scattering direction (μ_s, ϕ_s) as it passes through all the L canopy layers. For vector expressions, the indexes of transmissivity matrices follow the order $1, 2, \cdots, m-2, m-1$.

In Equations (3.40) — (3.43),

$$\mathcal{A}_{gmg}(\mu_s, \phi_s; \mu_i, \phi_i) = \int_{-z_m}^{-z_{m-1}} e^{-\boldsymbol{\kappa}_m^-(z_m+z')/\mu_s} \mathcal{P}_m(-\mu_s, \phi_s; \mu_i, \phi_i) e^{-\boldsymbol{\kappa}_m^+(z'+z_m)/\mu_i} \mathrm{d}z' \tag{3.44}$$

$$\mathcal{A}_{mg}(\mu_s, \phi_s; \mu_i, \phi_i) = \int_{-z_m}^{-z_{m-1}} e^{-\boldsymbol{\kappa}_m^-(z_m+z')/\mu_s} \mathcal{P}_m(-\mu_s, \phi_s; -\mu_i, \phi_i) e^{\boldsymbol{\kappa}_m^-(z'+z_{m-1})/\mu_i} \mathrm{d}z' \tag{3.45}$$

$$\mathcal{A}_{gm}(\mu_s, \phi_s; \mu_i, \phi_i) = \int_{-z_m}^{-z_{m-1}} e^{\boldsymbol{\kappa}_m^+(z_{m-1}+z')/\mu_s} \mathcal{P}_m(\mu_s, \phi_s; \mu_i, \phi_i) e^{-\boldsymbol{\kappa}_m^+(z'+z_m)/\mu_i} \mathrm{d}z' \tag{3.46}$$

$$\mathcal{A}_{mdir}(\mu_s, \phi_s; \mu_i, \phi_i) = \int_{-z_m}^{-z_{m-1}} e^{\boldsymbol{\kappa}_m^+(z_{m-1}+z')/\mu_s} \mathcal{P}_m(\mu_s, \phi_s; -\mu_i, \phi_i) e^{\boldsymbol{\kappa}_m^-(z'+z_{m-1})/\mu_i} \mathrm{d}z' \tag{3.47}$$

$\mathcal{A}_{gmg}$, $\mathcal{A}_{mg}$, $\mathcal{A}_{gm}$ and $\mathcal{A}_{mdir}$ represent the scattering processes in Layer m caused by all the components respectively, where the terms of $\mathcal{P}_m(\mu_s, \phi_s; \mu_i, \phi_i)$ are source function computed from the modified Mueller matrices, the argument inside indicates the wave intensity is scattered from (μ_i, ϕ_i) direction to (μ_s, ϕ_s) direction.

The total contribution by the $m-th$ layer is denoted by $\mathcal{T}_m(\mu_s, \phi_s; -\mu_i; \phi_i)$.

$$\begin{aligned} \mathcal{T}_m(\mu_s, \phi_s; -\mu_i, \phi_i) &= \mathcal{T}_{gmg}(\mu_s, \phi_s; -\mu_i, \phi_i) + \mathcal{T}_{mg}(\mu_s, \phi_s; -\mu_i, \phi_i) \\ &+ \mathcal{T}_{gm}(\mu_s, \phi_s; -\mu_i, \phi_i) + \mathcal{T}_{mdir}(\mu_s, \phi_s; -\mu_i, \phi_i) \end{aligned} \tag{3.48}$$

The incident intensity is also scattered by the underlying ground surface when it propagates downward to the ground, which then propagates upward back to the air. The ground direct scattering can be written in a similar way as the specular reflection part by using a bistatic scattering matrix $\mathcal{G}(\mu_s, \phi; -\mu_i, \phi_i)$

$$\mathcal{T}_g(\mu_s, \phi; -\mu_i, \phi_i) = \Big(\prod_{m=1}^{L} e^{-\boldsymbol{\kappa}_m^+ d_m/\mu_s}\Big)\mathcal{G}(\mu_s, \phi; -\mu_i, \phi_i)\Big(\prod_{m=1}^{L} e^{-\boldsymbol{\kappa}_m^- d_m/\mu_i}\Big) \tag{3.49}$$

where $\mathcal{G}(\mu_s, \phi; -\mu_i, \phi_i)$ is given by the roughs surface model of the ground.

The total bistatic scattering from the multi-layer canopy over a ground surface is obtained by adding $\mathcal{T}_g$ to $\mathcal{T}_{canopy}$

$$\mathcal{T}_{total}(\mu_s, \phi; -\mu_i, \phi_i) = \mathcal{T}_{canopy}(\mu_s, \phi; -\mu_i, \phi_i) + \mathcal{T}_g(\mu_s, \phi; -\mu_i, \phi_i) \tag{3.50}$$

which is the direct first order RT equation solution.

3.3 Multi-MIMICS Model Development

3.3.1 First Order Multi-MIMICS Scattering Mechanisms

The first order solution demonstrates there are four scattering sources in each layer (Figure 3.3), which similar to those in the crown layer of Bi-MIMICS but with different propagation path and transmissivity matrices.

Since single trunk layer no longer exists in Multi-MIMICS and trunks are treated as other scatterers, there are four scattering mechanisms provided for trunk structures. However, because we model the trunks as vertical large cylinders, the model

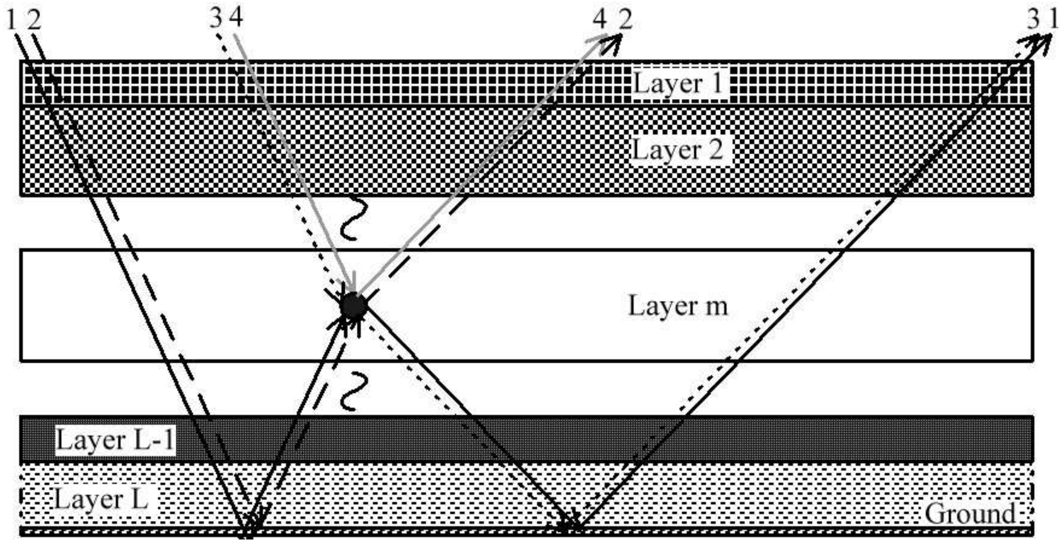

Figure 3.3: Four scattering contribution from each Layer according to the first order Multi-MIMICS solution. 1: scattering by this layer and double reflections by the ground; 2 and 3: scattering and reflection interactions between the canopy layer and the ground; 4: directing scattering by this layer of canopy. All four terms are attenuated along the propagation path by the upper and lower layers.

results show that strong scattering only exists in the forward ans specular directions, and scattered intensity in other direction are negligible, therefore, two in four of the mechanisms — direct trunk scattering and double ground reflection scattering are zeros. The other two remaining mechanisms are consistent with those in Bi-MIMICS.

Multi-MIMICS accommodates bistatic scattering configuration, so an additional term representing the coherent specular ground reflection exists in the specular direction. The ground scattering is also stronger in the specular direction than backscattering. A combination of the rough surface models is used for the ground surface scattering.

The total canopy scattering is the sum of all layer contributions and direct scattering from the rough ground. In Multi-MIMICS, as in Bi-MIMICS, the extinction, source and phase matrices are calculated as the statistical average over the type, quantity, size and orientation of the scatterers in each layer.

3.3.2 Modification for Overlapping Canopy Layers

For nonuniform canopies, overlapping between trunks of tall trees and crowns of short trees are common in mixed forest species as shown in Figure 3.1, another example for overlapping is trunks extending into crowns such as pine trees and spruces. Therefore, the scattering from each layer is no longer independent of the other layers and the solution derived in the previous section is insufficient.

When canopy layers are overlapped, the direct first order solution needs to be modified. An example of two overlapping canopy layer is shown in Figure 3.4. Each layer contains certain type of the scatterers, the extinction and phase matrices can be solved within each layer as if they were not overlapped. When two layer are place together, the upward and downward intensities of two layer are added together in the overlapped part, moreover, the wave propagates through or being scattered in three different regions, scattering can occur in the upper layer, overlapped layer or the lower layer. Because of RT theory, the extinction and scattering effects in the overlapped part are assumed to be enhanced and they can be added together incoherently. The overlapped part of the two layers can be treated as an additional layer, which contains more types of or more scatterers. Without taking into account multiple scattering, it can be concluded that the upper and lower layers maintain the original attenuation and scattering properties and the extinction and phase matrices in the middle layer are the sums of the top and bottom layers. The two-layer structure therefore becomes a three-layer system and hence the first order solution can be applied. As shown in Figure 3.4, the original top layer l has extinction matrices $\boldsymbol{\kappa}_l(\pm\mu_i, \phi_i)$, $\boldsymbol{\kappa}_l(\pm\mu_s, \phi_s)$ and phase matrices $\mathcal{P}_l(\pm\mu_s, \phi_s; \pm\mu_i, \phi_i)$, while the scattering properties of the bottom layer $l+1$ are $\boldsymbol{\kappa}_{l+1}(\pm\mu_i, \phi_i)$, $\boldsymbol{\kappa}_{l+1}(\pm\mu_s, \phi_s)$ and $\mathcal{P}_{l+1}(\pm\mu_s, \phi_s; \pm\mu_i, \phi_i)$. In the new three-layer system, the additional middle layer's extinction matrices are then $\boldsymbol{\kappa}_l(\pm\mu_i, \phi_i) + \boldsymbol{\kappa}_{l+1}(\pm\mu_i, \phi_i)$, $\boldsymbol{\kappa}_l(\pm\mu_s, \phi_s) + \boldsymbol{\kappa}_{l+1}(\pm\mu_s, \phi_s$ and its phase matrices are $\mathcal{P}_l(\pm\mu_s, \phi_s; \pm\mu_i, \phi_i) + \mathcal{P}_{l+1}(\pm\mu_s, \phi_s; \pm\mu_i, \phi_i)$. The scattering properties in the upper and lower layer keep unchanged. We can easily extend the solution to the case of three or more overlapping layers.

In this approach, scatterer are assumed independent among layers and interactions between scatterers (higher order scattering mechanism) are ignored. However, more consideration are needed for future higher order Multi-MIMICS development.

3.3.3 Tapered Trunk Model

Instead of using an approximate uniform trunk truncated at the crown layer bottom as in Bi-MIMICS, we use a tapered trunk by cascading layers with increasing trunk radius. As the trunk position is correlated among layers, the multi-layer solution cannot be applied to cascading trunk layers and a correction factor is therefore introduced. The particular advantages of using a tapered trunk model are that the actual forms of tree trunks are better represented and the trunks are able to grow into the crown layer rather than be truncated at the interface of the two layers.

Using RT theory, the extinction matrix and phase matrix are given in terms of the electric field scattering matrix $S_{2\times2}$. For a long cylinder, the approximate expression modified from an infinitely long cylinder is used such that [69]:

$$S_{2\times2}(\psi_i, \phi') = Q(\psi_i, \psi_s) \cdot S_\infty(\psi_i, \phi') \tag{3.51}$$

where ψ_i is the between the plane perpendicular to the cylinder axis and the direction of the propagation of the incident electric field and ψ_s is the angle between this plane and the direction of the propagation of the scattered electric field, ϕ' is the azimuth angle of the scattered field in this plane. $S_\infty(\psi_i, \phi')$ is the scattering matrix obtained from an infinity long homogeneous dielectric cylinder. $Q(\psi_i, \psi_s)$ is the factor to

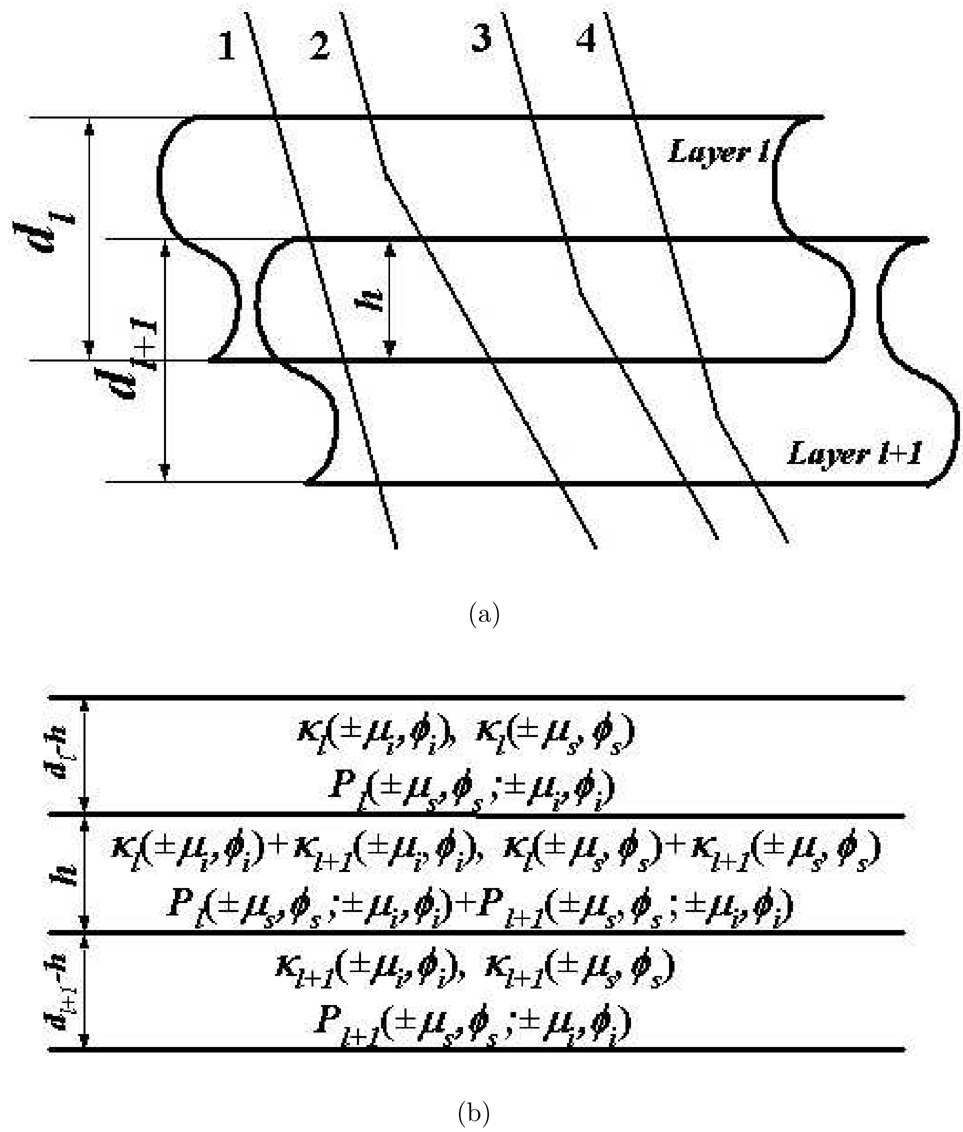

Figure 3.4: Propagating intensities in two overlapping Canopy Layers, the overlapped part of the two layers can be treated as an additional layer, which contains more types of or more scatterers. The extinction and phase matrices in the middle layer are the sums of the top and bottom layers.

transform the scattering matrix of infinite long cylinder to the finite length cylinder and is given by

$$Q(\psi_i, \psi_s) = \frac{iH \cos\psi_s}{\pi \cos\psi_i} \left\{ \frac{\sin[k_0(\sin\psi_i + \sin\psi_s)\frac{H}{2}]}{k_0(\sin\psi_i + \sin\psi_s)\frac{H}{2}} \right\} \tag{3.52}$$

where H is the trunk height.

In both the cases of forward scattering ($\psi_s = -\psi_i, \phi' = \pi$) and specular scattering ($\psi_s = -\psi_i, \phi' = 0$), the argument of the sinc function is zero and $\frac{\sin[k_0(\sin\psi_i+\sin\psi_s)\frac{H}{2}]}{k_0(\sin\psi_i+\sin\psi_s)\frac{H}{2}} = 1$, then Equation (3.52) reduces to

$$S_{2\times2}(\psi_i, \phi') = iH \cdot S_\infty(\psi_i, \phi') \tag{3.53}$$

Since effect of trunk's height on the scattering model is of our interest, other parameters can be treated as constants, we conclude that the scattering matrix $S_{2\times2}$ of a finite trunk is in proportion to its height H from Equation (3.53)

$$\mathbf{S}_{2\times2} \quad \propto \quad H \tag{3.54}$$

The phase matrix is in proportion to ${S_{2\times2}}^2$ (Equation (2.6)) and the extinction matrix is in proportion to $S_{2\times2}$ (Equation (2.10)). As a result, when other parameters are fixed, the phase matrix for a trunk layer of height H and density N trunks per square meter is

$$\mathcal{P} \quad \propto \quad \frac{N}{H}H^2 \qquad OR \qquad \mathcal{P} \quad \propto \quad H \quad (N \ \ is \ \ a \ \ constant) \tag{3.55}$$

and

$$\boldsymbol{\kappa} \quad \propto \quad \frac{N}{H}H \qquad OR \qquad \boldsymbol{\kappa} \quad = \quad constant \tag{3.56}$$

For layered trunk structures, we can't simply cascade the layers together as though they are independent canopy layers. Figure 3.5 is an example of when we divide a trunk layer into two half layers without considering the correlation of their positions. The scattering quantities are calculated within each sub-layer which is assigned with the same trunk density but half the trunk height.

The result in Figure 3.5(b) is clearly wrong, as we would expect the phase matrices in two half height layers to be the same as in one layer. The error arises as, when determining ${S_{2\times2}}^2$, the trunk positions in two layers are related and the wave should be added coherently. Therefore, a coherent correction factor $\frac{total-trunk-height}{sub-layer-height}$ needs to be applied to correct the phase matrices. The new phase matrix is then calculated as

$$\mathcal{P}_{new} = \frac{H_{total-trunk}}{H_{layer}} \mathcal{P}_{old} \tag{3.57}$$

where $\mathcal{P}_{old}$ is the phase matrix calculated by the first order solution and $\mathcal{P}_{new}$ denotes the new phase matrix corrected for coherent trunk positions. When the correction factor is applies as in Figure 3.5(c), we get the expected correct result. The method can be extended to tapered trunk layers with increasing trunk radius in the direction from the ground to the canopy top.

As illustration, Figure 3.6 compares the L-band (1.25 GHz) HH backscattering coefficients from 50m trunks with density of 9 trunks/ha based on two trunk models. In the first, the trunk radius is uniform at 24.5 cm while for the second, the trunk radius at the ground and top is 29.8 cm and 5 cm respectively (3.6(a)). The volume of the two trunks is identical. The simulation shows that when the uniform trunk is considered, the backscattering coefficient is underestimated from the upper part and overestimated from the lower part (Figure 6b). By contrast, the accumulated σ^0 from the ground to the higher layers leads to a better correspondence (Figure 6c). Therefore, the total backscattering coefficients from the two trunk models are similar but the contributions with changing height were different. When trunks

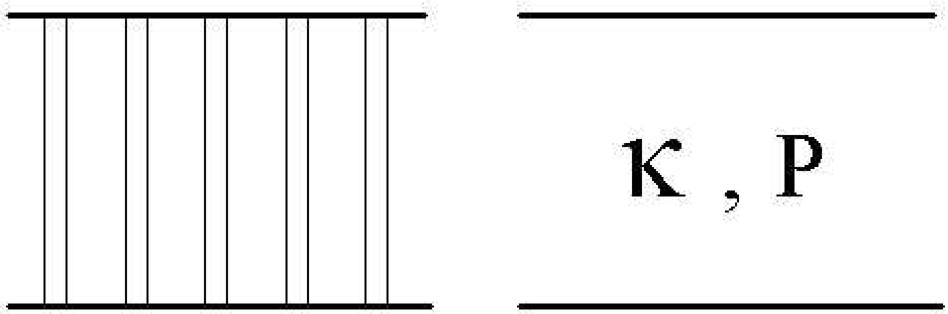

(a) One trunk layer

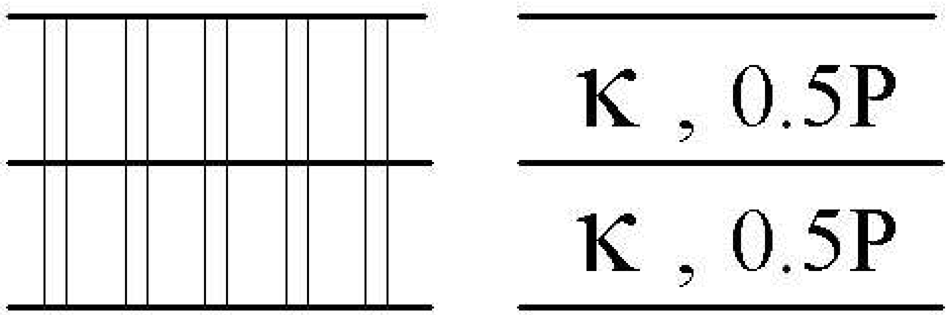

(b) Two equal halves without correction

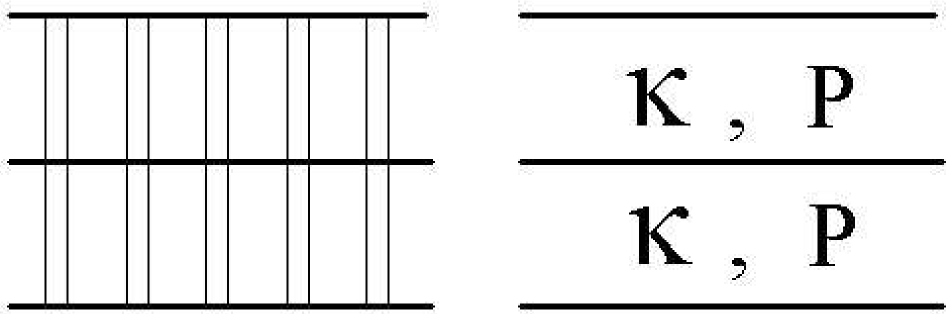

(c) Two equal halves with correction

Figure 3.5: Apply the first order solution directly to trunk layers without the correction factor. (a), (b) and (c) model the same the trunk structure. The trunks in (b) and (c) are modeled as two layers with half the height of the one layer trunk model in (a). Extinction and phase matrices of the layered trunk model are compared with and without the correlation factor.

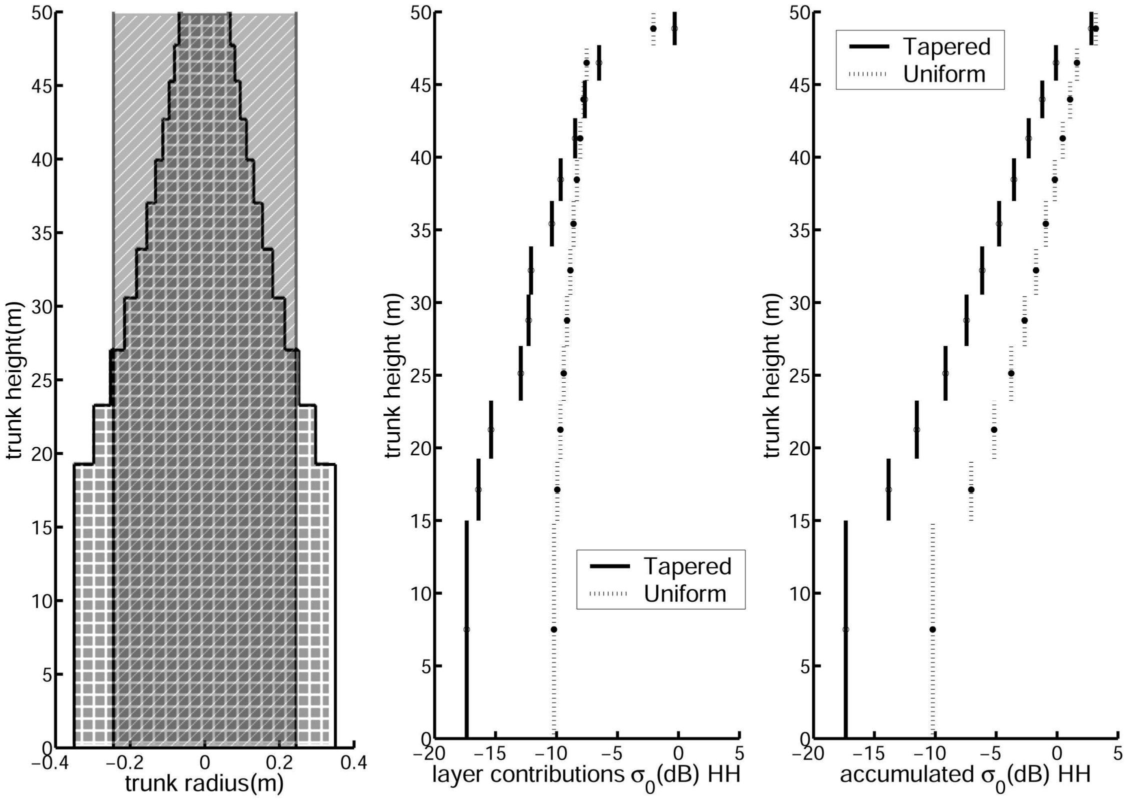

(a) (b) (c)

Figure 3.6: Trunk Backscattering by the uniform trunk model and tapered trunk model. (a) Two trunk models with the same volume. (b) Simulated LHH backscattering coefficient from two models. Individual layer's contribution is shown in (b). The uniform model underestimates the backscattering from the trunks' upper part and overestimates the backscattering from the trunks' lower part. (c) The accumulated backscattering from the ground to higher layers is shown as a function of layer locations. At the trunk top, the total backscattering coefficient of two models agree.

superimposed with branches and foliage, the tapered trunks can influence the total canopy backscattering coefficient.

3.4 Multi-MIMICS Model Implementation

3.4.1 Scattering Models of Canopy Components

Multi-MIMICS inherits the scattering models for all canopy constitutes such as trunk, branch, foliage and ground surface. However, there are a few changes when dealing with tapered trunk layers, it is necessary to indicate the ratio between the layer depth and the total trunk height as required in section 3.3.3.

Furthermore, scatterers are no longer named as branch and leaf, etc. since any combination of types of scatterers can be in any position inside the canopy. Instead, we use a general data structure which includes several variables representing scatterer type, scatterer parameters, scatterer position. Scatterer type indicates which scattering model should be used to compute the electric filed scattering matrix. Scatterer parameters include the geometric parameters of the scatterer such as size, shape and orientation as well as its dielectric constant. Scatterer position describes the layer that the scatterer is in.

3.4.2 Multiple Layers Structure

Bi-MIMICS's crown and trunk layer structure is replaced by multiple layers that don't have identifications, since layers can contains both trunks and crown compositions. Canopies layers instead are numbered and tracked by program. The input parameter of Multi-MIMICS is a list of single layers that either cascade or overlap. Each layer is considered homogeneous with distributions of a combination of types of scatterers. Location and depth of every layer must be specified. Multi-MIMICS reads in the input file, calculate all the extinction and phase matrices of each layer as the first step. The model then rearranges all the layers from top of the canopy to the ground according to their locations and depths. If overlapping among layers is detected at any range of height, Multi-MIMICS modifies the original layer structure and computer new layer's scattering matrices as described in section 3.3.2. The resulting canopy model may have more layers than the input file but are free of overlapping, thus the first order RT model solution can be applied to.

3.4.3 Scattering Processes and Solution Implementation

Since we are faced the multiplication operation of multiple 4×4 transmissivity matrices, it is essential to use the eigen value/vector decomposition to simplify the computation. The integration over the distribution of scatterers' shape, size and orientation are achieved by summation over finite range steps. So is the integration of phase matrices computed.

The total transform matrix is obtained by put all the scattering mechanism together through proper sequences.

3.5 Summary

For complex forests, particularly those that are in their natural state or subject to different levels of degradation, the existing two-layer microwave canopy scattering models are inappropriate. For this reason, a multi-layered approach that accounted for the vertical discontinuity of mixed forests and was based on RT theory was considered which resulted in the development of Multi-MIMICS.

Main contributions of this chapter are (1) Use a multi-layer canopy configuration to better represent forest structures with vertical discontinuity. (2) Solve multi-layer RT equations which is the direct first order Multi-MIMICS model. (3) Introduce overlapping canopy layers and modification to the first order Multi-MIMICS. (4)

Introduce a tapered trunk model and the solution of the correlation correction factor.

Chapter IV

MULTI-MIMICS MODEL VALIDATION AND APPLICATION

Multi-MIMICS is applied to real forest situations and validated by actual radar measurement. In this chapter, we use an extended dataset to parameterize Multi-MIMICS and also the original MIMICS model and evaluate the performance of each through comparison of actual and simulated σ^0 at different frequencies and polarizations. We also examine the additional understanding of microwave interaction with the forests through consideration of the different scattering mechanisms.

Section 4.1 describes the acquisition and processing of field and SAR data. The application of Multi-MIMICS to the test sites is then presented in Section 4.2 where simulated results are compared with those generated using MIMICS and recorded also by the AIRSAR, and the capabilities and limitations of the models are discussed in 4.3. Section 4.4 is the conclusion.

4.1 Field Measurement and SAR Data Acquisition

The development of Multi-MIMICS was motivated partly by a previous study [48] that focused on the simulation of SAR backscattering coefficient from mixed species forests near Injune in Queensland, Australia. In this research, which was part of a larger program aimed at investigating the use of SAR data for mapping forest biomass and structural diversity, the study benefited from the availability of NASA JPL AIRSAR data acquired over the area in September 2000 as part of the PACRIM II Mission.

4.1.1 Test Site

Several studies in Australia [3, 46] have investigated the relationship between above ground woody vegetation biomass and SAR data. However, during the 2000 NASA JPL PACRIM II AIRSAR Mission and under a joint program between several research agencies, a dedicated field and airborne campaign aimed at resolving issues relating to the use of SAR for quantifying forest biomass and structural diversity was conducted in Queensland [48]. The study focused on a 37×60 km area of forests and agricultural land west of Injune (Latitude $-25°32'$, Longitude $147°32'$), which is located in the Southern Brigalow Belt (SBB), a biogeographic region of southeast and central Queensland. The forests within the area contain a wide range of regeneration and degradation stages, due to differing land use, management histories and clearance regimes, and a diverse mix of species although several genera dominate [82]. In particular, Callitris glaucophylla (White Cypress Pine; herein referred to as CP-) is widespread, particularly in the undulating hills to the south of the study area where sandy soils predominate while Eucalyptus species favor the more alluvial plains. Angophora species, particularly A. leiocarpa (Smooth Barked Apple; SBA) occur throughout the study area. Few communities, however, can be considered to be homogeneous in terms of their structure, biomass and composition.

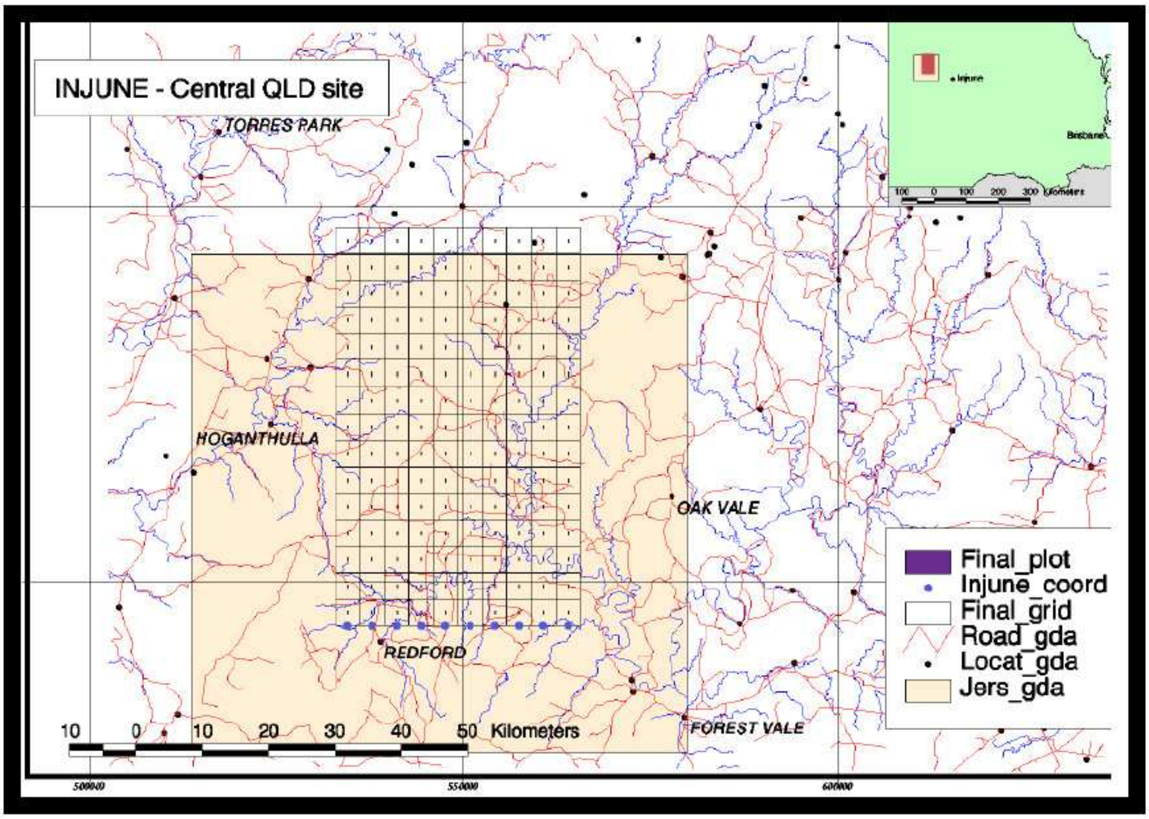

Figure 4.1: 150 primary sampling units (PSUs) (10 columns and 15 rows numbered progressively from top left to bottom right) over are of Injune, Australia. The size of each PSU is 500 × 150 m.

4.1.2 Field Data Collection

In July and August, 2000, large scale (1:4000) stereo aerial photography and LiDAR data were acquired over a systematic grid of 150 (10 columns and 15 rows numbered progressively from top left to bottom right) 500×150 m Primary Sampling Units (PSUs), with each PSU center located 4 km apart in the north-south and east-west directions [48]. Each PSU was further divided into thirty 50×50 m Secondary Sampling Units (SSUs; numbered from top left). The location and sampling schemes are shown in Figure 4.1 and 4.2. The composition of the forest was collected by summarizing the dominant species over the units.

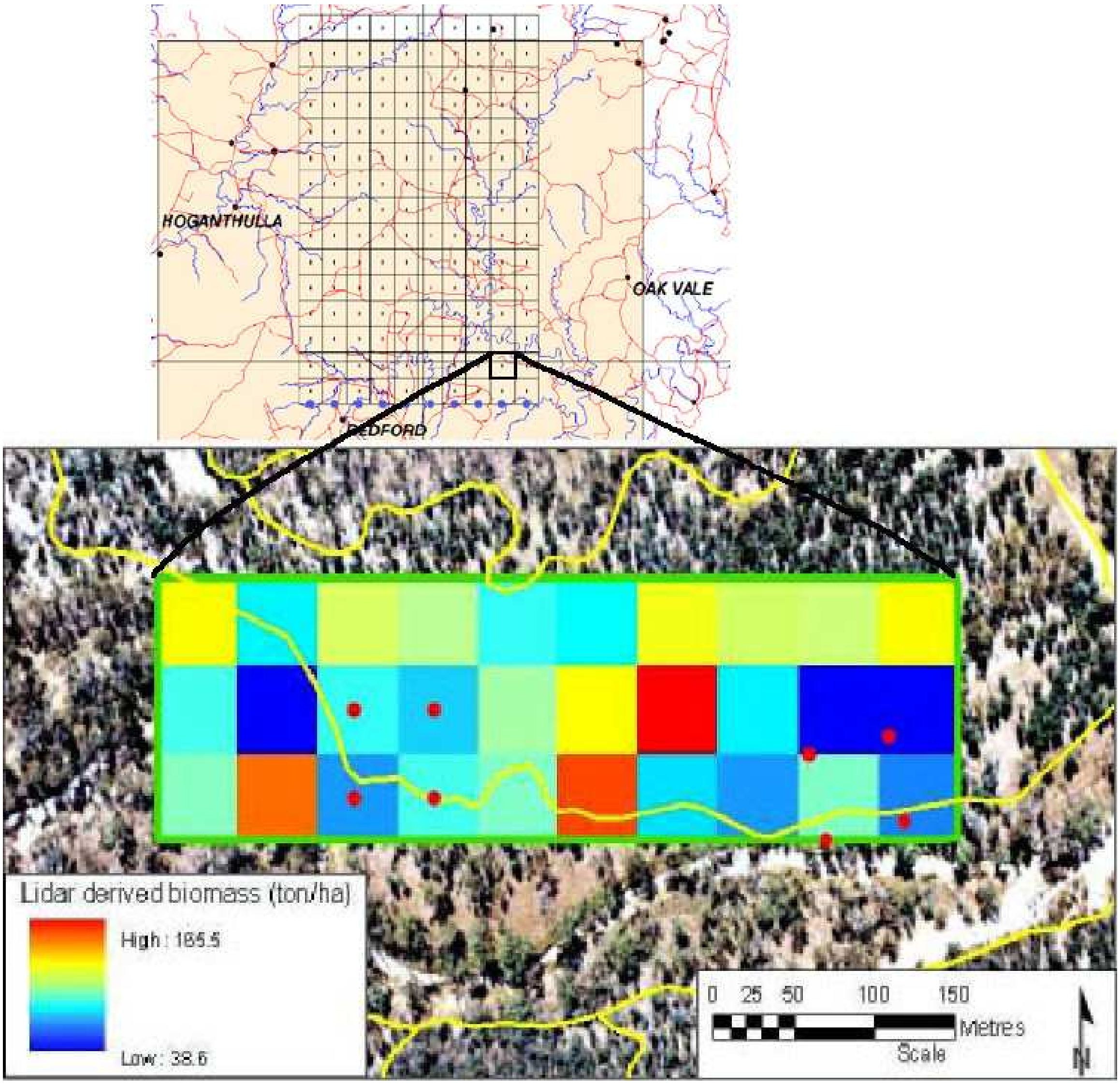

Figure 4.2: Each PSU is divided into thirty 50 × 50 m Secondary Sampling Units (SSUs; numbered from top left).

During a field campaign conducted over the same time-period, an extensive set of field measurements were collected from 36 SSUs located within 12 PSUs considered representative of the main forest types and regeneration stages occurring in the area. These measurements included trunk diameters at 30 (D30) and 130 cm (D130 or DBH; for all trees > 5 cm at D130), tree height, crown diameter and crown depth and each tree measured was identified to species [48]. Smaller (< 5 cm D130) individuals were measured in five 10×10 regrowth and understory plots. Digital pictures were taken of at least every 10th tree measured and soil dielectric constants and moisture contents were recorded for each SSU using a Time Domain Reflectometer (TDR) and through gravimetric methods.

The complex nature of these mixed forests is highlighted in Figure 4.3 [47] which shows the crown and trunk layers of two tall species (a pine and eucalypt) overlapping and an understory of various species of similar structural form. It is a true measurement of trees from a SSU.

Following field data collection, destructive harvesting of CP- (22 individuals) was undertaken to generate new allometric equations relating tree size to leaf, branch (< 1 cm, 1-4 cm, 4-10 cm, 10-20 cm etc.), and trunk biomass. Harvesting of Eucalpytus populnea (Poplar Box; PBX; n = 7), Eucalyptus melanaphloia (Silver-leaved ironbark; SLI; n=5) and Acacia harpophylla (Brigalow; BGL; n=1) was also undertaken to assess the validity of applying existing allometric equations [6, 29], generated by harvesting trees several hundred km distant, for estimating the total above ground and component biomass of trees at Injune. After harvesting, trees were divided into major components such as trunks, branches and leaves. Branches were divided into subcomponents as large and small branches. The number, size and orientation of these components were measured and categorized. Leaf size for main species

(a) 3D Illustration

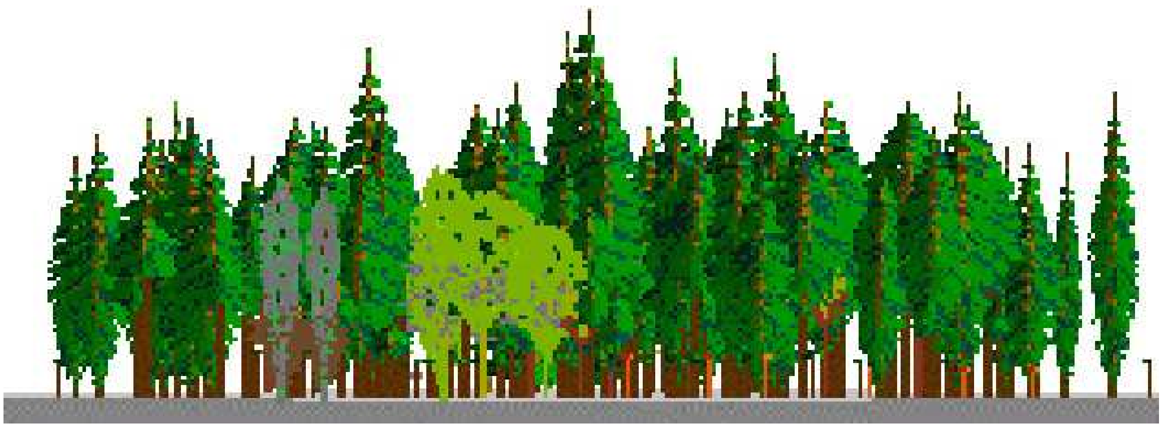

(b) 2D Profile

Figure 4.3: Layer constitutes of a mixed species forest. Field data collected from a 50 × 50 m area of Injune, Australia. The plot consists of mature callitris glaucophyllas($\sim$ 14 m), eucalyptus fibrosas($\sim$ 12 m) and callitris glaucophylla saplings($\sim$ 5 m).

(a) SLI (b) CP- (c) SBA

Figure 4.4: Major tree species from test sites. SLI: Eucalyptus melanaphloia (Silver-leaved Ironbark); CP-: Callitris glaucophylla (White Cypress Pine); SBA: Angophora leiocarpa (Smooth Barked Apple).

was also measured and photographed. The harvesting also allowed the number and size of canopy elements to be estimated and provided measures of moisture content throughout each tree harvested. Figure 4.4 shows photos of a few major species.

4.1.3 SAR Data Acquisition and Processing

AIRSAR data (four strips of 12×80 km) were acquired across the entire PSU grid on 3rd September 2000. C-band ($\sim$ 6 cm wavelength, 5.288 GHz), L-band ($\sim$ 25 cm wavelength; 1.238 GHz) and P-band ($\sim$ 68 cm, 0.428 GHz) at three distinct polarizations (HH, VV and HV) were recorded (9 channels) and processed by JPL in the standard format of compressed Stokes matrix, giving a stated calibration accuracy of 1 dB. The incidence angle at which the selected SSUs were observed ranged from 29° to 59°. The standard AIRSAR data, which had a pixel size of 3.3×4.6 m in slant range, were ground projected and resampled to a pixel size of 10×10 m. Figure 4.5 is a composite of three channels of C-band AIRSAR raw image which covers the area of Injune. A cross track correction was applied to the images to reduce the backscattering coefficient variation caused by incidence angle variation. Geometric rectification was then achieved using a 3rd order polynomial nearest neighbor transformation based on ground control points common within the AIRSAR and pre-registered Landsat ETM+ data (September, 2000) of the study area. Each SSU therefore occupied a 5×5 block of pixels in the image and, under the assumption of homogeneity within the SSU, the average backscattering coefficients over these 25 pixels were calculated to reduce noise. Figure 4.6 is an example that trees inside of SSU P111-12 scatter over the AIRSAR image, a block of CHH channel is shown in the figure. These averaged data were then compared against that simulated using both the MIMICS and multi-MIMICS model.

4.2 Model Application

4.2.1 Model Parameters

The available field measurements were used to parameterize the two models (multi-MIMICS and MIMICS) for each SSU (Table 4.1). In addition, the digital photographs were used to determine the branch orientations and pdf exponents while the data on trees harvested were used to estimate the dielectric constants of the branches and foliage (Table 4.2). The radar incidence angle for each SSU was also estimated from AIRSAR images (Table 4.3). These forest inventory data were also seen in [48]). In all cases, the sum of the biomass of the simulated components (based on dimensions and wood density) for all contained species equated to the biomass observed for the SSU.

For Multi-MIMICS, each tree species was modeled separately by a crown layer and a trunk layer which could overlap if the trunk was known to grow into the crown

Figure 4.5: Composite of three channels of C-band AIRSAR raw image which covers the area of Injune. Red — CHH, Green — CHH, Blue — CHV. Slant range pixel size: 3.3×4.6 m.

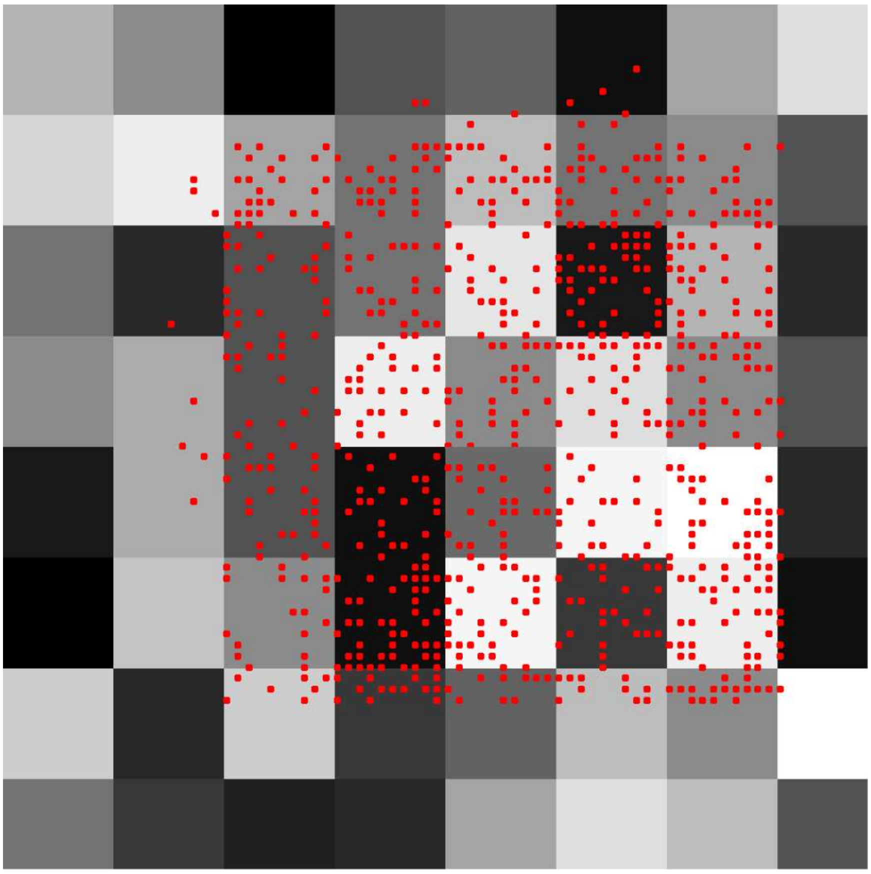

Figure 4.6: CHH band processed ground range AIRSAR image. Ground range pixel size: 10×10 m. 781 trees in SSU P111-12 are scattered over the area and their center locations are plotted as dots.

(e.g., in the case of CP-). If five tree stands were considered, for example, ten layers were first generated. Each layer of specified height was then populated with estimates of the densities, dimensions, orientations and dielectric constants of scatterers. The input layers were then rearranged from top to bottom and overlapping parts were treated accordingly, and the multi-MIMICS RT solution to the canopy may include more than ten layers. An approximately uniform trunk that extended into the crown layer was used as trunk tapering factors were not employed due to the lack of field measurement, although future simulations will integrate published taper functions available for the species. Sensor and environmental parameters were then defined, including microwave frequency, incidence and scattering directions and ground surface characteristics (e.g., soil dielectrics, RMS height and correlation length). The incidence angle for each SSU was determined from the AIRSAR data, which was warranted due to the relative flatness of the ground terrain.

4.2.2 Backscattering Simulation by Multi-MIMICS and Standard MIMICS Model

Based on the model input parameters, simulation of the SAR backscattering at all frequencies and polarizations was undertaken using multi-MIMICS and MIMICS and a comparison between actual and simulated σ^0 was undertaken. To illustrate the results for a relatively simple but typical stand, P111-12 with two species (CP- and SLI) but three groups (SLI and CP - with D130 $\geq$ 10 cm and CP- $<$ 10 cm respectively) was considered. The above ground biomass of this stand was estimated at 130 Mg/ha and the SSU contained 781 trees of which 18 and 89 were SLI and CP- (D130 $\geq$ 10) respectively while the remaining 674 were CP- (D130 $<$ 10). However, the CP- (D130 $\geq$ 10) contributed more than 50% of the biomass with the SLI contributing approximately 25%. Approximately 75% of the biomass was contained

Table 4.1: Forest Structural Characterizes of 15 SSUs.

SSU	Species	Canopy Density (/m^2)	Top Height(m)	Crown Depth(m)	Trunk Height(m)	Trunk Diameter(cm)	Large Branch Length(m)	Small Branch Length(m)	Large Branch Radius(cm)	Small Branch Radius(cm)	Large Branch Number	Small Branch Number	Leaf Number
P23-15	PBX	0.032	13.8	6.9	6.9	13.79	0.4	1.5	6.96	0.5	3782	33154	1112470
	CP-	0.012	9.2	7.7	8.2	9.97	3.17	1	1	0.5	1021	17723	945643
	CP-	0.4036	5	2.5	4	1.98	-	1	-	0.5	-	34944	1587629
	SBA	0.004	12.4	7.6	4.8	19.73	6.1	1.5	9.96	0.5	4	687	61033
	SLI	0.1204	5	2.5	2.5	3.3	1.5	1	1.66	0.5	362	17096	2056
P23-16	SLI	0.0028	11.5	6	5.5	19.5	4.5	1.5	6.5	0.5	21	2339	121753
	CP-	0.0016	12.5	10	12.5	25.3	4.74	1	1	0.5	387	4641	256244
	BRH	0.0072	6.5	4.5	6.5	15	-	1	-	0.5	-	8425	233003
	SBA	0.012	12	9.5	9.5	26.1	8	1.5	8.7	0.5	134	20610	1831004
	SBA	0.1012	0.5	0.25	0.25	2.5	0.25	1	0.84	0.5	623	4355	170009
P58-24	PBX	0.0172	19	14	7.5	17.99	12.5	1.5	9.56	0.5	105	24323	971206
	CP-	0.0672	2.4	1.2	1.2	2.1	-	1	-	0.5	-	13793	254635
P58-29	SLI	0.0076	10.3	8.6	4.7	22	3.6	1.5	9.16	0.5	117	11956	679909
	PBX	0.018	9.4	3.3	7.6	16.49	2.8	1.5	6.46	0.5	690	15144	894172
	SLI	0.3088	6	3	3	2.82	2	1	1.56	0.5	654	37352	1382205
P81-8	ECH	0.016	12.7	5.4	7.3	10.32	3.9	2	5.06	0.5	272	6196	269823
	CP-	0.016	17.8	11.5	6.3	17.49	2.61	1	1	0.5	9621	53179	2855806
	SBA	0.0036	20	15.9	4.1	18.48	14.4	1.5	9.34	0.5	24	6912	624238
	BRH	0.0232	3	1.4	1.6	3.96	0.4	1	2	0.5	3021	3408	264932
P81-11	CP-	0.012	14.6	9	5.6	22.2	2.28	1	1	0.5	10454	44083	2462246
	CP-	0.0408	1.6	0.8	0.8	5	-	1	-	0.5	-	3975	336201
	SBA	0.0028	25.6	20.3	5.3	45.57	10.8	1	21.7	0.5	34	19871	2217461
	ANE	0.0252	6.5	5.2	1.3	3.99	4.2	1	1.9	0.5	691	7384	352782

Table 4.1: Forest Structural Characterizes of 15 SSUs (Continued).

SSU	Species	Canopy Density (/m^2)	Top Height(m)	Crown Depth(m)	Trunk Height(m)	Trunk Diameter(cm)	Large Branch Length(m)	Small Branch Length(m)	Large Branch Radius(cm)	Small Branch Radius(cm)	Large Branch Number	Small Branch Number	Leaf Number
P111-12	SLI	0.0072	13.7	11.6	6.68	25.8	5.1	1.5	8.6	0.5	126	13630	796563
	CP-	0.0356	15	9.9	5.1	28.5	3.82	1	1	0.5	9580	98415	5420834
	CP-	0.2696	5	2.5	2.5	5	-	1	-	0.5	-	100920	5002367
P114-4	CP-	0.042	17	10	7	12.14	1.7	1	1	0.5	11742	81519	4410974
	CP-	0.0092	7	3.5	3.5	4.16	-	1	-	0.5	-	2605	127196
	SBA	0.0004	16	11	13	76.32	9.5	1.5	28.26	0.5	9	3883	458114
	SBA	0.352	1.5	0.75	0.75	1.8	0.75	1	0.66	0.5	45	10577	360177
P114-12	CP-	0.0132	10.9	8	10.4	13.2	2.32	1	1	0.5	2617	25234	1364353
	CP-	0.0168	6	3	5	3.4	-	1	-	0.5	-	2682	126583
	SBA	0.0044	13.3	5.7	7.6	14.98	4.2	1.5	7.56	0.5	69	5509	467559
	ANE	0.0529	3.7	1.85	1.85	0.99	1	1	1.85	0.5	244	22031	1056220
P142-2	PBX	0.0252	9.5	5.9	5.1	14.3	5.4	1	1.5	0.5	236	21390	760760
P142-18	PBX	0.0204	13.3	10.1	4.6	20.16	7.6	1.5	8.4	0.5	153	22875	1595931
P142-20	PBX	0.0212	11.5	4.2	7.3	13.79	2.7	1.5	6.96	0.5	506	14673	1442699
	SBA	0.038	6	3	3	5.94	2	1	3	0.5	199	13607	550138
P144-13	ECH	0.0056	11.3	9.6	8.7	26.32	8.1	1.5	5.4	0.5	348	9402	299541
	CFM	0.0336	11	5.4	5.6	11.82	4.47	1	1	0.5	3082	67714	1926119
P144-19	SLI	0.0036	11	7.7	3.3	23.18	6.2	1.5	11.2	0.5	46	8488	512789
	CP-	0.0196	11.5	9.5	11	14.94	3.04	1	1	0.5	3372	39794	2158231
	CP-	0.1204	5.5	2.75	2.75	3.43	-	1	-	0.5	-	25110	1203118
P148-16	SLI	0.0116	18.5	11.5	7	25.74	10	1.5	13	0.5	68	27351	1652321
	CP-	0.0036	10	8.2	10	13.13	3.39	1	1	0.5	511	7041	381155
	CP-	0.288	2.9	1.45	2.9	1.13	-	1	-	0.5	-	8214	349865
	1018	0.1432	2.2	1.1	2.2	1.98	0.1	1	1	0.5	39113	4084	542616

Table 4.2: Tree and Soil Permittivities at C-, L- and P-band of 15 SSUs.

SSU	Species	Branch Dielectric Constant(relative)			Soil Dielectric Constant(relative)		
		C	L	P	C	L	P
P23-15	PBX	20,2	22,2	25,2	2,1	2,1	3,1
	CP-	15,2	15,2	25,2	2,1	2,1	3,1
	CP-	15,2	15,2	25,2	2,1	2,1	3,1
	SBA	20,2	22,2	25,2	2,1	2,1	3,1
	SLI	20,2	22,2	25,2	2,1	2,1	3,1
P23-16	SLI	20,2	22,2	25,2	2,1	2,1	3,1
	CP-	12,2	15,2	25,2	2,1	2,1	3,1
	BRH	18,2	18,2	22,2	2,1	2,1	3,1
	SBA	18,2	18,2	22,2	2,1	2,1	3,1
	SBA	18,2	18,2	22,2	2,1	2,1	3,1
P58-24	PBX	20,2	20,2	25,2	2,1	2,1	3,1
	CP-	12,2	20,2	25,2	2,1	2,1	3,1
P58-29	SLI	12,2	20,2	28,2	2,1	2,1	5,1.5
	PBX	20,2	20,2	25,2	2,1	2,1	5,1.5
	SLI	12,2	20,2	28,2	2,1	2,1	5,1.5
P81-8	ECH	18,2	18,2	25,2	2,1	2,0.5	3,1
	CP-	12,2	15,2	25,2	2,1	2,0.5	3,1
	SBA	18,2	18,2	25,2	2,1	2,0.5	3,1
	BRH	12,2	15,2	25,2	2,1	2,0.5	3,1
P81-11	CP-	12,2	18,2	25,2	2,1	2,0.5	3,1
	CP-	12,2	15,2	25,2	2,1	2,0.5	3,1
	SBA	20,2	18,2	25,2	2,1	2,0.5	3,1
	ANE	12,2	15,2	25,2	2,1	2,0.5	3,1

Table 4.2: Tree and Soil Permittivities at C-, L- and P-band of 15 SSUs (Continued).

SSU	Species	Branch Dielectric Constant(relative)			Soil Dielectric Constant(relative)		
		C	L	P	C	L	P
P111-12	SLI	18,2	20,2	25,2	2,1	2,0.5	3,1
	CP-	12,2	15,2	25,2	2,1	2,0.5	3,1
	CP-	12,2	15,2	25,2	2,1	2,0.5	3,1
P114-4	CP-	20,2	22,2	28,3	4,1	5,1	12,1
	CP-	20,2	22,2	28,3	4,1	5,1	12,1
	SBA	18,2	18,2	20,2	4,1	5,1	12,1
	SBA	18,2	18,2	20,2	4,1	5,1	12,1
P114-12	CP-	20,2	20,2	22,2	2,1	2,1	3,1
	CP-	20,2	20,2	22,2	2,1	2,1	3,1
	SBA	20,2	18,2	22,2	2,1	2,1	3,1
	ANE	20,3	22,3	25,3	2,1	2,1	3,1
P142-2	PBX	20,2	20,2	25,2	2,1	2,1	3,1
P142-18	PBX	22,2	25,2	30,3	2,1	2,1	4,2
P142-20	PBX	22,2	22,2	25,2	2,1	2,0.5	3,1
	SBA	12,2	15,2	25,2	2,1	2,0.5	3,1
P144-13	ECH	12,2	15,2	25,2	2,1	2,1	3,1
	CFM	12,2	15,2	25,2	2,1	2,1	3,1
P144-19	SLI	12,2	15,2	25,2	2,1	2,1	3,1
	CP-	12,2	15,2	25,2	2,1	2,1	3,1
	CP-	12,2	15,2	25,2	2,1	2,1	3,1
P148-16	SLI	12,2	15,2	25,2	2,1	2,1	3,1
	CP-	12,2	15,2	25,2	2,1	2,1	3,1
	CP-	12,2	15,2	25,2	2,1	2,1	3,1
	1018	12,2	15,2	25,2	2,1	2,1	3,1

Table 4.3: Backscattering Radar Incidence Angles Estimated Fromm AIRSAR Images of 15 SSUs.

SSU	P23-15	P23-16	P58-24	P58-29	P81-8
Incidence Angle (°)	33.06	33.06	30.10	30.10	58.95
SSU	P81-11	P111-12	P114-4	P114-12	P142-2
Incidence Angle (°)	58.95	58.77	46.98	46.98	48.38
SSU	P142-18	P142-20	P144-13	P144-19	P148-16
Incidence Angle (°)	48.38	48.38	46.98	46.98	30.10

within the tree trunks. Figure 4.7 illustrates the relative size of three types.

The multi-MIMICS parameter input file was generated from 4.1. For the two-layer MIMICS, the crown depth was set to 12.9 m and the trunk height to 2.1 m. The densities of canopy scattering components (branches, leaves) were calculated individually for each species. The comparison of actual (mean) and simulated (multi-MIMICS and MIMICS) backscattering coefficient, σ^0, (dB) is shown in Figure 4.8, with the error bars representing the dynamic range (σ_{0min} and σ_{0max}) of the AIRSAR data.

The σ^0 simulated by both models was within the AIRSAR dynamic range. At C-band, both simulations were similar with discrepancies of around 1 dB for C-band HH, VV and HV. As the upper layer of the canopy contributed the greatest backscatter, differences at C-band were not expected. However, both models underestimated σ^0 at C-band which could be attributed largely to minor errors in the calibration of the AIRSAR data. At L-band and P-band, double bounce scattering primarily from the tree trunks became noticeable and the multi-MIMICS showed a significant improvement over the MIMICS simulation, with the difference between simulated and actual decreasing from -3.41 dB to 0.06 dB (for L-band HH) and from -3.90 to

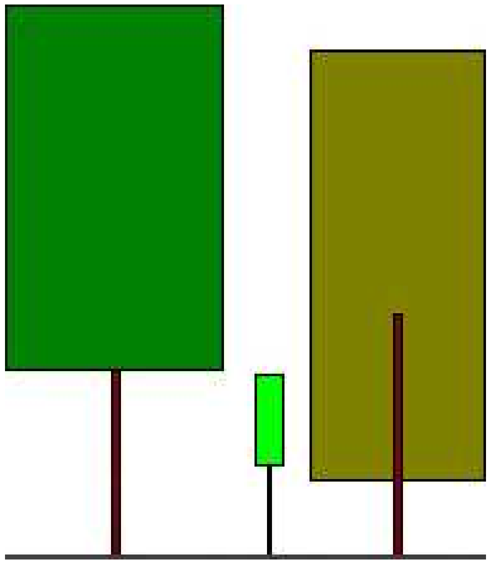

Figure 4.7: Relative size of three groups of two species in SSU P111-12. They are large CP- (Height= 15 m, Crown radius= 2.93 m, Trunk Height= 5.1 m), small CP- (Height= 5 m, Crown radius= 0.4 m, Trunk Height= 2.5 m) and SLI (Height= 13.7 m, Crown radius= 2.35 m, Trunk Height= 6.7 m) from the left.

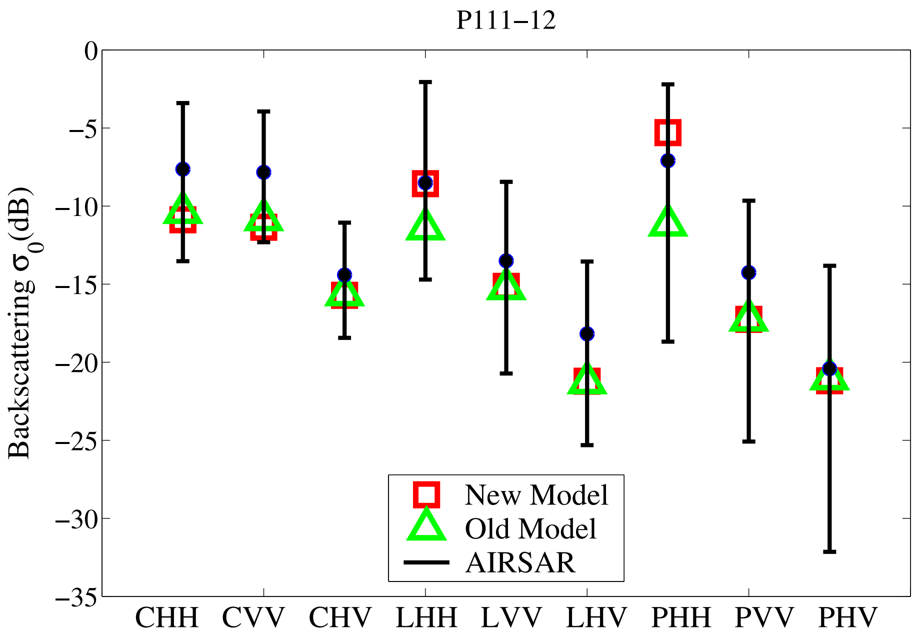

Figure 4.8: AIRSAR measured and model simulated backscattering coefficients for P111-12. Results are shown for C-, L- and P-bands at HH, VV and HV polarizations. The AIRSAR data are provided with dynamic ranges (bars) and mean values (block dots). The square marks present Multi-MIMICS's simulation and the triangular marks show old MIMICS's simulation.

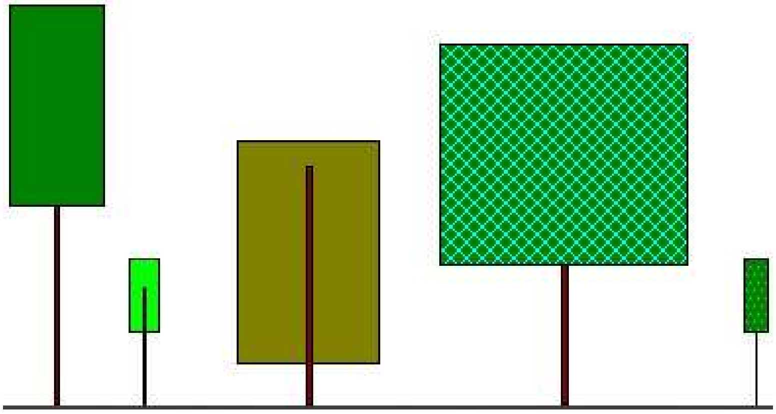

Figure 4.9: Relative size of five groups of four species in SSU P23-15. They are PBX (Height= 13.8 m, Crown radius= 1.63 m, Trunk Height= 6.9 m), small CP- (Height= 5 m, Crown radius= 0.5 m, Trunk Height= 4 m), large CP- (Height= 9.2 m, Crown radius= 2.42 m, Trunk Height= 8.2 m), SBA (Height= 13.7 m, Crown radius= 2.35 m, Trunk Height= 6.7 m) and SLI (Height= 5 m, Crown radius= 2.35 m, Trunk Height= 2.5 m) from the left.

1.79 dB (for P-band HH).

As both SLI and CP- (D130 $\geq$ 10) that provided the majority of biomass had similar heights and crown depths, the two layer crown-trunk configuration was a close approximation to the multi-layer canopy structure and hence both models offer reasonable predictions of σ^0. However, where forests with more complex vertical structures were considered, MIMICS failed to produce a reliable prediction whereas multi-MIMICS was more successful. The complex situation was illustrated by considering the forests represented by SSU P23-15 which consisted of five species, namely PBX (n = 80), CP- with D130 $\geq$ 10 cm (n = 30), SBA (n = 1), CP- with D130 $<$ 10 cm (n = 1009) and SLI (n = 301) and of heights ranging from short (5 m) to medium tall (9.2 m) and tall (13.8 m). The estimated biomass for P23-15 was 74 Mg/ha. The relative size of five types are shown in Figure 4.9.

For MIMICS, the crown-trunk canopy model was used with a crown and trunk layer depth of 11.3 m and 2.5 m respectively. Multi-MIMICS was parameterized using the inputs listed in Table 4.1 and the comparison of actual (mean) and simulated σ^0 is shown in Figure 4.10. In this case, σ^0 simulated by MIMICS was outside of the dynamic range of the AIRSAR-data at C-band and L-band (with the exception of L-band VV) and generally underestimated (including for P-band HH and VV). Part of the reason for this underestimate was that MIMICS truncated the trunk length, which resulted in a reduction in σ^0 at HH polarizations in particular. As MIMICS also overestimated the canopy volume, the scatterer density within the crown decreased, which partly explained the underestimation at C-band. For all channels, the mean error between σ^0 simulated by MIMICS and recorded (mean) by the AIRSAR (all nine channels) was -3.98 dB and the Root Mean Square Error (RMSE) was 5.26 dB. By contrast, the mean errors was -1.18 dB and RMSE was 2.40 dB where simulations were performed with multi-MIMICS. These comparisons indicated that multi-MIMICS provided a significantly improved or equivalent simulation of σ^0 at most frequencies and polarizations compared to MIMICS.

4.2.3 Comparison between Multi-MIMICS Simulations and Actual SAR Data

Simulations were conducted on a further thirteen forests. In the majority of cases (Figure 4.11), σ^0 simulated by multi-MIMICS was within the dynamic range of the AIRSAR data. At C-band, however, simulations were generally lower that observed by the AIRSAR. At L-band, in particular, but also P-band (with the exception of P-band HV polarization), a good correspondence between actual and simulated σ^0 was observed. Combining all fifteen plots (Figure 4.14), we observed that the 1:1 line intersected with most of the dynamic range bars of the AIRSAR data which indicates that the simulation is performing well. Even so, the under-estimation of σ^0 at C-band by Multi-MIMICS was apparent which was partly attributable to AIRSAR

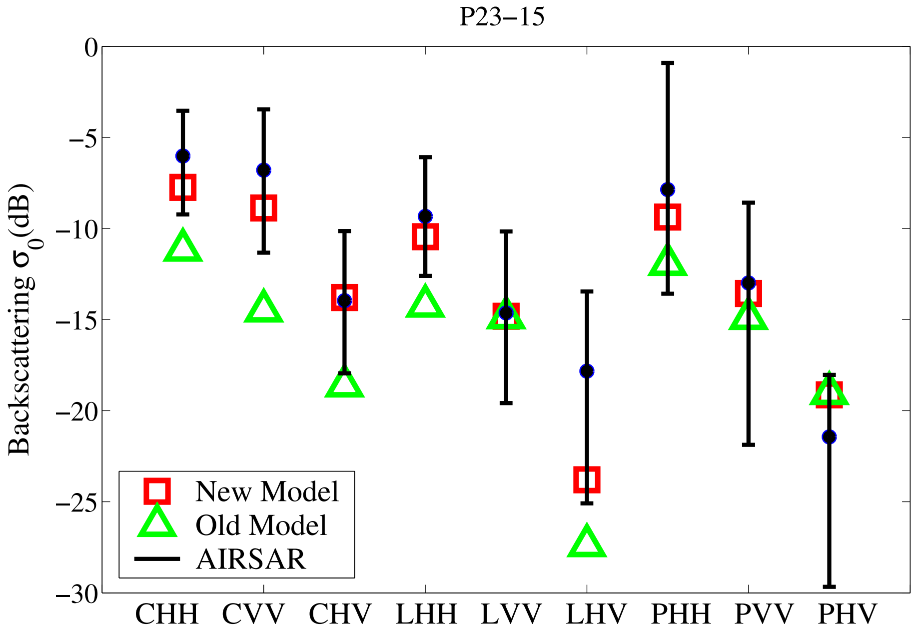

Figure 4.10: AIRSAR measured and model simulated backscattering coefficients for P23-15. Results are shown for C-, L- and P-bands at HH, VV and HV polarizations. The AIRSAR data are provided with dynamic ranges (bars) and mean values (block dots). The square marks present Multi-MIMICS's simulation and the triangular marks show old MIMICS's simulation.

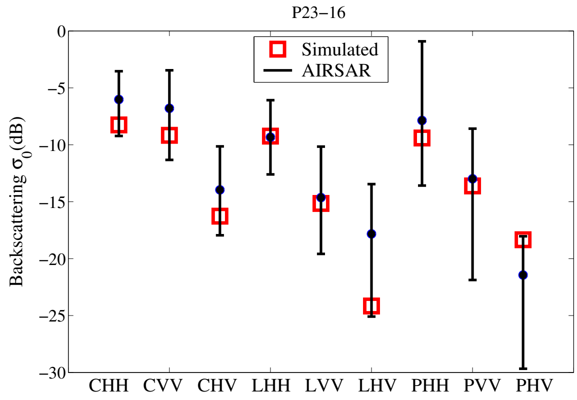

(a) P23-16

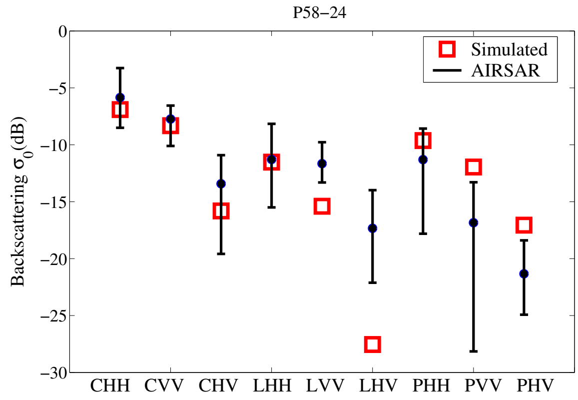

(b) P58-24

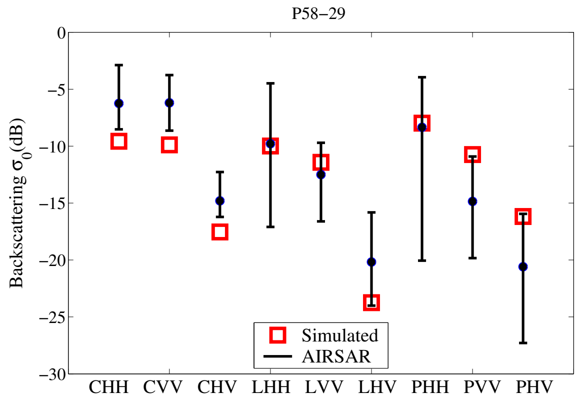

(c) P58-29

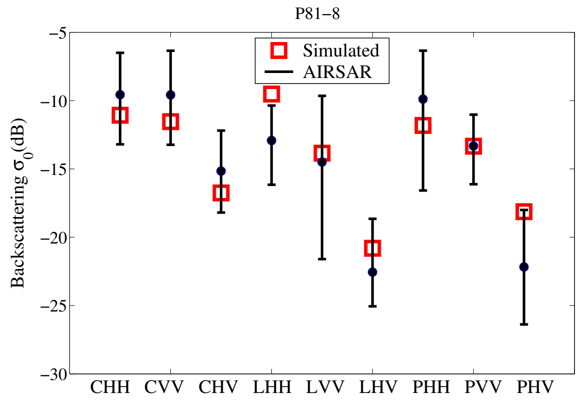

(d) P81-8

calibration errors. The model best fit the measurements at L-band HH and VV and P-band HH, although a few outliers were evident in the latter case, which may be attributable to the open nature of the forest canopies. For each channel, the mean error and RMSE are given in Table 4.4 and, in this calculation, we excluded the worst point for each channel on the assumption that these represented outliers. In this table, small absolute values of mean error indicated less bias between measurement and simulation while a small RMSE indicated good correspondence between two datasets.

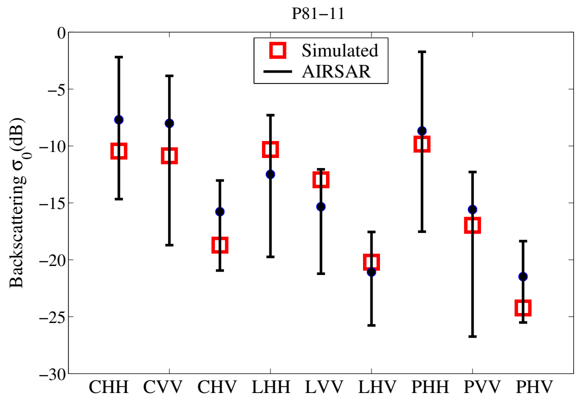

(e) P81-11

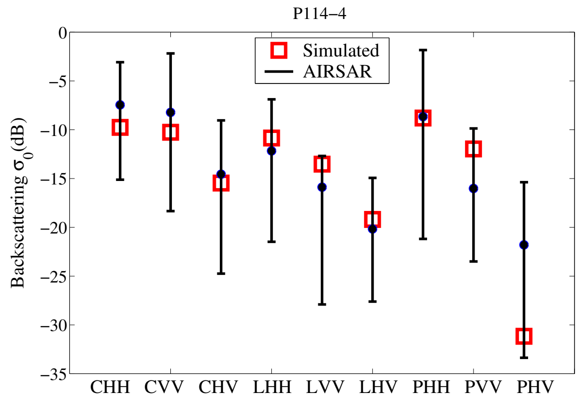

(f) P114-4

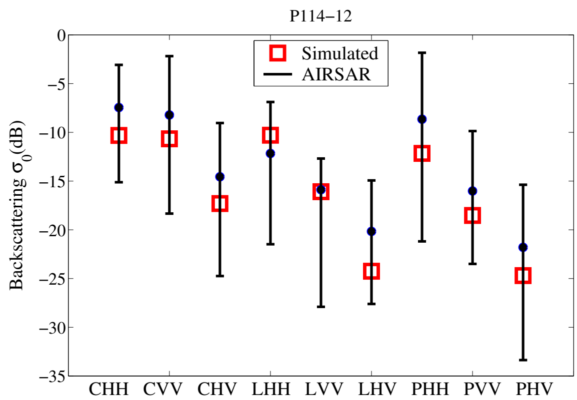

(g) P114-12

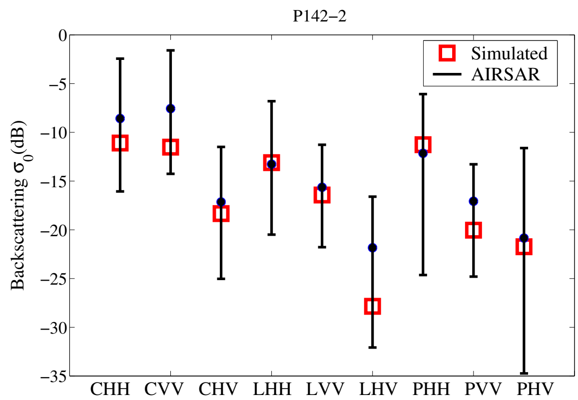

(h) P142-2

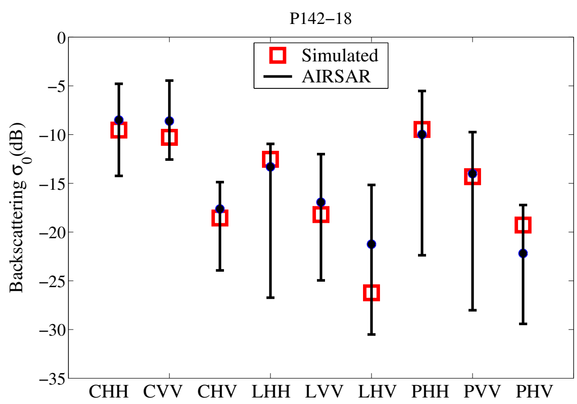

(i) P142-18

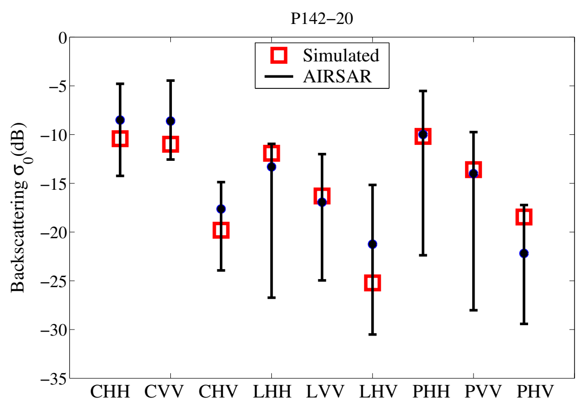

(j) P142-20

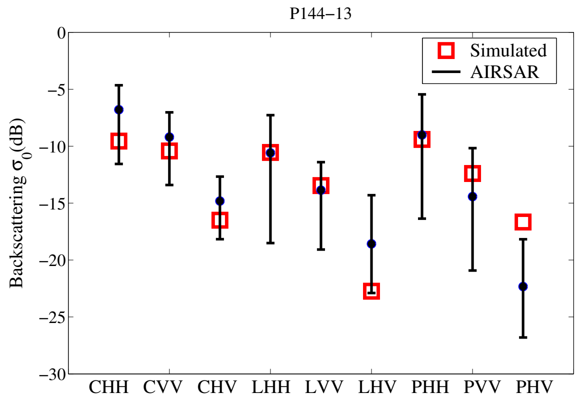

(k) P144-13

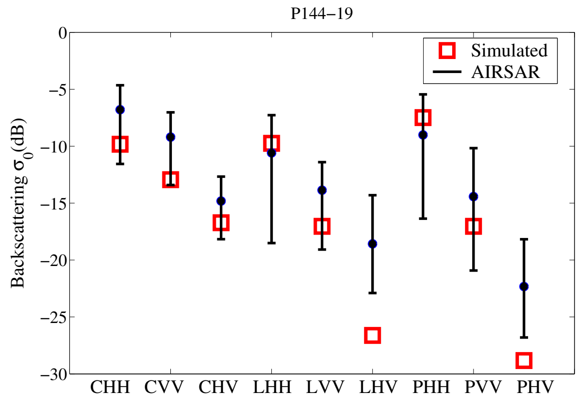

(l) P144-19

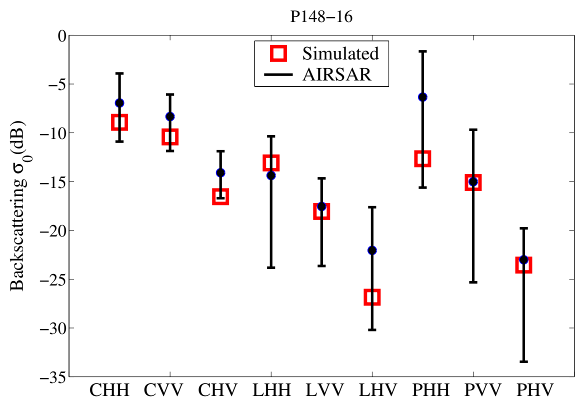

(m) P148-16

Figure 4.11: Backscattering simulation for thirteen test sites. AIRSAR measured and model simulated backscattering are compared for each SSU. The backscattering coefficients are plotted at multiple frequencies and polarizations. The AIRSAR measurement are shown by their dynamic range from minimum to maximum and their mean values. Simulated backscattering coefficients are plotted against the AIRSAR data.

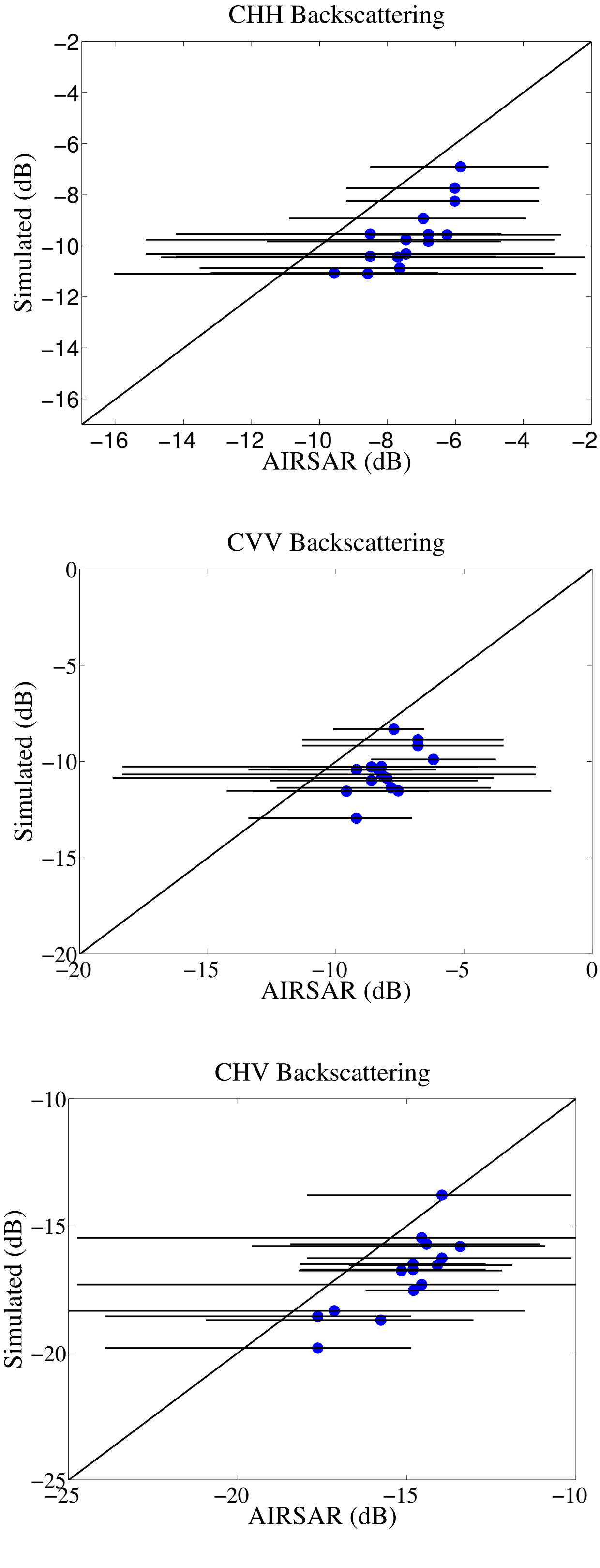

Figure 4.12: Model simulated backscattering coefficients versus AIRSAR data at C-band at HH, VV and HV polarizations.

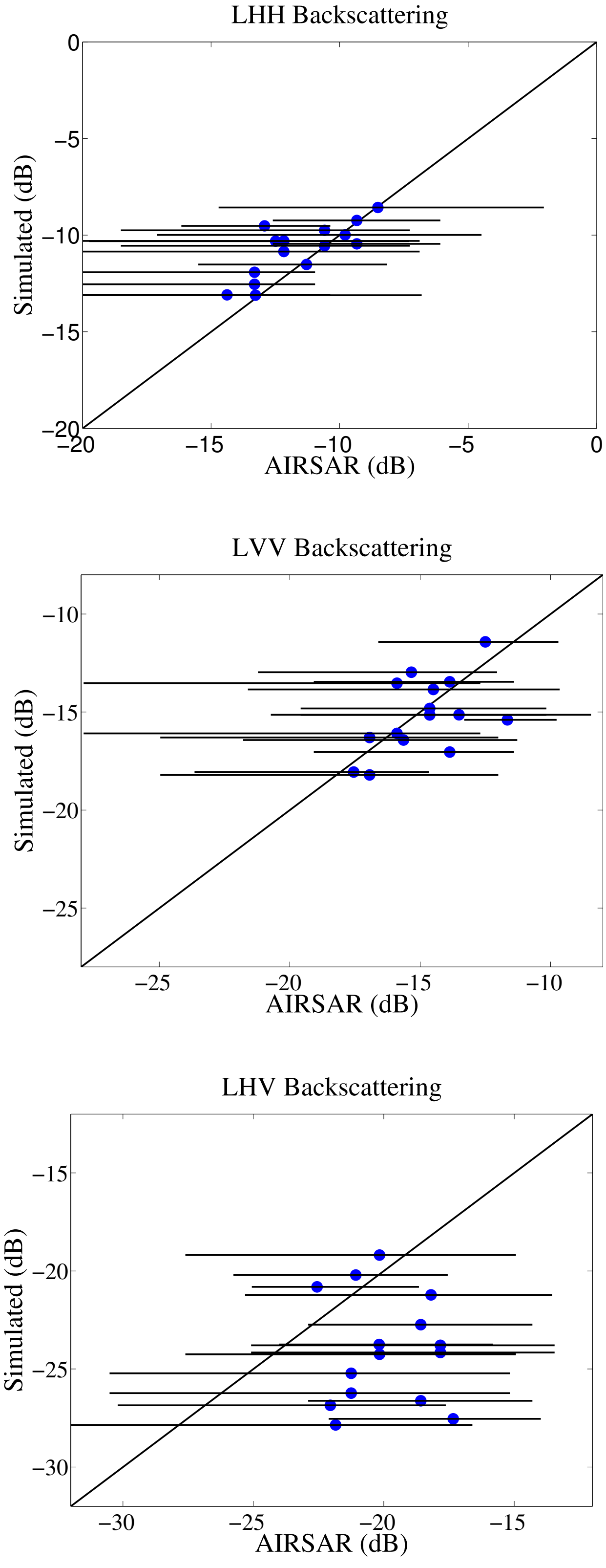

Figure 4.13: Model simulated backscattering coefficients versus AIRSAR data at L-band at HH, VV and HV polarizations.

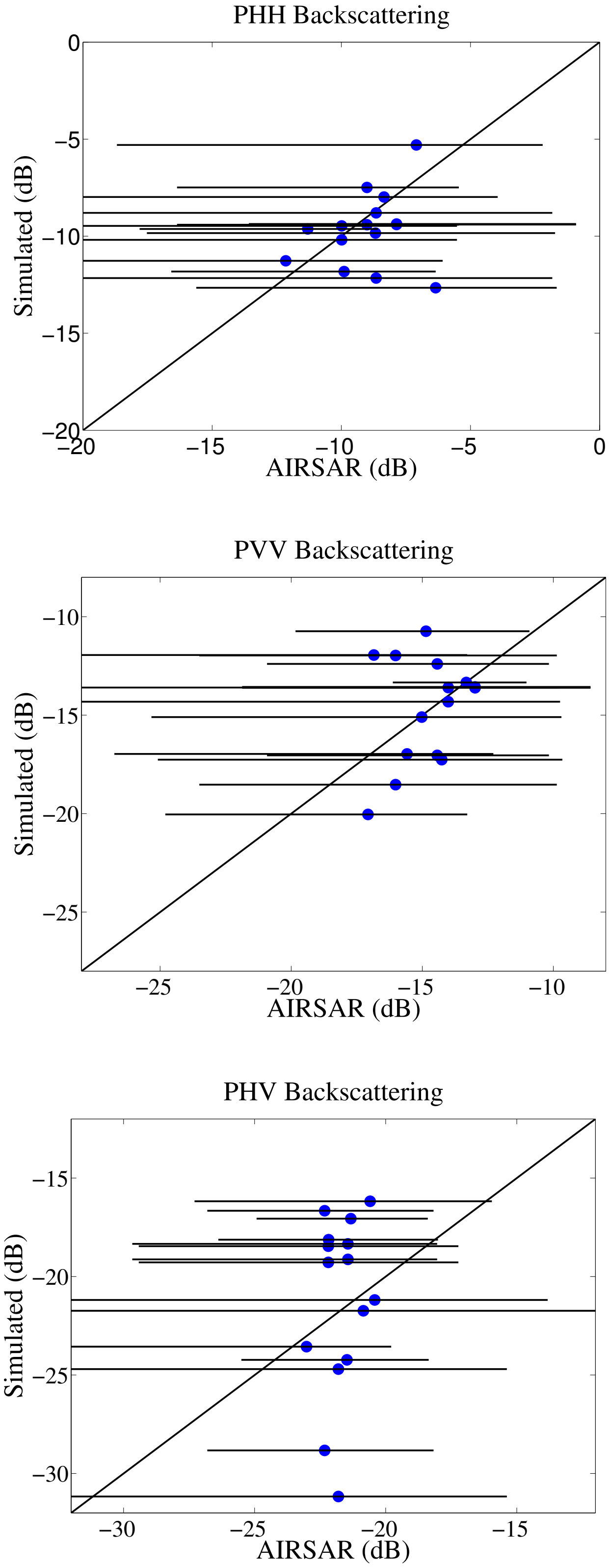

Figure 4.14: Model simulated backscattering coefficients versus AIRSAR data at P-band at HH, VV and HV polarizations.

Table 4.4: Mean Error and RMS Error Between Model Simulation and AIRSAR Measurement.

Band	HH		VV		HV	
	Mean Error	RMSE	Mean Error	RMSE	Mean Error	RMSE
C(dB)	-2.21	2.30	-2.33	2.48	-1.72	1.90
L(dB)	0.59	1.07	-0.05	1.43	-3.66	4.63
P(dB)	-0.26	1.50	-0.25	2.25	1.14	3.61

4.2.4 Scattering Mechanisms

By analyzing scattering from each layer in the canopy, the backscattering from each polarization was observed to originate from different canopy components. At C-band, the σ^0 was primarily through direct scattering from the branches and foliage and varied with small branch and foliage biomass. At C-band HH and VV, scattering from the small branches dominated while scattering from both small and also larger branches was seen to contribute to C-band HV. Trunk and ground scattering were attenuated largely by the top of the canopy.

At L-band HH, contributions from trunk and ground interactions dominated while L-band VV and HV contributions were mainly from the large branches. Ground scattering was also present but generally insignificant.

At P-band, major scattering occurred through interaction between the trunks and large branches and the ground surface. P-band VV and HV backscattering was attributed largely to interaction between the ground and the large branches and also direct large branch scattering. This was particularly noticeable within stands containing larger individuals of SBA which supported an expansive crown and allocated a significant proportion of the biomass to a network of large branches. Compared to

C-band and L-band, σ^0 from the ground surface was significantly greater because of reduced attenuation by the canopy.

4.3 Discussion

4.3.1 Performance of Multi-MIMICS

Overall, multi-MIMICS provides a more effective scattering model for simulating SAR σ^0 from forests of mixed species and structural form compared to its predecessor [86] which was effectively a two layered forest model.

The observed discrepancies between measured and simulated σ^0 can be attributed to three main factors: the error associated with field measurement and parameter derivation, the limitation of the first order RT-based model and the error associated with AIRSAR data acquisition and calibration.

First, the forests are extremely complex and hence there is necessarily some homogenization in order to achieve parameterization. Multi-MIMICS is sensitive to the dimensions, density, angular distribution and dielectric constant of the forest components and also surface attributes and any inaccuracies in these data and the derived parameters will therefore result in estimation error by the model. In this study, errors are associated with parameter estimation from a) field measurements (e.g., diameters), b) interpretation of digital photographs (e.g., branch lengths) and c) measurements from destructively harvested trees (e.g., moisture contents and canopy component densities) and also their derivation from summarized data. In all cases, the canopy was assumed to be continuous with horizontal homogeneity and that each species was distributed uniformly over each SSU. However, even within a single SSU, considerable heterogeneity in cover and species distributions occurs and gaps in the canopy are commonplace. The close correspondence between actual and simulated

σ^0 is therefore particularly encouraging.

Second, the simulations are limited by using only a first order RT-based model. Our present first order solution does not include the multiple scattering mechanism among scatterers; the coherent effects, such as enhanced backscatter, are not therefore considered. Multiple scattering among canopy elements is expected, particularly at C-band, where branch and foliage volume scattering dominates and this may be the reason for the underestimation of σ^0 at C-band. The model predictions for L-band and P-band at HV polarization are also believed to be low as the simulation does not contain multiple and higher order scattering associated with the HV polarization. Furthermore, an ideal vertical trunk model is used and HV scattering from these is not considered. However, the structure of the forests is such, particularly in those dominated by decurrent (e.g., Eucalyptus) forms, that many trunks are leaning and the crown centers are often displaced from the location of the trunk base. Overall, multi-MIMICS provides better simulations at L-band.

Finally, errors are associated with the acquisition of AIRSAR data, particularly as high winds prevailed, and also subsequent calibration. The AIRSAR data form the PACRIM II Mission are known to have a calibration accuracy of 1 dB. However, the data at C-band have larger errors. The sensitivity of P-band HV is also suspect given its insensitivity to biomass variation among the SSUs considered.

4.3.2 Scattering Behavior

The simulations using multi-MIMICS are an improvement on those undertaken using a modified version of the model of Durden *et al.* [19, 48] . The scattering mechanisms observed are also similar. As with [48], this study supports the notion that C-band HV, L-band HH and L-band HV can be integrated to estimate the leaf/small branch, trunk and branch biomass of the forests at Injune.

4.4 Conclusion

Multi-MIMICS was parameterized using plot data representing fifteen configurations of mixed species forest in Queensland, Australia, with each containing a diversity of species, structural forms and growth stages. The resulting simulations represented a considerable improvement over those generated using MIMICS with the same source data and a successful simulation of the backscattering coefficient, as indicated by the close correspondence with AIRSAR data. The model simulations were best at L-band HH and VV and also P-band HH and VV, although σ^0 at C-band and also L-band and P-band HV was underestimated. These discrepancies were attributable largely to the model inputs (as these were still homogenized representations of the complex forest), the limitations of the model and inaccuracies in the AIRSAR calibration.

The potential retrieval of forest biomass and other vegetation parameters can be studied by integrating the radar response at multiple frequencies and polarizations, and the effect of forest parameters on backscattering coefficients can be predicated by changing model's inputs. The research has nevertheless resulted in the development of a model that is applicable to a significant proportion of forests in Australia and has applications in other regions. Furthermore, the model paves the way for forest parameter estimation for forest inversion which is an aim of our ongoing work. Our future plans also include extending the current solution to higher orders.

Chapter V

CORRELATION LENGTH ESTIMATION OF SAR IMAGERY

Multi-MIMICS is a scattering model to account for the vertical inhomogeneity of nonuniform mixed forests. The output of Multi-MIMICS is the mean scattering coefficient from canopies with infinite horizontal homogeneous surface for each polarization. However, to study the horizontal inhomogeneity of the scene, single pixel value is insufficient and image texture provides the required information. In this chapter, the multiplicative SAR image model is used and a texture measurement model — correlation length is applied to SAR images, which is compared with Markov random field (MRF) method. A blind deconvolution method is also developed to estimate the target texture correlation length that is buried by the presence of speckles for SAR imagery.

5.1 Introduction to SAR Texture

The definition of texture is wide and varies among research areas. Webster's dictionary defines texture as "visual or tactile surface characteristics and appearance of something". It can be interpreted as smooth or rough, fine or coarse, irregular or lineated. Some researchers [31] define texture to be "detailed structure in an image that is too fine to be resolved, yet too coarse enough to produce a noticeable fluctuation in the gray levels of neighboring cells". Haralick in [28] characterized texture by tonal primitive properties as well as spatial relations between them. Texture is also defined as the repetition of a pattern in [45].

Texture is mainly studied by statistical and structural approaches. Statistical approaches analyze the texture as a random field modeled with some parameters. Statistical models are appropriate for disordered textures [64]. Structural approaches study the texture geometrically, some primitive elements and the relationships and placement rules of those elements are used to symbolize textures. The structural approaches are more suitable for strongly ordered textures [64].

In this dissertation, the definition of texture is the spatial distribution of gray level variation in a 2-D image. SAR data measure the complex scattering of the scene. The information of each SAR image pixel is carried by the radar cross section (RCS) or scattering coefficient. For distributed targets, the estimate of the local scattering can be presented by the coherent summation over a number of discrete scatterers illuminated by the radar beam. For a single look SAR image of a homogeneous scene, the observed in phase and quadrature components are independently identically distributed Gaussian random variables with mean zero and variance $\frac{\sigma^0}{2}$ determined by the scattering amplitude. The observed phase is uniformly distributed over $[-\pi, \pi]$. The resulting intensity has a negative exponential distribution with mean and standard deviation both equal to σ^0. The noise looking image is the result of the fading process — an intrinsic effect of all coherent imaging systems such as radar, lidar, sonar or ultrasound. How the RCS distributes as a function of position determines the overall structure in the images. However, the spatial average properties over a region is not the only source of information within a SAR image. In visualization of

SAR images, image pixel values fluctuate apparently in addition to speckle. Physically, the fluctuations correspond to scene structural variations. This type of process caused by natural clutters can be treated as a noise-like texture variable. Therefore, we define SAR texture to be the spatial fluctuation properties of the RCS in a region. Texture measures the depth of fluctuation of the RCS within the local region. A clutter sample comprised only of speckle is not considered textured. With texture information, we can better understand the characteristics of the region of interest.

Because SAR texture is not strongly ordered, the statistical approaches are applied. The usual method to extract SAR data information is to establish viable statistical models, in which information can be related to measurable parameters of targets.

5.2 Correlation Length Model of SAR Images

5.2.1 Multiplicative SAR Model

A multiplicative model of a fading random variable and a texture random variable can be used for SAR images. The fading random variable represents speckle statistics due to the coherent nature of the SAR. The texture random variable represents the intrinsic scene texture caused by the spatial variability in the scattering properties of the targets. The model for an intensity SAR image of $N_x \times N_y$ is given by [85]

$$I(i,j) = \sigma^0 T(i,j) F_N(i,j) \tag{5.1}$$

where I and σ^0 denote the image intensity (power) and mean scattering coefficient of the field of interest. T and F_N represent the random texture variable with mean $E\{T\} = 1$ and the random fading variable with mean $E\{F_N\} = 1$, respectively. N is the number of looks. An N-look intensity radar image is generated by the incoherent averaging of N uncorrelated intensity images of the same scene. The parameters $0 \leq i < N_x$ and $0 \leq j < N_y$ are the azimuth and range coordinates of a pixel.

Speckle conveys little information about a scene other than that it contains many randomly positioned scattering elements. It results from interference between many random scatterers within a resolution cell under the assumption that the cell contains a larger number of identical and independent scatterers without any single dominant scatterer. Theoretically, the sum of the backscattering electric field is equivalent to a 2-D random walk process with independently and identically Gaussian distributed real and imaginary components [25, 84]. When $N = 1$, the pdf of the single-look fading random variable follows a negative exponential distribution. It is necessary to emphasize that speckle is noise-like, but it is not noise. It is a real electromagnetic measurement produced by all coherent imaging systems. The pdf of the N-look fading random variable is represented by the average of N independent single-look fading random variables, which is a Gamma distributions of shape parameter N and scale parameter N

$$P(F_N) = \frac{N^N F_N^{N-1} e^{(-NF_N)}}{\Gamma(N)} \tag{5.2}$$

with mean $E[F_N = 1]$ and variance $Var(F_N) = \frac{1}{N}$. The properties of fading show that incoherent averaging over several images of the same area improves the interpretation of the SAR imagery.

Natural scenes are not normally homogeneous, rather, they have an intrinsic spatial variability. Discriminants based on texture measure the variation of RCS within the target region. For a homogeneous area, the texture component is considered constant $T(i, j) = 1$. The standard deviation or contrast $(\frac{\sqrt{Var(I)}}{\bar{I}})$ of the image is a parameter to test different land use categories. Research has shown that vegetation categories would belong to medium texture classes with medium contrast whereas urban would represent a high texture class for its high contrast. The more profound approach to describe texture requires second or high order statistical characteristics of images. Image correlation length is another parameter proposed [85] to represent the texture characteristics of images, and the term is commonly used for rough surface modeling.

5.2.2 Correlation Function Estimation

The image autocorrelation function is defined on the multiplicative image model. Under the assumption of stationarity and independence for $T(i,j)$ and $F_N(i,j)$, the image autocorrelation function is

$$R_I(p,q;N) = {\sigma^0}^2 R_T(p,q) R_F(p,q;N) \tag{5.3}$$

where $R_T(p,q)$ and $R_F(p,q;M)$ are the autocorrelation functions of $T(i,j)$ and $F_M(i,j)$, respectively, and (p,q) is the pixel distance. The correlation coefficient is then given by

$$\rho(p,q) = \frac{R_I(p,q) - {\sigma^0}^2}{R_I(0,0) - {\sigma^0}^2} \tag{5.4}$$

Thus, the correlation length L of the image is defined as

$$L = \sqrt{L_x^2 + L_y^2} \tag{5.5}$$

while L_x and L_y satisfy the condition

$$\rho(L_x, L_y) = e^{-1} \tag{5.6}$$

For an image of a particular land-cover category, two parameters σ^0 and L can be extracted to represent the characteristics of that category. There are two ways to calculate the correlation functions of SAR images. We can either compute it directly in the spatial domain or employ 2-D discrete Fourier transform (DFT) in the frequency domain. Under the assumption of stationarity and periodicity of the image, the autocorrelation function is calculated by

$$R_I(p,q) = \frac{1}{N_p} \sum_{i=0}^{N_x-1} \sum_{j=0}^{N_y-1} I(i,j) I(i+p, j+q) \tag{5.7}$$

with $N_p = N_x \times N_y$ is the number of the pixels within the image. The parameters $0 \leq p < N_x$ and $0 \leq q < N_y$ are the azimuth and range displacement distance.

The autocorrelation function can also be obtained by the inverse discrete Fourier transform (IDFT) of the power spectral density function of the image

$$R_I(p,q) = \mathbf{IDFT}[P(i,j)] = \mathbf{IDFT}[|\mathbf{DFT}[I(i,j)]|^2] \tag{5.8}$$

where $P(i,j)$ is the squared magnitude of the DFT of the image.

The pixels with larger distance are less correlated. As a result, the autocorrelation function attenuates as the displacement distance increases. Most times, we are only interested in a small part of the autocorrelation matrix, which is when the spatial domain direct computing approach is often chosen to save the computation of DFT/IDFT of whole image. The frequency domain approach is often used to simulate image textures.

5.2.3 Correlation Length of SAR Texture With Speckles

The presence of speckle makes the retrieval of accurate texture statistics difficult. As a result, the correlation lengths of the degraded images tend to be very small, corresponding to the correlation length of speckle. To show the speckle effect on the texture, we compare the correlation length of simulated textures and speckled textures. A simulation algorithm [13] based on the scattering modified Mueller matrix is used to generate several homogeneous polarimetric SAR images with same mean intensities and different correlation lengths representing different textures. The resulting images have Gaussian correlation functions. Next, single and two-look speckle are applied to the simulated texture images.

The term Gaussian surface denotes a surface height random process having a Gaussian correlation function [14]. Similarly, the Gaussian texture represents a texture random process having a correlation function described by

$$R(p,q) = \sigma^2 exp(-\frac{p^2+q^2}{L^2}) \tag{5.9}$$

where σ^2 is the texture variance and L is the correlation length. A 2-D DFT gives the power spectral density for a $N_x \times N_y$ Gaussian texture image.

$$P(m,n) = \sigma^2\pi^2L^2 exp\{-\pi^2L^2(\frac{m^2}{{N_x}^2}+\frac{n^2}{{N_y}^2})\} \tag{5.10}$$

where $0 \leq m \leq N_x - 1$ and $0 \leq n \leq N_y - 1$.

The texture simulation procedure can be realized by a filter $H(m,n) = \sqrt{P(m,n)}$ with an input of a complex Gaussian random process $N(0,1)$ with zero mean and unit variance in the frequency domain. The output of the filter is the squared root of the image power spectral density and texture can be obtained by the method of inverse discrete Fourier transform (IDFT). The process is illustrated in Figure 5.1.

$$N(0,1) \longrightarrow \boxed{H(m,n) = \sqrt{P(m,n)}} \longrightarrow \boxed{IDFT} \longrightarrow I(i,j)$$

Figure 5.1: Texture simulator with defined power spectral density through a complex Gaussian random process.

Five textures with correlation length ranging from 4 to 20 pixels are simulated by the above process. Each image's size is 512×512. Figure 5.2 shows the five simulated Gaussian texture images with the same mean but different correlation lengths of 4.71, 7.60, 8.94, 12.55 and 13.61, respectively. The correlation lengths used to simulate these fives images are L=5, 8, 9, 13 and 15. As can be seen from Figure 5.3, the

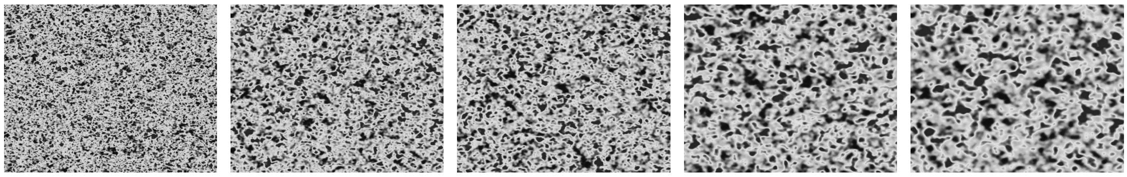

(a) $L = 4.71$ (b) $L = 7.60$ (c) $L = 8.94$ (d) $L = 12.55$ (e) $L = 13.61$

Figure 5.2: Original simulated textures with different correlation length. (Images are enhanced by histogram equalization).

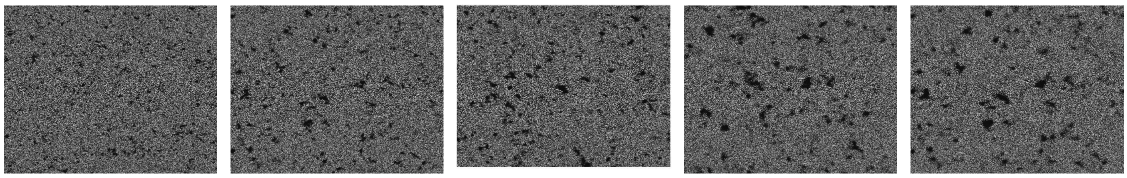

(a) $L = 0.56$ (b) $L = 0.56$ (c) $L = 0.58$ (d) $L = 0.57$ (e) $L = 0.55$

Figure 5.3: Simulated textures are corrupted by the single-look speckles, the resulting correlation lengths are similar. (Images are enhanced by histogram equalization).

texture information is buried in the noise after we corrupt the images with speckle. The correlation lengths of those single-look speckled images are found to be 0.56, 0.56, 0.58, 0.57 and 0.55, the estimation error is over 88%. The correlation lengths of two-look speckle degareded images are 0.80, 0.82, 0.86, 0.84 and 0.81. The results show that the correlation length of raw SAR images becomes meaningless. Since the corrupted images have the same mean and very similar correlation length, it is difficult to get accurate land-cover classification by these two parameters.

For the ideal situation, SAR image speckle is assumed uncorrelated among pixels, which enables us to obtain the real texture correlation functions from corrupted ones, we will show the algorithms in the next chapter. However, the limited bandwidth and sampling of SAR process system causes the real-life case to be far more complicated, the assumption dose not always hold. Some efforts have been done to derive the speckle autocorrelation function R_F, Dainty derived the single-look intensity image autocorrelation function of speckle in [11] for a square uniform aperture as

$$R_F(p, q; N = 1) = [1 + \text{sinc}^2(\frac{p}{r_x}) + \text{sinc}^2(\frac{q}{r_y})] \tag{5.11}$$

with r_x and r_y the spatial resolution of the sensor. Most times, due to the lack of system information and the comprehensive procedures that generated the images, users are provided with little knowledge of the correlation properties of speckle.

5.2.4 Other Image Texture Models

Many image texture models have been developed for various applications such as image segmentation, computer vision and medical imaging. Some among them used for SAR data are histogram estimation [37, 85] , image correlation length estimation [37, 85], second-order gray-level co-occurrence matrix (GLCM) method [28, 85], lacunarity index [17, 54, 63], wavelet decomposition [59] and Markov random field (MRF) models [12, 15, 24, 42, 75]. These methods are widely used SAR image processing techniques currently.

Image correlation length is of our interest because of its relatively easy implementation and physical understanding for remote sensing applications. MRF texture models become more popular partly due to development of larger and faster computers, which compensates the disadvantage of high computational cost. We apply MRF model and correlation length model on some SAR data from natural forests to compare the texture information extracted by both models. The results offer a tool to evaluate the effectiveness of the correlation length model.

Markov random field (MRF) models have been widely used to characterize image textures. In these models, the image pixels are described by Markov chains defined in terms of conditional probabilities associated with spatial neighborhoods. There are many MRF models that have been proposed such as Gibbs, Gaussian, binomial and Gamma [10, 15, 24, 42] models. Gaussian Markov random field model is chosen for our data characteristics since we apply the models on logarithmic intensity radar images. Detailed descriptions about these models can be fund from the references and are not the topics of this dissertation. A simple explanation of Gaussian Markov random field (GMRF) is given as follow.

Let $\{y(s)|s \in \Omega, \Omega = \{s = (i, j)\}, 0 \leq i, j \leq M - 1\}$ be the observation from an image of size $M \times M$. The 2-D noncausual GMRF follow the difference equation [10]

$$y(s) = \sum_{r \in N_s} \theta_r(y(s + r) + y(s - r)) + e(s) \tag{5.12}$$

where $e(s)$ is a white stationary Gaussian noise sequence, N_s is the asymmetric neighborhood and θ_r are the interaction coefficients. The neighborhood N_s is characterized by the model order. Figure 5.4 shows some examples for N_s at order 1,3 and 6, where the center pixel is denoted by indexes $(0, 0)$ and its neighborhood pixels are presented by the displacement of the indexes r, which can have the value such as $(0, -1)$, $(2, 0)$ and $(0, 1)$, *etc.* The order of the model is defined by the distance between the surrounding and center pixels. Higher order means larger neighborhood and more interaction coefficients are needed for the model. The first order has two neighborhood pixels and the sixth order model has fourteen The. The asymmetric neighborhood covers only half of the surrounding pixels because the model assumes the symmetry respect to the center.

The above set of equations can be rewritten in the form of a 2-D convolution $h(\theta_r) \otimes y = e$, so we can simulate a GMRF image by the techniques of DFT and IDFT [10]. The function $h(\theta_r)$ is the neighborhood interaction matrix formed by the interaction coefficients. Its size depends on the order of model (neighborhood) and

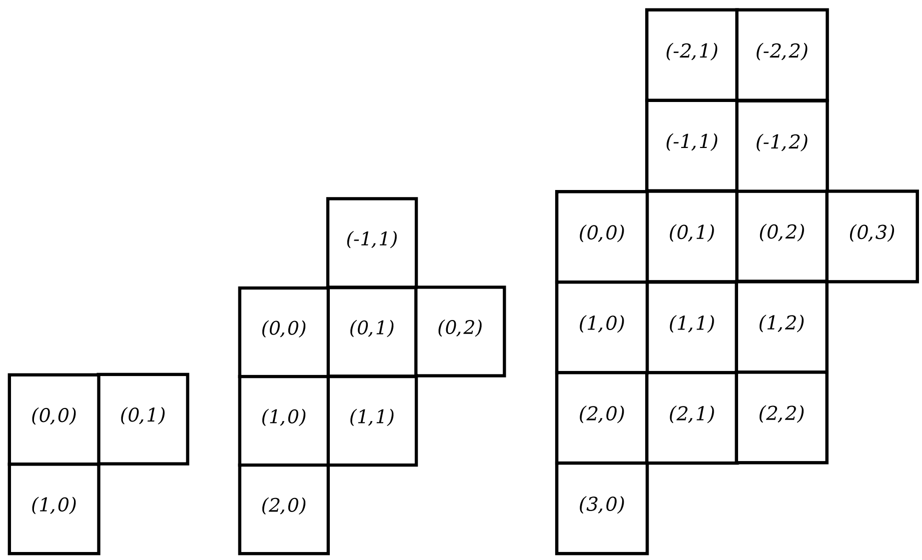

(a) Order = 1 (b) Order = 3 (c) Order = 6

Figure 5.4: Asymmetric neighborhood of Gaussian Markov random field.

can be estimated from th image. The order of neighborhood describes the extended range of the correlated pixels and the interaction coefficients decide the relationship among them.

5.3 Texture Estimation For SAR Data Of Natural Forests

5.3.1 Remote Sensing Data

Both the correlation length model and GMRF model are applied to actual SAR data to extract texture information from the image. Our test image is one JERS image from Manaus in the Amazon basin in June, 1996. The image is orthorectified to be precisely geocoded and remove the terrain effect. The calibrated backscattering coefficients are in logarithmic format ranging $-40 \sim 0$ dB. They are rescaled to $0 \sim 255$ to form a 8 bit unsigned integer channel with pixel size of $25m$. Then, a 7×7 EPOS speckle filter [27] is applied to remove the speckle. After the filtering, the image is considered to represent the real RCS of the target. Therefore, the texture

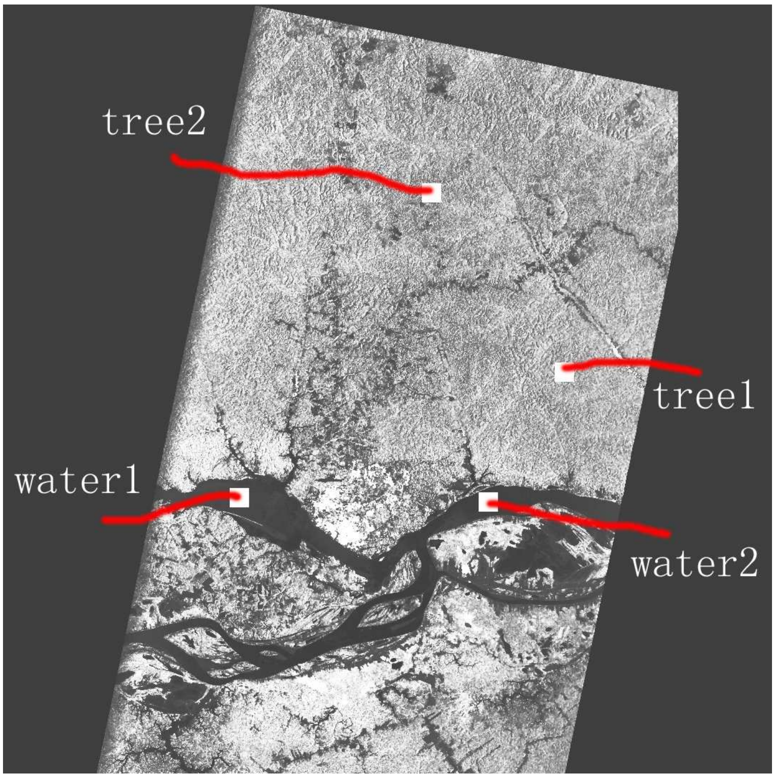

Figure 5.5: Orthorectified and filtered L-band JERS image of Manaus in the Amazon basin. Four test samples are chosen from the image: two forest area samples, tow water surface samples. Acquisition date: June, 1996. Pixel Size: 25×25 m.

information estimated below by the two models represents the true texture of the target and is free of the effects of fading.

The image is classified into the four classes: flat area (water, bare soil), short vegetation, secondary forest regrowth and primary forest. Two 128×128 water samples and 128×128 primary forest samples are randomly selected to apply texture measurement. Figure 5.5 is the orthorectified and filtered JERS image and four selected samples are indicated. The full resolution SAR image of four samples are shown in Figure 5.6. The mean pixel values for these 4 samples are 132.34 and 123.37 for two water samples, 183.50 and 182.70 for two forest samples, respectively. The images are linearly enhanced to show the spatial variations.

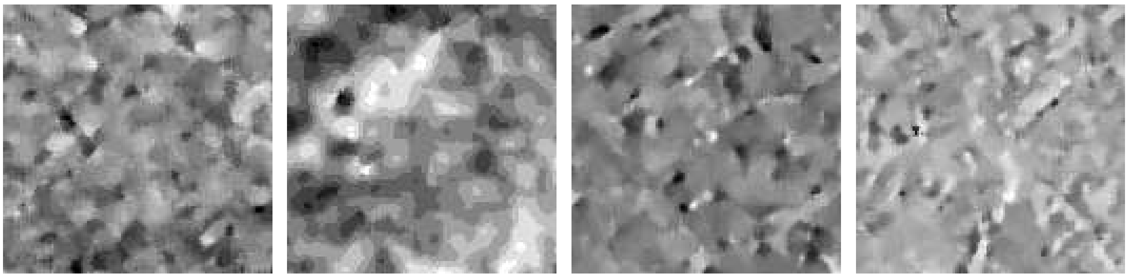

(a) Water 1 (b) Water 2 (c) Forest 1 (d) Forest 2

Figure 5.6: Full resolution SAR image of four samples. Size of each sample: 128×128 pixels.

5.3.2 Texture Estimation Result

All the calculations are applied to the logarithmic intensity image. First we calculate the correlation length of the four samples. Then we apply the least square(LS) estimation method [10] to estimate the GMRF neighborhood matrices for each sample. The orders of model's neighborhood are estimated by Bayesian selection [79].

The correlation length of the four samples are calculated as 6.91 pixels and 13.4 pixels for two water samples, 4.98 pixels and 4.79 pixels for two forest samples. The results are consistent with the target properties. We expect slow variation from the water surface, which results in longer correlation length. The forest canopy has faster spatial variation, therefore, short correlation length. The correlation coefficient for the four samples are shown in Figure 5.7.

For the GMRF model, the neighborhood orders for four samples are 6 (Water 1), 7 (Water 2), 3 (Forest 1), 3 (Forest 2) respectively. The calculated interaction coefficients within the neighborhood are listed in Table 5.1. As seen from the table, the interaction coefficients of all sample images have large values for two closet neighboring pixels — the bottom neighbor $(1, 0)$ and right neighbor $(0, 1)$, the interaction coefficients at other locations have much less weights on the center pixel.

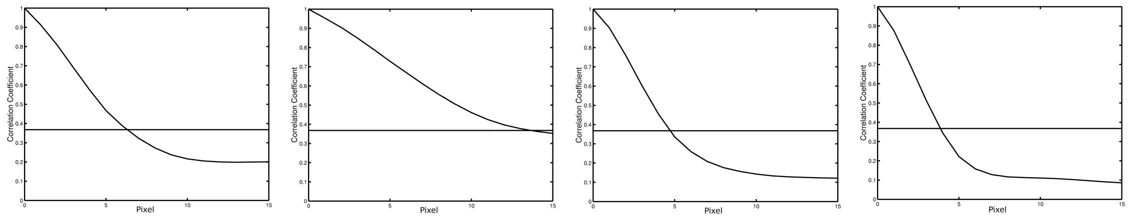

(a) Water 1, $L = 6.91$ (b) Water 2, $L = 13.4$ (c) Forest 1, $L = 4.98$ (d) Forest 2, $L = 4.79$

Figure 5.7: Correlation coefficient of four JERS image samples.

These results indicate pixels have more influences on the pixels nearby than pixes far away.

The estimated correlation length and GMRF model order of two models are closely related since images with higher GMRF model order have longer correlation lengths, as shown in Table 5.2. Relationships among different texture models are useful for model selection and verification. Parameters estimated by two models deliver similar information about the image's spatial variation. However, the implementation of correlation length model is proved to be easier and faster and yet effective compared to much more complicated GMRF model. This is the reason we choose the correlation length model as the texture measurement for SAR images.

In this example, the different correlation lengths can distinguish the classes of water and forests. Texture measurements of different land coverage categories such as short vegetation, regrowth forests, and mature forests help us better understand the forest distribution on the ground and improve the retrieval of the forest structure parameters such as biomass and tree height. In this section, both texture models are applied to filtered SAR images, which is the usual approach in SAR image processing. However, we are also interested in estimating image texture before despeckle to investigate the effect of speckle on the target texture, since many speckle filters

Table 5.1: GMRF neighborhood interaction coefficients for four JERS image samples.

	Water 1	Water 2	Forest 1	Forest 2
$\theta(1,0)$	0.3337	0.2632	0.3765	0.4069
$\theta(0,1)$	0.3394	0.3054	0.3706	0.3811
$\theta(-1,1)$	-0.0489	-0.0059	-0.0813	-0.1018
$\theta(1,1)$	-0.0692	-0.0294	-0.1196	-0.1337
$\theta(2,0)$	0.0558	0.0454	-0.0199	-0.0232
$\theta(0,2)$	0.0479	0.0458	-0.0175	-0.0224
$\theta(-2,1)$	-0.0489	-0.0289		
$\theta(2,1)$	-0.0339	-0.0300		
$\theta(-1,2)$	-0.0436	-0.0257		
$\theta(1,2)$	-0.0415	-0.0288		
$\theta(-2,2)$	0.0133	0.0080		
$\theta(2,2)$	0.0071	0.0059		
$\theta(3,0)$	-0.0063	0.0413		
$\theta(0,3)$	-0.0026	0.0627		
$\theta(-1,3)$		-0.0422		
$\theta(1,3)$		-0.0377		
$\theta(-3,1)$		-0.0285		
$\theta(3,1)$		-0.0201		

inevitably change or add artifacts to SAR images and distort the real target texture.

5.4 Correlation Length of SAR Imagery Through Blind Deconvolution

5.4.1 Algorithm Overview

Over the years, many speckle filters have been developed with the attempt to remove the effects of speckle and still preserve the intrinsic texture information of SAR imagery. Lee [41], Kuan [35], EPOS [27] and Frost [23] filters are among the best

Table 5.2: Comparison between correlation length and GMRF order of four JERS image samples.

	Water 1	Water 2	Forest 1	Forest 2
Correlation length	6.91	13.4	4.98	4.79
GMRF order	6	7	3	3

knowns. Speckle reduction has been a prerequisite procedure for most subsequent SAR image processing. In this section, We present a blind deconvolution approach to retrieval of accurate texture correlation function from speckled SAR images without the prerequisite filtering process. The motivation of using blind deconvolution in our study is the fact that it is impossible to obtain the accurate information about the fading random process due to the complicated SAR signal processing system, which is a key factor to achieve good performance of most speckle filters.

The inspiration for us to utilize blind deconvolution method is the form of the image correlation function. A convolution model in the frequency domain can be obtained from the multiplicative model in the space domain by taking the DFT of both sides of Equation (5.3)

$$P_I(m,n) = {\sigma^0}^2 P_T(m,n) * P_F(m,n) \tag{5.13}$$

where $P_I(m,n)$, $P_T(m,n)$ and $P_F(m,n)$ are the discrete Fourier transform of the autocorrelation functions $R_I(p,q)$, $R_T(p,q)$ and $R_F(p,q)$, respectively. If we had access to the actual $P_T(m,n)$ and $P_F(m,n)$ in the frequency domain, the autocorrelation functions $R_T(p,q)$ and $R_F(p,q)$ can be obtained by the inverse discrete Fourier transform (IDFT). Therefore, the correlation length of the image can be estimated by Equation 5.6.

Since little is known about $R_F(p,q)$ and $R_T(p,q)$, a blind deconvolution approach is appropriate. The method of blind deconvolution has been used in image restoration when the blur function is not known. The general blind deconvolution problem refers to the task of separating two convolved signals (P_T and P_F in our case) when both the signals are either unknown or partially known. Image deconvolution is based on the assumption that an original image is degraded by a point spread function (PSF). The various approaches that have appeared in the literature depend upon the particular degradation and image models. Existing algorithms include projection-based blind deconvolution, maximum likelihood estimation, zero sheet separation, ARMA parameter estimation method, invariant parameter approach, gradient algorithms and increment Wiener filter [21, 36, 39, 57]. Yagle *et al* presented a blind deconvolution algorithm for even PSFs from compact support images in [88], which smartly utilizes the symmetry of the Toeplitz matrix of the convolution by a even PSF function to achieve high accuracy, however, we assume both $R_F(p,q)$ and $R_T(p,q)$ are even functions, which causes the matrices in the algorithm become singular and no meaningful solutions to our problem.

So among all the algorithms mentioned above, a method of gradient-based nonlinear optimization [57] is chosen in our study. This is one kind of least squares and iterative (LSI) algorithm. Its aperiodic model is generally nonsingular. The main calculation in the algorithm can be accomplished efficiently by means of DFT technique. The algorithm is described in [57]. We make some adjustments to adapt it for use with SAR images.

5.4.2 Blind Deconvolution Algorithm

According to [57], the model of the convolution process is

$$x * h = y \tag{5.14}$$

where x is the original image with dimension $M_1 \times N_1$, h is the PSF(point spread function) of $M_2 \times N_2$, y is the degraded image with dimension $(M_1 + M_2 - 1) \times (N_1 + N_2 - 1)$. The deconvolution of the aperiodic model has the form

$$\mathbf{F_h x} = \mathbf{y} \tag{5.15}$$

where $\mathbf{x}$ is of $M_1N_1 \times 1$, $\mathbf{h}$ is of $M_2N_2 \times 1$, and $\mathbf{y}$ is of $L \times 1$ with $L = (M_1 + M_2 - 1)(N_1 + N_2 - 1)$. $\mathbf{F_h}$ is the kernel matrix formed from h, the least-square solution to the above equation is given by

$$(\mathbf{F_h^T F_h})\mathbf{x} = \mathbf{F_h^T y} \tag{5.16}$$

where $\mathbf{F_h^T F_h}$ is a block Toeplitz matrix.

In terms of aperiodic model $\mathbf{s} = \mathbf{y} - \mathbf{F_h x}$, the nonlinear optimization method is to estimate a pair of x and h that minimize the difference $s(m, n) = y(m, n) - x(m, n) * y(m, n)$.

Let $\theta^T = [\mathbf{x}^T \mathbf{h}^T]$, the error metric is defined by

$$E = \frac{1}{2}[\lambda \|\mathbf{s}\|^2 + (1 - \lambda)\|\theta\|^2] \tag{5.17}$$

with $0 < \lambda < 1$. We hope to find $\theta_1 = \theta + \delta\theta$ so that the error metric can be reduced. [57] gives the shortest least-squares solution

$$\Delta E \approx \Delta\theta^T \mathbf{g}_1 + \frac{1}{2}\mathbf{H}\Delta\theta \tag{5.18}$$

where the gradient vector and the Hessian matrix are

$$\mathbf{g}_1 = -\lambda \mathbf{F}^T \mathbf{s} + (1 - \lambda)\theta \tag{5.19}$$

$$\mathbf{H}_1 = \lambda \mathbf{F}^T \mathbf{F} + (1 - \lambda)\mathbf{I} \tag{5.20}$$

with $\mathbf{F} = [\mathbf{F_h F_x}]$.

The minimization of E turns out to solve the Gauss-Newton equation

$$\mathbf{H}\Delta\theta = -\mathbf{g}_1 \tag{5.21}$$

The problem can be solved efficiently by means of the DFT technique.

In our problem, the power spectral density function of texture P_T is x and the power spectral density function of speckle P_F is h, and the power spectral density function of speckled SAR image P_I is y. The algorithm begins with an initial guess P_{F_0} and then iteratively uses estimates in the frequency domain and constraints in the object domain to search for P_T and P_F alternately to minimize the object domain error metric $|P_I - \mu^2 P_T * P_F|$. We need to estimate the autocorrelation function from the speckled SAR image and the window size is chosen at least twice the texture correlation length. Because of the DFT technique, we have to assume that the image and the correlation functions are periodic.

5.4.3 Simulation Result

The blind deconvolution algorithm is then applied to the corrupted images shown in Section 5.2.3 to estimate the real correlation lengths of the textures. The results are compared with those of the original images and the corrupted images.

Speckle filters can also remove the speckle and preserve the texture [87]. Usually, speckle filtering is a window operation on each pixel of the image. The filters are based on the multiplicative speckle model, their goal is to smooth the speckle and at the same time, preserve edges and texture information. The output value of each pixel is a weighted sum of the observed pixel value and mean value within the operating window. Many speckle filters have been developed for speckle reduction, the most often used are Frost [23], EPOS [27], Lee [41] and Kuan [35] filters. It works well if the *prior* information of the speckle such as the number of looks and/or the standard deviation of the noise are known. Moreover, the performance of speckle filters is sensitive to the size of the window. We apply the Lee filter and Average Filter to the same images and compare the results with those of the blind deconvolution method. For single-look images, Table 5.3 shows that better results are obtained with the blind deconvolution method. The maximum estimation error is 19.8% by blind deconvolution, 26.58% by Lee filtering and 28.42% by average filtering. The results of two-look images in Table 2.2 show the similar performance.

Table 5.3: Comparison of the correlation length estimated by blind deconvolution and Lee, AV Filter, nlook=1.

	Correlation Length (pixel) and Estimation Error							
	Original	Corrupted	Deconvolution		Lee Filtering		AV Filtering	
		nlook=1	L	Error	L	Error	L	Error
Image1	4.71	0.56	4.59	2.55%	5.13	8.92%	5.22	10.83%
Image2	7.60	0.56	6.25	17.76%	9.62	26.58%	9.76	28.42%
Image3	8.94	0.58	7.17	19.80%	10.74	20.13%	10.94	22.37%
Image4	12.55	0.57	11.35	9.56%	15.57	24.06%	15.56	23.98%
Image5	13.61	0.55	12.05	11.46%	16.01	16.68%	16.00	17.56%

Table 5.4: Comparison of the correlation length estimated by blind deconvolution and Lee, AV Filter, nlook=2.

	Correlation Length (pixel) and Estimation Error							
	Original	Corrupted	Deconvolution		Lee Filtering		AV Filtering	
		nlook=2	L	Error	L	Error	L	Error
Image1	4.71	0.80	4.83	2.55%	5.43	15.29%	5.63	19.53%
Image2	7.60	0.82	6.82	10.26%	9.61	26.45%	9.98	31.32%
Image3	8.94	0.86	8.25	7.72%	11.00	23.04%	11.44	27.96%
Image4	12.55	0.84	12.05	3.98%	15.57	24.06%	15.56	23.98%
Image5	13.61	0.81	12.88	5.36%	16.01	16.68%	16.00	17.56%

Since mean value of all the images are round 128, correlation length is the parameters that can distinguish all the categories. It is noteworthy that the blind deconvolution have better results for two-look images than single-look images since the level of noise is considered lower. However, the Lee filter and average filter's estimates don't show much improvement for the two-look images.

For all cases, the blind deconvolution method provides more accurate correlation length estimation than Lee and average filters, but window size of the blind deconvolution is usually larger than average speckle filters, which decrease the speed for the algorithm when we incorporate it into an automatic classification program, especially when the image is large.

5.5 Conclusion

The multiplicative SAR image model is reviewed and image correlation length is the measurement we choose to study SAR texture of forest areas. A correlation length model and Gaussian Markov random field model are both applied to JERS images of natural scenes. The texture parameters of the two models are close related, which shows the similarity between different texture models. The correlation length models is preferred for easy and fast implementation. A blind deconvolution algorithm is also developed to extract the autocorrelation function of scene texture from speckle degraded images, which is alternative approach as many SAR processing techniques since speckle filtering is not performed at first and the results is satisfying. Applying this algorithm to real SAR images to estimate texture information as additional criteria to the single pixel image model to improve the classification accuracy is our goal.

Chapter VI

COHERENT SAR TEXTURE SIMULATOR

6.1 Introduction

In this chapter, a coherent SAR texture simulator is developed to simulate the backscattering of natural scenes with intrinsic texture. The coherent SAR texture simulator uses the fundamental scattering theory, it coherently adds up the backscattering from individual scatterers and the phase of the returned signal is preserved. Speckle is produced as the deterministic result of the interference. The major shortcoming of coherent simulator is the heavy task in computing the backscattering signal of many scatterers.

There have been several SAR simulators in the literature since the last decade. Most of them generate SAR images by means of statistical models. Speckle is introduced by an independent statistical noise model. MSIS [4] is a high fidelity backscattering SAR image simulator using coherent approach , the author presents a speed-up method for low resolution image simulations. Although the model is still in its initial stage, it has been used in the application to test a tree height estimation algorithm.

Instead of using some statistical model where speckle is an intrinsic product of the coherent processing algorithm. We choose the coherent simulator because the coherent approach can reliably capture the scattering signal variation caused by the space distribution of individual scatterers. It is also our intention to investigate the speckle effects on scene image texture. The simulated image is sensitive to the heterogeneous land coverage. It can fully take advantage of the 3-D forest model, in contrast to the single result for the average scattering from the canopy generated by Multi-MIMICS, a 2-D radar image texture will carry the canopy's heterogeneity.

In this chapter, the coherent simulator is practically used to study SAR texture model through its formation and the correlation length model for ideal SAR images is derived. The speckle generate by the coherent SAR texture simulator is also compared with the statistical speckle model.

6.2 SAR Texture Analysis

6.2.1 Formation of SAR Texture

In this section, we analyze the formation of SAR texture.

For simplicity, an ideal SAR system is used. The backscattering field is specified by the scattering properties of single scatterers and their relative positions. The scattered far field E_s of a pixel cell is the summation of the returned signals from all the scatterers contributing to the cell.

$$E_s = \sum_{n=1}^{N} S_n \exp(j\phi_n) W_n = \sum_{n=1}^{N} S_n \exp(j2k_0R_n) W_n \tag{6.1}$$

where N is the number of scatterers, S_n is the backscattering coefficients of the scatterer n, and $\phi_n = 2k_0R_n$ is the phase delay caused by the round trip between the antenna and the scatterer. k_0 is the free space wave number and W_n accounts for all the other factors such as antenna pattern, far range, near range, *etc.* For distributed targets, the above summation over single scatterers can be replaced by the integration over the area.

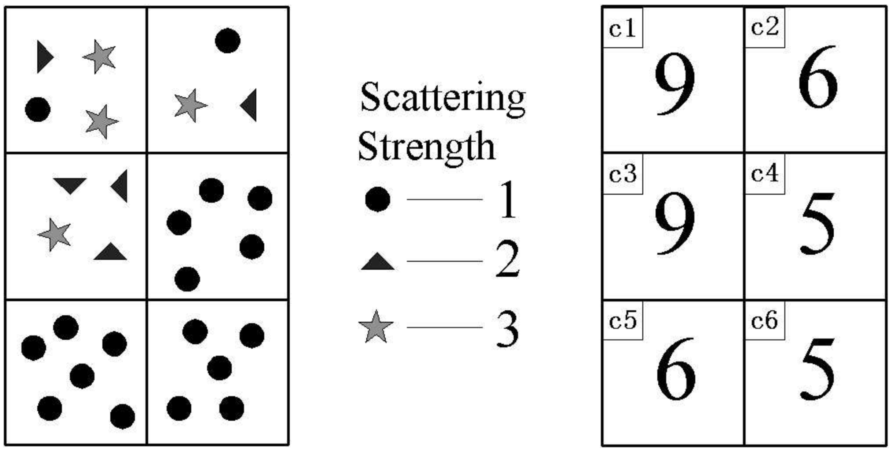

(a) Scatterers in the resolution cells

(b) Normalized scattering coefficient

(c) Normalized image

Figure 6.1: Image of textured target generated by direct summation without phase modulation

To investigate the image texture properties, we assume the W_n is corrected to be the same for all N scatterers. Therefore, only two parts S_n and ϕ_n cause the variation of the returned signal.

6.2.1.1 Target Texture

Real target texture is the variation caused by the scatterers' backscattering coefficients, of course we cannot get any variation that is smaller than a resolution cell. The backscattering scalar electrical field can be rewritten if we ignore the phase modulation.

$$E_s{}^{normalized} = \sum_{n=1}^{N} S_n{}^{normalized} \tag{6.2}$$

As illustrated in Figure 6.1(a), the target has six resolution cells enclosing three types of scatterers. The scatterers normalized backscattering coefficients are given in Figure 6.1(b) and the simulated image is shown in 6.1(c). In this example, it is impossible to tell the type and number of scatterers in each cell. However, we can tell the backscattering of *cell* 1 is stronger that of *cell* 4. This variation is the real texture information we are interested in, which is referred as the target texture.

6.2.1.2 Noise-like Speckle

Phase delay difference is caused by the range difference between the scatterers and the antenna, this consequently, generates fading or speckle. Usually, the real scene texture is buried in the noise-like speckle. It makes it difficult to identify the real texture. The speckle filter works well only if we understand the speckle. In order to characterize speckle, we assume only one type of scatterer (S_n=constant=S_0) present in our target, Equation (6.1) for the backscattering field is reduced to

$$\begin{aligned} E_s &= \sum_{n=1}^{N} S_n \exp(j2k_0R_n) = NS_0 \sum_{n=1}^{N} \frac{\cos(2k_0R_n) + j\sin(2k_0R_n)}{N} \\ &= N \times S_0 \times (Re^{(N)} + jIm^{(N)}) = N \times F^{(N)} \end{aligned} \tag{6.3}$$

where $F^{(N)} = Re^{(N)} + jIm^{(N)}$ represents the single-look fading caused by N random distributed scatterers in a resolution cell.

A natural area-extensive target is usually treated as many randomly distributed scatterers. The reasonable assumption is that the phase delay is uniformly distributed in $0 \sim 2\pi$, this is also verified by dozens of simulations. We have the distribution of the phase as

$$p(\phi) = \frac{1}{2\pi} \quad ; \quad 0 \leq \phi < 2\pi \tag{6.4}$$

Given S_0=1 and $N = 1$, according to Equations (6.3) and (6.4), the real part (Re) and the imaginary part (Im) part of single-look fading $F^{(1)}$ from a scatterer should follow the pdfs as bellow and the amplitude is 1 with the probability of 1.

$$\begin{aligned} p(Re^{(1)}) &= \frac{1}{\pi\sqrt{1 - {Re^{(1)}}^2}} \qquad -1 \leq Re^{(1)} \leq 1 \\ p(Im^{(1)}) &= \frac{1}{\pi\sqrt{1 - {Im^{(1)}}^2}} \qquad -1 \leq Im^{(1)} \leq 1 \\ P(Amp^{(1)} = 1) &= 1 \end{aligned} \tag{6.5}$$

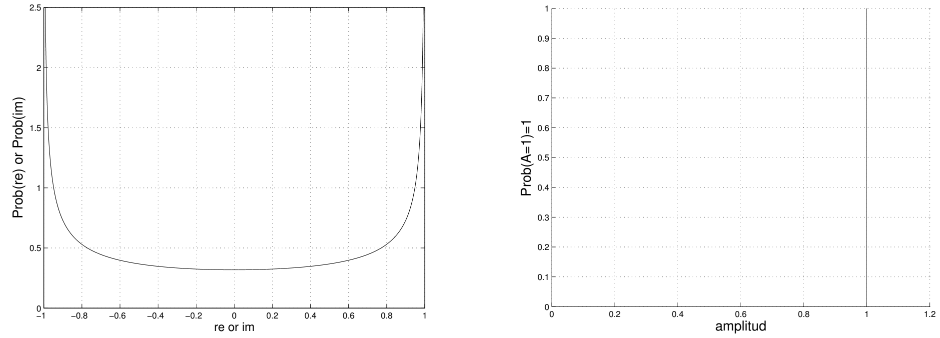

(a) pdf of real(imaginary) (b) pdf of amplitude

Figure 6.2: Probability density function of SAR backscattering electric field signal from one scatterer.

Figure 6.2 shows the distribution of the backscatter signal with only one scatterer randomly positioned in a resolution cell. We also know $E[Re^{(1)}] = E[Im^{(1)}] = 0$ and $Var[Re^{(1)}] = Var[Im^{(1)}] = \frac{1}{2}$ from Equation (6.5). When N=2, under the assumption of the interdependency of the two scatterers, the pdf of the sum of two independent variables is the convolution of the pdfs of each random variable, therefore, the pdfs of real and imaginary parts and the amplitude of the response $F^{(2)}$ are given by Equation (6.6) and plotted in Figure 6.3. In addition, $E[Re^{(2)}] = E[Im^{(2)}] = 0$ and $Var[Re^{(2)}] = Var[Im^{(2)}] = \frac{1}{2\times 2}$.

$$
\begin{aligned}
p(Re^{(2)}) &= \int_{-0.5}^{Re^{(2)}+0.5} \frac{4d\tau}{\pi^2\sqrt{1-4\tau^2}\sqrt{1-4(Re^{(2)}-\tau)^2}} && -1 \le Re^{(2)} \le 1 \\
p(Im^{(2)}) &= \int_{-0.5}^{Im^{(2)}+0.5} \frac{4d\tau}{\pi^2\sqrt{1-4\tau^2}\sqrt{1-4(Im^{(2)}-\tau)^2}} && -1 \le Im^{(2)} \le 1 \\
p(Amp^{(2)}) &= \frac{2}{\pi\sqrt{1-{Amp^{(2)}}^2}} && 0 \le Amp^{(2)} \le 1 \quad (6.6)
\end{aligned}
$$

As the number of the scatterers N increases, $N-1$ convolution operations of the pdf of real and imaginary backscattering fields by a single scatterer are needed. The properties $E[Re^{(N)}] = E[Im^{(N)}] = 0$ and $Var[Re^{(N)}] = Var[Im^{(N)}] = \frac{1}{2N}$ still hold.

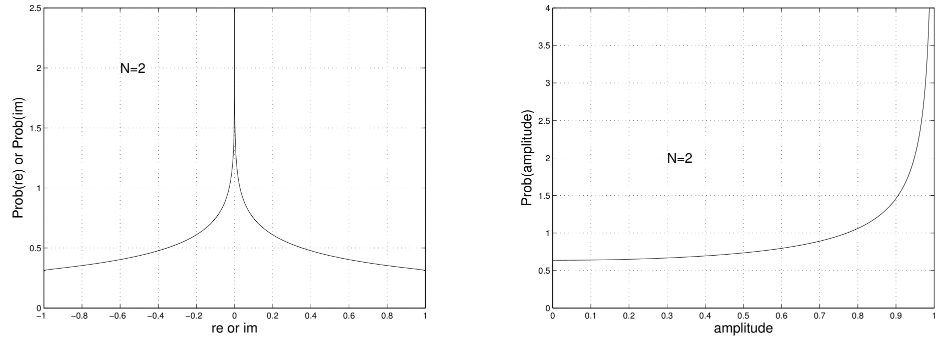

(a) pdf of real(imaginary) (b) pdf of amplitude

Figure 6.3: Probability density function of SAR backscattering electric field signal from two independent identical scatterers.

For big N, the real ($Re^{(N)}$) and imaginary ($Im^{(N)}$) parts become independent and approximately follow Gaussian distributions $norm(0, \frac{1}{2N})$. We can see the trend in Figure 6.4. The pdf of the real and imaginary parts of the fading $F^{(N)}$ for large N can be written as

$$\begin{aligned} p(Re^{(N)}) &= \sqrt{\frac{N}{\pi}} \exp(-N\, {Re^{(N)}}^2) \quad -\infty \le Re^{(N)} \le \infty \\ p(Im^{(N)}) &= \sqrt{\frac{N}{\pi}} \exp(-N\, {Im^{(N)}}^2) \quad -\infty \le Im^{(N)} \le \infty \end{aligned} \tag{6.7}$$

As a result, the fading ($F^{(N)}$) amplitude ($Amp^{(N)}$) follows the Rayleigh distribution and the intensity ($Int^{(N)}$) follows an exponential distribution.

$$\begin{aligned} p(Amp^{(N)}) &= 2N\, Amp^{(N)} \exp(-N\, {Amp^{(N)}}^2) \quad 0 \le Amp^{(N)} \le \infty \\ p(Int^{(N)}) &= N \exp(-N\, Int^{(N)}) \qquad\qquad\qquad 0 \le Int^{(N)} \le \infty \end{aligned} \tag{6.8}$$

As seen from Figure 6.4, if more than six randomly distributed single scatterers contribute to one pixel, the received signal behaves as speckle.

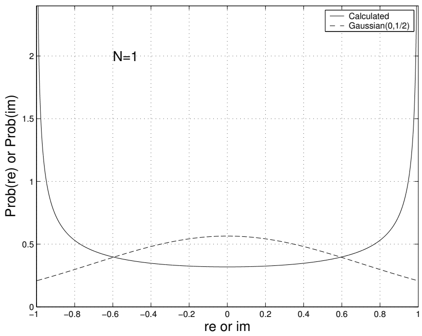

(a) N=1

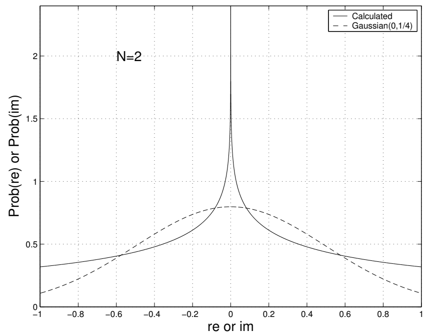

(b) N=2

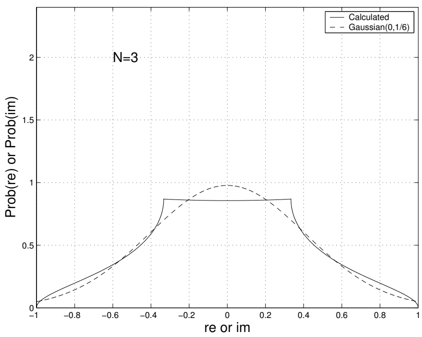

(c) N=3

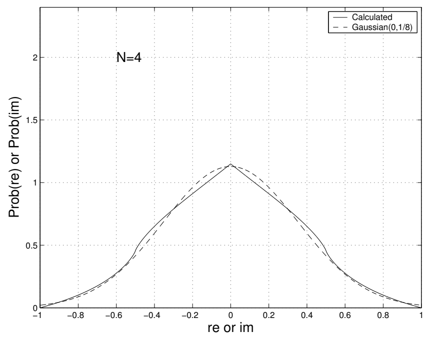

(d) N=4

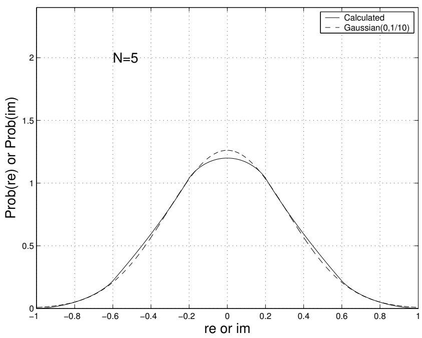

(e) N=5

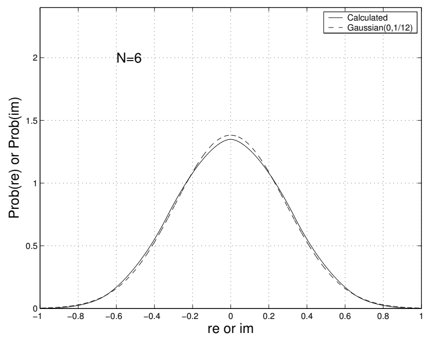

(f) N=6

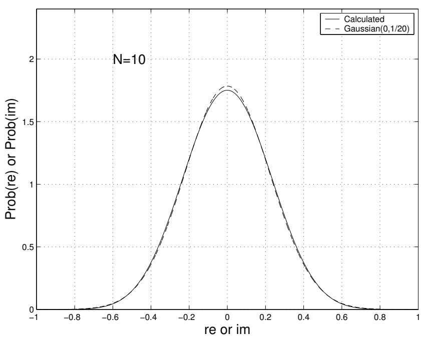

(g) N=10

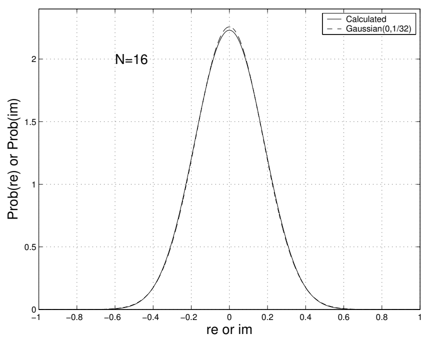

(h) N=16

Figure 6.4: Distributions of the real and imaginary SAR backscattering electric field from N randomly distributed scatterers

6.2.2 Texture of Speckled Image

From the analysis above, the received SAR image of a homogeneous scene comprising randomly distributed scatterers is pure speckle. When the target texture exists, the resulting image is a speckle corrupted version of the true texture. Assume we have only one type of scatterer and their positions on the ground follow some pattern (texture). The target texture is represented by a stationary random process $N(i,j)$ with known texture characteristics such as the autocorrelation function $R_T(\tau_i, \tau_j)$. The fading is another random process $Spkl(i,j)$. The backscattering image can be described as

$$B_{Re}(i,j) = N(i,j) \times Spkl_{Re}(i,j) \quad B_{Im}(i,j) = N(i,j) \times Spkl_{Im}(i,j)$$
$$B_{Amp}(i,j) = N(I,J) \times Spkl_{Amp}(i,j) \quad B_{Ints}(i,j) = N^2(i,j) \times Spkl_{Ints}(i,j) \quad (6.9)$$

where i and j are the pixel indexes and B denotes the backscattering image. $N(i,j)$ can be described by the number of scatterers enclosed in the resolution cell (i,j). $Spkl(i,j)$ is the disturbing factor cause by the coherent summation of random phases of scatterers. Next, we focus the analysis on the amplitude image, however, the approaches are similar for other components. From now on, the subscript *amp* is dropped.

As derived in the previous section, at a position (i,j), the value of $Spkl(i,j)$ is a random variable x with a pdf of $2N(i,j)x\exp(-N(i,j)x^2)$, therefore, strictly speaking, the texture and speckle are not uncorrelated. Another assumption is made that the speckle behaves like white noise or the correlation length for speckle is zero. This assumption is valid for the ideal SAR system because one scatterer can only contribute to on resolution cell.

Consider a periodic stationary image of size $M_1 \times M_2$, the autocorrelation function of the scene is

$$\begin{aligned}
R_B(\tau_i, \tau_j) &= \int B_1 B_2 \mathrm{d}P(B_1, B_2, (\tau_i, \tau_j)) \\
&= \int N_1 Spkl_1 \cdot N_2 Spkl_2 \cdot \mathrm{d}P(N_1 Spkl_1, N_2 Spkl_2, (\tau_i, \tau_j)) \qquad (6.10) \\
&= \frac{1}{M_1 M_2} \sum_{i=0}^{M_1-1} \sum_{j=0}^{M_2-1} N(i,j) Spkl(i,j) N(i+\tau_i, j+\tau_j) Spkl(i+\tau_i, j+\tau_j)
\end{aligned}$$

where B is the returned amplitude image and $N(i,j)$ is the number of scatterers belonging to pixel (i,j). (τ_i, τ_j) is the displacement distance between the pixels. In Equation (6.10), the ensemble average over probabilities is equalized with the average over space. Under the assumption that the speckle behaves like white noise for the ideal SAR system, we have

$$R_{Spkl}(i_1, j_1, i_2, j_2) = E[Spkl^2] \times \delta(i_2 - i_1, j_2 - j_1) \qquad (6.11)$$

Equation (6.9) shows that at a position (i,j), the value of the backscattered amplitude is a random variable whose pdf can be written as

$$p(B) = p(N) \times p(Spkl|N) \qquad (6.12)$$

where the pdf of target's scatterer distribution $p(N)$ is unknown but $p(Spkl|N)$ is already derived. The statistics are given again by

$$\begin{aligned}
p(Spkl|N) &= 2NSpkl \exp(-NSpkl^2) \qquad Spkl \geq 0 \\
E[Spkl|N] &= \frac{1}{2}\sqrt{\frac{\pi}{N}} \qquad Var[Spkl|N] = \frac{4-\pi}{4N} \\
E[(Spkl|N)^2] &= \frac{1}{N} \qquad E[(Spkl|N)^4] = \frac{2}{N^2} \qquad (6.13)
\end{aligned}$$

Take the above quantities into Equation (6.10), the mean backscattering amplitude of the image is a function of the scatterer's distribution over the scene

$$\begin{aligned}
E[B] &= \int Bp(B)\mathrm{d}B = \int N \cdot (\int Spkl \cdot p(Spkl|N) \cdot \mathrm{d}Spkl) \cdot p(N)\mathrm{d}N \\
&= \int N \cdot \frac{1}{2}\sqrt{\frac{\pi}{N}} \cdot p(N)\mathrm{d}N = \frac{\sqrt{\pi}}{2} E[\sqrt{N}] \qquad (6.14)
\end{aligned}$$

Similarly, the mean backscattering intensity of the image is

$$\begin{aligned} E[B^2] &= \int B^2 p(B)\mathrm{d}B = \int N^2 \cdot (\int Spkl^2 \cdot p(Spkl|N) \cdot \mathrm{d}Spkl) \cdot p(N)\mathrm{d}N \\ &= \int N^2 \cdot \frac{1}{N} p(N)\mathrm{d}N = E[N] \qquad (6.15) \end{aligned}$$

Equation (6.15) shows that the average over the intensity image ($intensity = amplitude^2$) is the average scatterer density (# per resolution cell) of the scene (normalized by the scattering coefficient). Moreover

$$\begin{aligned} E[B^4] &= \int B^4 p(B)\mathrm{d}B = \int N^4 \cdot (\int Spkl^4 \cdot p(Spkl|N) \cdot \mathrm{d}Spkl) \cdot p(N)\mathrm{d}N \\ &= \int N^4 \cdot \frac{2}{N^2} p(N)\mathrm{d}N = 2E[N^2] \qquad (6.16) \end{aligned}$$

Now, the autocorrelation function of the target scatterer density (# per resolution cell) is introduced as the texture measurement of the target

$$E[N_1, N_2, \tau] = \int\int N_1 N_2 p(N_1, N_2, \tau)\mathrm{d}N_1 \mathrm{d}N_2 = R^{(N)}(\tau) = \begin{cases} E[N^2] & \tau = 0 \\ R^{(N)}(\tau) & \tau \neq 0 \end{cases} \qquad (6.17)$$

where $\tau = (i_2 - i_1, j_2 - j_1)$ is the space lag of two densities N_1 at (i_1, j_1) and N_2 at (i_2, j_2). Next when $\tau \neq 0$, the autocorrelation function of the intensity image is given by

$$\begin{aligned} E[B_1^2, B_2^2, \tau] &= \int\int B_1^2 B_2^2 p(N_1 Spkl_1, N_2 Spkl_2, \tau)\mathrm{d}B_1 \mathrm{d}B_2 \\ &= \int\int N_1^2 N_2^2 \cdot (\int\int Spkl_1^2 Spkl_2^2 \cdot p(Spkl_1|N_1, Spkl_2|N_2, \tau) \\ &\quad \cdot \mathrm{d}Spkl_1 \mathrm{d}Spkl_2) \cdot p(N_1, N_2, \tau)\mathrm{d}N_1 \mathrm{d}N_2 \qquad (6.18) \\ &= \int\int N_1^2 N_2^2 \cdot \frac{1}{N_1}\frac{1}{N_2} \cdot p(N_1, N_2, \tau)\mathrm{d}N_1 \mathrm{d}N_2 \\ &= \int\int N_1 N_2 p(N_1, N_2, \tau)\mathrm{d}N_1 \mathrm{d}N_2 = R^{(N)}(\tau) \end{aligned}$$

In the derivation of Equation (6.18), we made two assumptions. First, the probability function $p(N_1 Spkl_1, N_2 Spkl_2, \tau)$ is separable into $p(N_1, N_2, \tau)p(Spkl_1|N1, Spkl_2|N2, \tau)$.

Secondly, the speckle values of different pixels are uncorrelated, therefore,

$$p(Spkl_1|N1, Spkl_2|N2, \tau) = p(Spkl_1|N1) \cdot p(Spkl_2|N2) \tag{6.19}$$

From all above, we come to the conclusions:

① The average scatterer density of target can be obtained by the average of intensity image $E[B^2]$.

② When $\tau \neq 0$, the autocorrelation function of the target density $R^{(N)}(\tau)$ is that of the intensity image $E[B_1^2, B_2^2, \tau]$.

③ When $\tau = 0$, the autocorrelation function of the target density is half the value of the mean square of the intensity image $E[B^4]$.

Now, all the statistics to solve the correlation length can be estimated from the backscattering images. We are pleased to see that the images preserve the autocorrelation properties of the target in the idealistic cases. The conclusion can be verified by the multiplicative SAR image model in Chapter V for the case of uncorrelated speckles among pixels.

6.2.3 Real SAR Image Texture Model

In the previous section, we investigate the image correlation function for the ideal SAR image model. However, the practical signal processing of SAR systems complicates the properties of SAR speckle and texture.

The aperture of the SAR antenna over a target is not infinite and it transmits and receives signals with limited bandwidth. Therefore, the SAR image of a point target is blurred by a point spread function (psf). Using the two-dimensional Fourier transform SAR processing algorithms, we could approximate a rectangular bandwidth support for the fast-time and slow-time domain. Fast-time domain represents

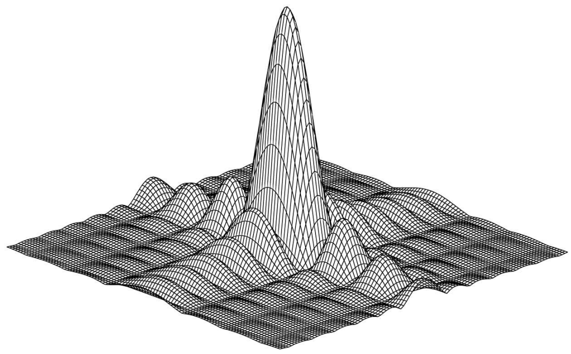

Figure 6.5: Shape of the point spread function by a rectangular bandwidth support region

the range identification and slow-time domain represents the azimuth discrimination [78] of a SAR processor. An analytical model for the point spread function can be approximated by use of the inverse 2-D Fourier transform.

Given the rectangular bandwidth support region of the SAR as B_r for the fast-time and B_y for the slow-time. The inverse Fourier transform takes the form of separable 2-D sinc functions in the range and azimuth (r, y) domain. Figure 6.5 shows the shape of the psf.

$$\mathrm{psf}(r, y) = \mathrm{sinc}\left(\frac{B_r r}{2\pi}\right) \mathrm{sinc}\left(\frac{B_y y}{2\pi}\right) \tag{6.20}$$

We usually define the SAR image resolution as the main lobes of the two sinc functions in the range and azimuth (r, y) domain respectively. They can be written as

$$D_r = \frac{2\pi}{B_r} \qquad D_y = \frac{2\pi}{B_y} \tag{6.21}$$

Let $S(r, y)$ represent a target composed of N isotropic point scatterers. For each scatterer, its backscattering coefficient is s_n and its range and azimuth position with respect to the antenna is (r_n, y_n)

$$S(r, y) = \sum_{n=1}^{N} s_n \delta(r_n, y_n) \tag{6.22}$$

The backscattered SAR image $B(r, y)$ can be written as the convolution of the target and a function PSF. PSF includes the amplitude of the psf in Equation 6.20 and the phase delay $\phi_n(r, y)$ caused by the round trip between the scatterer and the antenna.

$$B(r, y) = S(r, y) * \mathrm{PSF}(r, y) = \sum_{n=1}^{N} s_n e^{\mathrm{j}\phi_n(r,y)} \mathrm{psf}(r - r_n, y - y_n) \tag{6.23}$$

After the discrete sampling, we get a 2-D discrete image presentation

$$B(i, j) = \sum_{n=1}^{N} s_n e^{j\phi_n(i\Delta r, j\Delta y)} \mathrm{psf}(i\Delta r - r_n, j\Delta y - y_n) \tag{6.24}$$

The ideal case is when the amplitude point spread function is a delta function

$$\mathrm{psf}(i\Delta r - r_n, j\Delta y - y_n) = \begin{cases} 1 \quad : & \begin{array}{l} 0 \le i\Delta r - r_n < \Delta r \quad \& \\ 0 \le i\Delta y - y_n < \Delta y \end{array} \\ 0 \quad : & otherwise \end{cases} \tag{6.25}$$

The condition for the psf > 0 in Equation (6.25) can be written as

$$i \le \frac{r_n}{\Delta r} < i + 1 \quad , \quad j \le \frac{y_n}{\Delta y} < j + 1 \tag{6.26}$$

We define

$$i_n = \lfloor (\frac{r_n}{\Delta r}) \rfloor \quad , \quad j_n = \lfloor (\frac{y_n}{\Delta y}) \rfloor \tag{6.27}$$

where $\lfloor \quad \rfloor$ gives the largest integer less than or equal to the the value of the argument. Then the ideal psf has the concise form of

$$\mathrm{psf}(i\Delta r - r_n, j\Delta y - y_n) = \delta(i - i_n, j - j_n) \tag{6.28}$$

So the image by the ideal SAR system is given by

$$B(i, j) = \sum_{n=1}^{N} s_n e^{j\phi_n(i,j)} \delta(i - i_n, j - j_n) \tag{6.29}$$

At a fixed pixel (i_1, j_1), only the scatterers belonging to the resolution cell contribute to the backscattering signal for the pixel

$$\begin{aligned} B(i_1, j_1) &= \sum_{n=1}^{N} s_n e^{j\phi_n(i_1,j_1)} \delta(i_1 - i_n, j_1 - j_n) \\ &= \sum_{m=1}^{M} s_m e^{j\phi_m(i_1,j_1)} \end{aligned} \tag{6.30}$$

Where M is number of scatterers contributing to pixel (i_1, j_1). The phase delay ϕ_m is uniformly distributed in the range of $[-\pi, \pi)$. Equation (6.30) gives us the same result for the ideal case of SAR image model as in the previous section.

For the real SAR image, the shifted psf of scatterer s_n is obtained by taking the form

$$\mathrm{psf}(r - r_n, y - y_n) = \mathrm{sinc}(\frac{r - r_n}{Dr})\mathrm{sinc}(\frac{y - y_n}{Dy}) \tag{6.31}$$

The discretely sampled version is written by Equation (6.32) and Figure 6.6 illustrates the sampling of a shifted psf in one direction.

$$\mathrm{psf}(i-i_n, j-j_n) = \sum_{ii=-\infty}^{\infty} \sum_{jj=-\infty}^{\infty} \mathrm{sinc}(\frac{ii\Delta r - r_n}{Dr})\mathrm{sinc}(\frac{jj\Delta y - y_n}{Dy})\delta(i-ii, j-jj) \tag{6.32}$$

In theory, one scatterer has the effects on the whole image because of the point spread function. The backscattered image is

$$\begin{aligned} B(i,j) &= \sum_{n=1}^{N} s_n e^{j\phi_n(i,j)} \\ &\cdot \left[\sum_{ii=-\infty}^{\infty} \sum_{jj=-\infty}^{\infty} \mathrm{sinc}(\frac{(ii + i_n)\Delta r - r_n}{Dr})\mathrm{sinc}(\frac{(jj + j_n)\Delta y - y_n}{Dy})\delta(i - ii - i_n, j - jj - j_n) \right] \end{aligned} \tag{6.33}$$

As seen from Figure 6.5, most energy of the psf is concentrated in the main lobe, practically, we disregard the tail of the surface and choose a small neighborhood of samples around the center. The sampling scheme of most SAR systems uses the

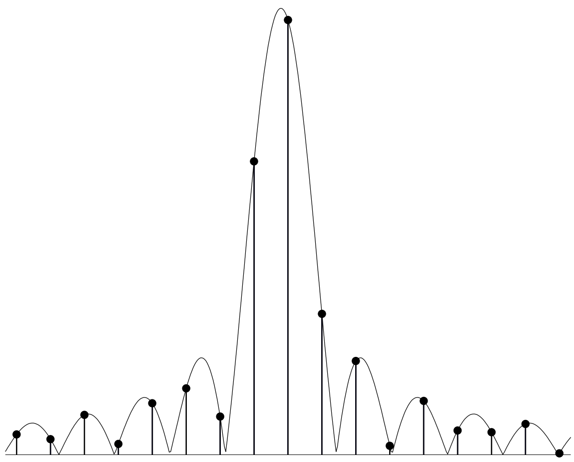

Figure 6.6: Sampling of a shifted point spread function in one direction

conventional estimation of the bandwidths and the main lobe will approximately cover a 3×3 pixel neighborhood.

Figure 6.7(a) is a simulated chirp pulse SAR logarithmic image of an isotropic point scatterer using the wave front reconstruction algorithm. The image is free of speckle. Figure 6.7(b) shows its correlation function. The SAR resolution of the image is $7.5m \times 6m$ and the pixel size is $2.43m \times 2.56m$. The figure shows that even the backscattered image of a single scatterer has a non-zero correlation function. Therefore, to acquire the full knowledge of real SAR image texture and speckle, a SAR texture simulator employing the similar but more realistic coherent summation algorithm is used to simulate SAR images of various target textures, as in the next section.

6.3 SAR Texture Simulator And Results

6.3.1 Coherent SAR Simulator

Soumekh in [78] presented the principles and algorithms to model SAR system, simulate SAR backscattering data, reconstruct image by means of 2-D Fourier array

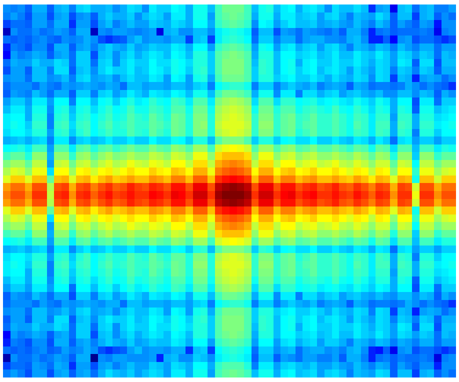

(a)

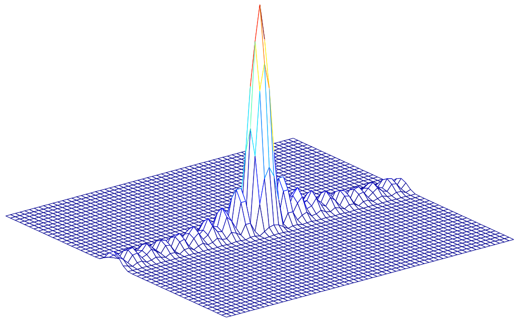

(b)

Figure 6.7: SAR image of a point scatterer

imaging [77], the matlab algorithms and numerical examples were also provided. Our texture simulator adapted the matlab code of stripmap SAR system and 2-D Fourier matched filtering and interpolation reconstruction method in [78] to a FORTRAN program. The simulator also integrates many types of scatterer distributions to form different texture of the ground. A large number of point scatterers with different scattering properties can be either randomly distributed in a 3-D space above the ground or obeying some rules such as regular lattice, rough surface or manually inputted. The 3-D target space is divided into bricks and Foldy's approximation [22] on the multiple scattering waves by randomly distributed scatterers is used in the model to calculated the electric field transmission matrix for each brick. The program records the path of incident and scattered wave by every scatterer and applies the corresponding transmission matrices. The coherent summation of the scattered fields by all the scatterers within a resolution cell is the simulator's output for one pixels. The SAR image scattered by a forest area can therefore be simulated by model the 3-D space of building bricks enclosing discrete scatterers. The geometry of a

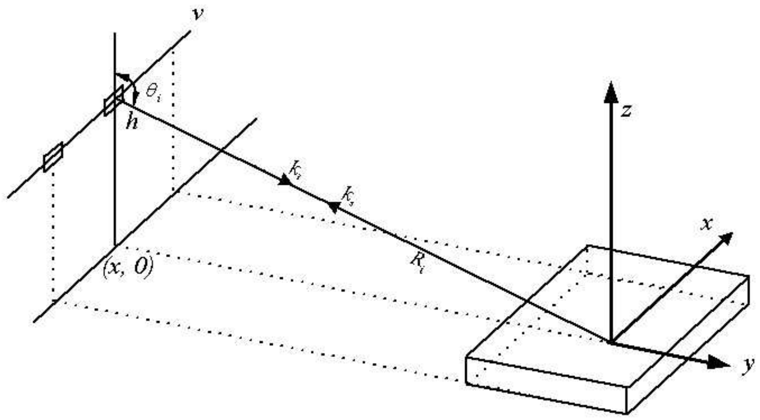

Figure 6.8: Geometry of the stripmode SAR simulator. A 3-D space target is defined by boundaries and the coordinate system is originated at target's center projected to the ground.

side-looking SAR system is illustrated in Figure 6.8. SAR moves at speed v in $+y$-direction at h above the ground and illuminates the target by right-hand side looking. The origin of the far field coordinate system is at the center of the ground projected target surface. The incidence angle of the wave from the antenna to the origin is θ_i.

$$\begin{aligned} z &= h \\ x &= -z \tan \theta_i \end{aligned} \tag{6.34}$$

The major shortcoming of coherent simulator is the heavy task in computing the backscattering signal of many scatterers. To get high fidelity simulation results, ground targets usually consists of tens of thousands singles scatterers. It can easily take a day or more to simulate one image of the scene using a PC.

In this section, for the interest of surface texture, we use only one type isotropic point scatterers that are located on the ground surface rather than a 3-D space, the density of scatterers is a function of their positions, which corresponds the scattering strength variations received by the antenna, as the indication of target texture. A chirp radar signal is transmitted by the antenna and the SAR system is configured by the following parameters.

Carrier frequency $f_c = 5.298$ GHz	Chirp bandwidth $f_0 = 20$ MHz
Chirp duration= 33.8 us	Antenna aperture = 12 m
Radar position = (-124.7, 0, 216) km	Target area = 300×100 m^2
Slant range resolution $D_x = 7.50$ m	Azimuth resolution $D_y = 6.0$ m
Slant Range Samples = 1672	Azimuth samples = 984
Slant range pixel size $d_x = 2.43$ m	Azimuth pixel size $d_y = 2.56$ m
Image range pixels $n_x = 62$	Image azimuth pixels $n_y = 48$

6.3.2 Texture Simulation Result

6.3.2.1 Homogeneous surface

One application of the SAR texture simulator is to test the statistical speckle model that has been long used for SAR image analysis, which can be accomplished by simulating the SAR image of a homogeneous surface composed by randomly distributed point scatterers. A scatterer map is generated by projecting the homogeneous surface to the slant range surface and is shown in Figure 6.9. The total number of the scatterers is 25520 and the mean density is 10 scatterers per pixel or 1.60 per m^2. As shown in Figure 6.4, the signal returned by 10 random scatterers have speckle characteristics. If we define the point backscattering coefficient σ^0 of every point scatterer is 1, the average backscattering coefficient of this area extended target is 1.60 per m^2.

Figure 6.10 is the simulated image $A_h(i, j)$ for this scene, it is in amplitude format and visually enhanced by histogram equalization. The 0dB calibration image $A_{cal}(i, j)$ (Figure 6.7(a)) is generated by simulating the SAR signal of single scatterer whose backscattering coefficient σ^0 is 1 and located in the center of the scene. The resulting image is also in amplitude format and the calibration factor is the summa-

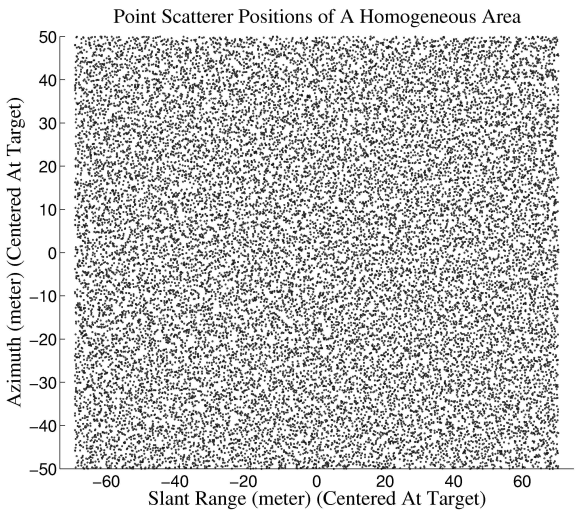

(a) Whole area

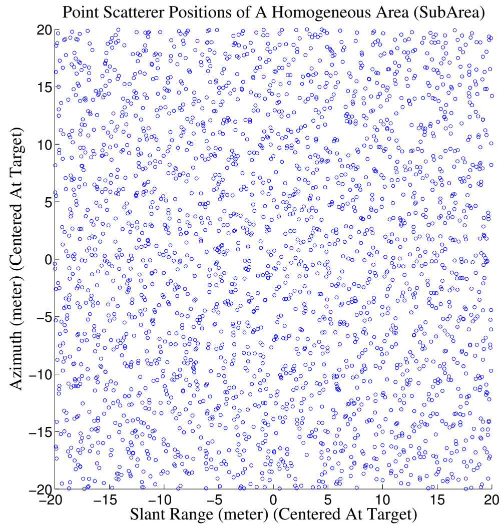

(b) Full resolution

Figure 6.9: A homogeneous surface with randomly distributed point scatterers. Horizontal direction: Slant Range, Vertical Direction: Azimuth.

tion over all the pixel values of the intensity image $I_{cal}(i,j)$, which is the squared amplitude image.

$$f_{cal} = \sum_{i=0}^{n_x}\sum_{j=0}^{n_y} I_{cal}(i,j) = \sum_{i=0}^{n_x}\sum_{j=0}^{n_y} A_{cal}^2(i,j) \tag{6.35}$$

Where i and j are the pixel indexes in the slant range and azimuth direction, respectivrluy. $n_x = 62$ and $n_y = 48$ are the range and azimuth samples given by the previous section.

The calibrated intensity image $I_h(i,j)$ of the homogeneous surface is obtained by dividing the squared amplitude image by the calibration factor $I_h(i,j) = \frac{A_h^2(i,j)}{f_{cal}}$. The calibrated intensity image shows that the mean scattering coefficient of the image is 1.58 per m^2, very close to the real scene's σ^0 of 1.60 per m^2. The maximum σ^0 is 14.56 and the minimum σ^0 is almost 0. The variance of σ^0 over the entire image is 3.05, which indicates the contrast of the image $\frac{\sqrt{Var[I_h(i,j)]}}{E[I_h(i,j)]} = 1.10$. In this example, normalized intensity image $\frac{I_h(i,j)}{E[I_h(i,j)]}$ can be called speckle, whose histogram

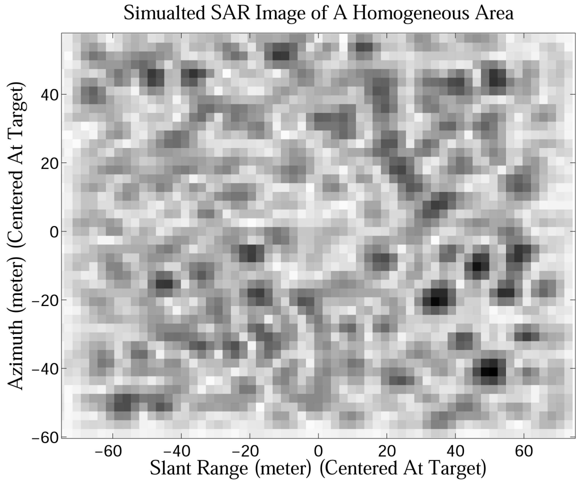

Figure 6.10: Simulated image for the homogeneous surface with randomly distributed point scatterers. Image size: 62×48. Horizontal direction: Slant Range, Vertical Direction: Azimuth.

is shown in Figure 6.11(a). Statistical SAR image model assumes that single-look SAR image speckle has a negative exponential pdf with mean and variance are both 1, which is also shown in Figure 6.11(a) for comparison. The consistency between two histograms demonstrates that the first order SAR speckle model is correct and can be safely used for SAR image analysis.

However, for the second order statistics, the simulated speckle are correlated among pixels, its correlation coefficients are shown in Figure 6.11(b). The correlation length of the image is estimated to be 4 m or 1.6 pixels. Which is contradictory to the statistical model, which assumes speckles are uncorrelated, thus no correlation length. The reason for this discrepancy is contributed to ideal conditions used in the statistical model. Although direct coherent approach used by our simulator can provide accurate and detailed information of the target, its computation is very time consuming, sometimes, statistic speckle model is preferred to study the large scaled overall scattering properties of the target for the simplicity and speed. However for texture analysis of real SAR data, which are second or higher order statistics,

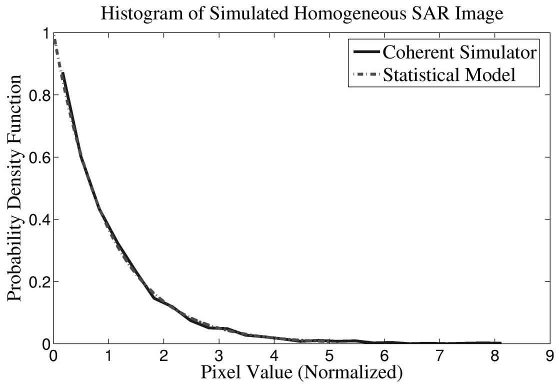

(a) Histogram

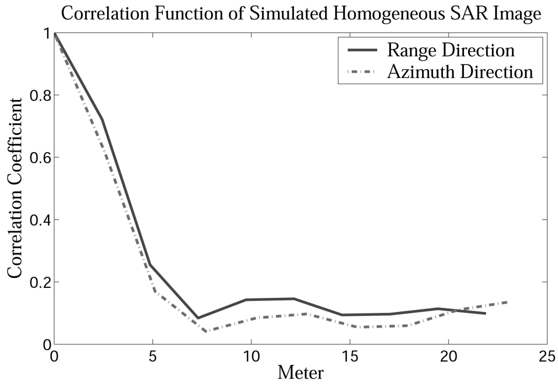

(b) Correlation coefficients

Figure 6.11: Histogram and correlation coefficients of the normalized intensity image for the homogeneous surface.

correlation of speckles is inevitable and can't be neglected.

6.3.2.2 Gaussian rough surface

In this section, image of a Gaussian rough surface is simulated to study how target's texture is captured by SAR data. The term "rough surface" doesn't represent the height fluctuation of the surface, instead, it indicates the scatterer density fluctuation. The density of scatterers placed on the ground is a function of positions, which has a Gaussian correlation function and the correlation length is 3 m in the ground range - azimuth coordinates. Figure 6.12 shows the scatterer distribution in the projected slant range surface. The total number of the scatterers is 29800 and the mean density is 11 scatterers per pixel or 1.61 per m^2. Thus, the average backscattering coefficient of this area extended target is 1.61 per m^2. Since the number of scatterers is directly related to the scattering strength, we consider the spatial variation of the scatterer density as the intrinsic scene texture.

The simulated amplitude image $A_G(i,j)$ for the rough surface is given in Figure 6.13. The noise-like image doesn't correspond directly to the scatterer map shown

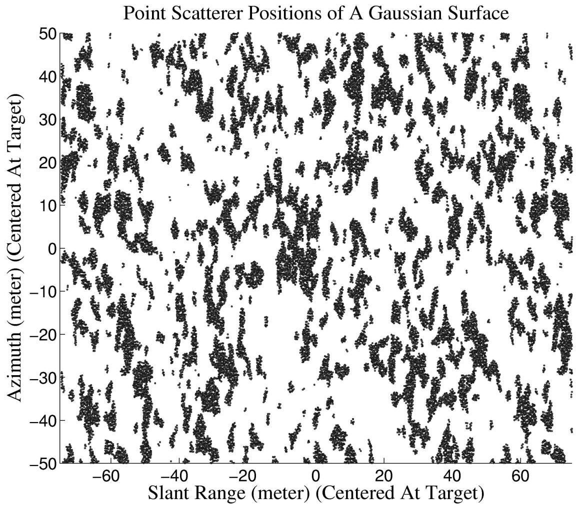

(a) Whole area

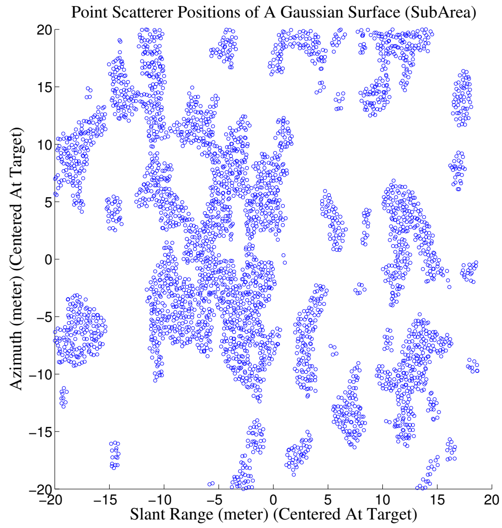

(b) Full resolution

Figure 6.12: A rough surface with randomly distributed point scatterers. Horizontal direction: Slant Range, Vertical Direction: Azimuth.

in Figure 6.12 since the scene texture is buried under the speckle.

Further analysis on the calibrate intensity images $I_G(i,j) = \frac{A_G^2(i,j)}{f_{cal}}$ indicates that the mean scattering coefficient of the image is 1.67 per m^2 while the average scene's σ^0 is 1.61 per m^2. The maximum and minimum σ^0 are 21 and 0 respectively. The variance of σ^0 over the entire image is 3.05, and the image's contrast is $\frac{\sqrt{Var[I_G(i,j)]}}{E[I_G(i,j)]} = 1.49$. Histogram of the normalized intensity image is shown in Figure 6.14(a), compared with the statistical single-looking speckle model's pdf. There are obvious differences between the two curves, which suggest the presence of target texture.

Figure 6.14(b) presents the correlation coefficient of $I_G(i,j)$ for the rough surface, whose correlation length of the image is estimated to be 5 m or two pixels. The blind deconvolution presented in Chapter V can be applied to this image to estimate the scene's correlation length from the simulated image, however, more pixels are needed

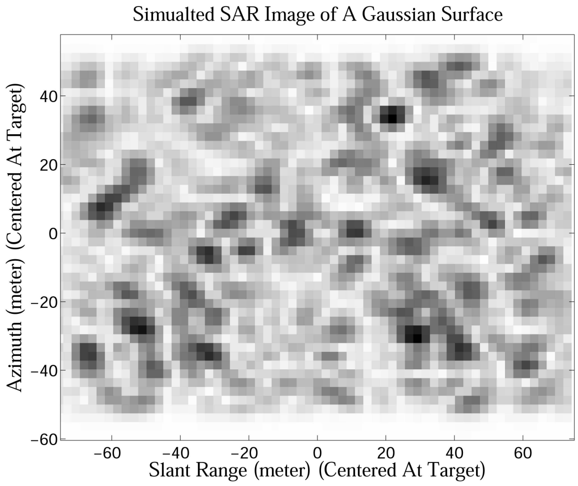

Figure 6.13: Simulated image for the Gaussian rough surface. Image size: 62×48. Horizontal direction: Slant Range, Vertical Direction: Azimuth.

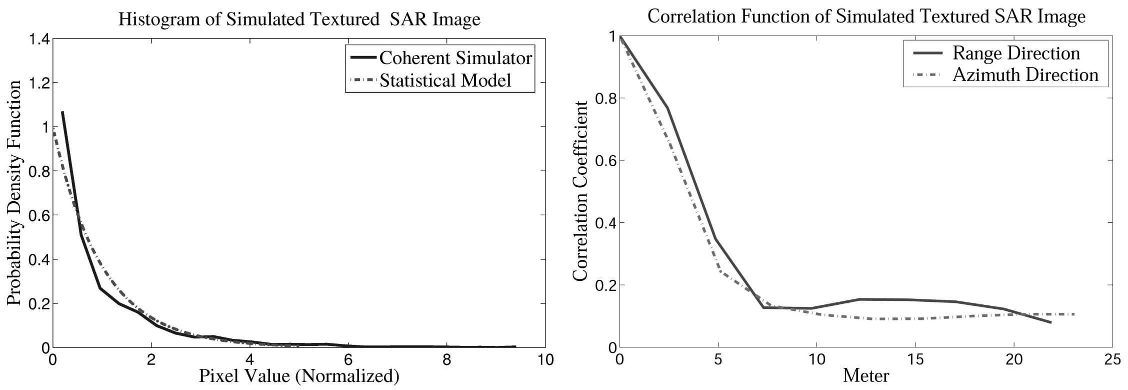

(a) Histogram

(b) Correlation coefficients

Figure 6.14: Histogram and correlation coefficients of the normalized intensity image for the Gaussian rough surface.

for high fidelity estimation. This is the future work for the combined application of the SAR texture simulator and blind deconvolution method, particularly, the SAR texture simulator need to increase the speed for any practical usage, which is usual achieved by using approximation and interpolation to reduce the samples to simulate the Fourier domain signal.

6.4 Discussion and Summary

We investigate the formation of texture and the ideal SAR model of texture and speckle are derived. SAR images preserve the autocorrelation properties of the target in the idealistic cases even with the presence of the speckle. However, a coherent SAR texture simulator is developed to simulate real SAR systems. The texture simulator uses the fundamental scattering theory, where the backscattering from individual scatterers are added up coherently in phase, as stated by the principles of basic radar systems. Multiple scattering among random scatterers are not considered at this moment. A SAR system of chirp radar signal and the wave front reconstruction reconstruction algorithm are is to simulate real life SAR images. Two images of targets representing general textures are simulated, one is a homogeneous surface and the other one is a Gaussian rough surface. The simulated images correctly reflect the overall properties of the scenes. The correlation function calculated for the homogeneous scene's image shows that the statistical model of SAR speckle is insufficient for texture analysis. The image with both the scene texture and speckle is difficult to interpret by visualization, texture preserving techniques such as blind deconvolution method and specking filters are needed. The texture simulator provides a power tool to study how the information about spatial distribution of the target can be extracted from SAR image. The input target of the model can be specified by any distributions of single scatterers. The model is capable of 3-D simulation with the Foldy's approximation for scattering by random media, but not applied in our work since it involves many additional tasks and is left for future work.

Chapter VII

CONCLUSION AND FUTURE WORK

7.1 Conclusion

This dissertation presented the microwave scattering models for nonuniform forest canopies, which addresses two aspects of nonuniform forest structures — vertical inhomogeneity of mixed species forests and texture information carried by SAR images of nonuniform canopies.

Bi-MIMICS has been developed to simulate bistatic scattering coefficients from forest canopies using radiative transfer theory. It is based on the backscattering canopy model MIMICS and is a first order full polarimetric model. We contribute to the development of Bi-MIMICS by introducing additional radar view angles and new scattering mechanisms, wave propagating quantities, and implementing the model. Bistatic scattering coefficients provides more information about the mechanisms of canopy scattering and composition compared to the backscattering coefficient, the advantage of the bistatic geometry is analyzed and demonstrated by model simulations, where σ^0 simulated different combination of incidence and scattering angles shows more sensitivity to some forest parameters such as stem orientation, biomass density. Bi-MIMICS is also a intermediate model that extends MIMICS and the same bistatic configuration is included in Multi-MIMICS.

The major contribution of the thesis is the development of Multi-MIMICS for mixed species forests. A multi-layer canopy structures is defined above the ground and two important forms of natural forests — overlapping layers and tapered trunks are specially treated. The model solves first order multi-layer radiative transfer equations using an iterative approach and diffuse boundary conditions. It also accommodates the ability of bistatic scattering simulation. Multi-MIMICS has been parameterized using ground collected forest inventory data of mixed species forest, simulation results correspond well with actual AIRSAR measurement, which also show improvement for complex forests over conventional two-layer scattering models. Overall, Multi-MIMICS provides a more effective scattering model for simulating SAR σ^0 from forests of mixed species and structural, the model still has built-in restrictions on multiple scattering mechanism among scatterers, the coherent effects, error for cross-polarization because it is only a first order RT-based model.

For nonuniform canopies, texture information carried by the SAR image reveals the spatial variation of the scene. Image correlation length is suggested as an optimal texture model for SAR images. A blind deconvolution method is presented to estimate the correlation length of target texture from the speckle degraded images. Utilizing texture information can help improve the land-cover category classification accuracy since some categories' SAR images may show the same mean value but different texture parameter.

A coherent SAR texture simulator is developed to simulate SAR images of surface targets' horizontal spatial variation. The model is a reliable source to study the texture from nonuniform forests, especially when the ground truth is unavoidable, where high fidelity simulation results is desired. The disadvantage of the coherent SAR simulator is its heavy commutating tasks.

7.2 Recommendations For Future Work

Several aspects of the future work of this thesis are considered as the extension and improvement of the current study. For the validation of Bi-MIMICS model, the lack of actual bistatic SAR measurement data from vegetation for us to comparison with the model's simulation arises as a major problem. For this reason, we have proposed some future work including conducting laboratory bistatic radar measurements on scaled forest models using our existing bistatic measurement facilities.

In studying Multi-MIMICS's simulated backscattering for mixed species forests, some discrepancies between the simulation and radar measurement, have been observed due to the model's limitation. Extending the current first order RT solution of Multi-MIMICS to higher order solutions can include the multiple scattering mechanisms among canopy elements, particularly at high frequencies, where branch and foliage volume scattering dominates and account for the underestimation of σ^0 by the current model. The scattering models for individual canopy compositions and the rough ground surface can also be refined since they are most accurate at L-band. Other scattering models are needed for much lower and higher frequencies.

Currently, using the blind deconvolution method to estimate real target texture's correlation length from speckle degraded SAR images is only applied to simulated images because no detailed ground truth have been available. Which in turn requires the coherent SAR texture simulator to provide high resolution simulations for real nonuniform forest scenes. Improving the speed of the simulator by incorporating some statistical models for approximation is part of future work.

Model inversion is a important aspects of the future work. The ultimate goal for developing scattering models is to improve the potential retrieval of forest biomass and other vegetation parameters. Multi-MIMICS inversion model is expected to provide estimates of soil moisture, canopy biomass, and the possibility to detect the multi-layer structure of canopies with mixed species.

BIBLIOGRAPHY

BIBLIOGRAPHY

[1] "The marrakesh accords and the marrakesh declaration," *Proceedings of the Seventh Conference of the Parties (COP 7), Marrakesh, Morocco.*, vol. Annex, Section A, Oct. 2001.

[2] D. S. Alves, J. L. G. Pereira, C. L. D. Sousa, J. Soares, and F. Yamaguchi, "Characterizing landscape changes in central rondonia using landsat tm imagery," *Int. J. Remote Sensing*, vol. 20, no. 14, pp. 2877–2882, Sept. 1999.

[3] J. M. Austin, B. G. Mackey, and K. P. V. Niel, "Estimating forest biomass using satellite radar: an exploratory study in a temperate Australian," *For. Ecol. Manage.*, vol. 175, no. 1-3, pp. 575–585, Mar. 2003.

[4] C. G. Brown, "Tree height estimation using shuttle radar topography mission and ancillary data," Ph.D. dissertation, The University of Michigan, Ann Arbor, Michigan, 2003.

[5] R. J. Burkholder, L. J. Gupta, and J. T. Johnson, "Comparison of monostatic and bistatic radar images," *IEEE Antennas Propagat. Mag.*, vol. 45, no. 3, pp. 41–50, June 2003.

[6] W. H. Burrows, M. B. Hoffmann, J. F. Compton, and P. V. Back, "Allometric relationships and community biomass stocks in white cypress pine (callitris glaucophylla) and associated eucalypts of the carnarvon area - south central Queensland," Australian Greenhouse Office, Canberra, Tech. Rep. 33, Feb. 2001.

[7] R. A. Butler, *A Place Out of Time: Tropical Rainforests and the Perils They Face*, San Francisco, CA, Unpublished, http://www.mongabay.com.

[8] S. Chandrasekhar, *Radiative Transfer.* New York: Dover Publications, 1960.

[9] N. S. Chauhan, R. H. Lang, and K. J. Ranson, "Radar modeling of a boreal forest," *IEEE Trans. Geosci. Remote Sensing*, vol. 29, no. 4, pp. 627–638, July 1991.

[10] R. Chellappa, "Two-dimensional discrete Gaussian Markov random field models for image processing," *J. Inst. Electron. Telecommun. Eng.*, vol. 2, no. 2, pp. 113–119, Mar-Apr 1989.

[11] J. C. Dainty, *Laser Speckle and Related Phenomena.* New York: Springer-Verlag, 2001.

[12] M. Datcu, K. Seidel, and M. Walessa, "Spatial information retrieval from remote-sensing images - Part I: Information theoretical perspective," *IEEE Trans. Geosci. Remote Sensing*, vol. 36, no. 5, pp. 1431–1445, Sept. 1998.

[13] R. De Roo, "A polarimetric radar image simulator for microwave and millimeter-wave sensors," The University of Michigan, Ann Arbor, Michigan, Tech. Rep., 1996.

[14] ——, "Theory and measurement of bistatic scattering of X-band microwaves from rough dielectric surfaces," Ph.D. dissertation, The University of Michigan, Ann Arbor, Michigan, 1996.

[15] H. Derin and H. Elliott, "Modeling and segmentation of noisy and textured images uing gibbs random fields," *IEEE Trans. Pattern Anal. Machine Intell.*, vol. 9, no. 1, pp. 39–55, Jan. 1997.

[16] M. C. Dobson, K. McDonald, and F. T. Ulaby, "Modeling of forest canopies and analyses of polarimetric SAR data," The University of Michigan, Ann Arbor, Michigan, Tech. Rep. 026143-1-F, 1989.

[17] M. C. Dobson, L. Pierce, J. Kellndorfer, and F. Ulaby, "Use of SAR image texture in terrain classification," in *Int. Geosci. Remote Sens. Symp.*, vol. 3, Sept. 1997, pp. 1180–1183.

[18] M. C. Dobson, F. T. Ulaby, T. Le Toan, A. Beaudoin, E. S. Kasischke, and N. Christensen, "Dependence of radar backscatter on coniferous forest biomass," *IEEE Trans. Geosci. Remote Sensing*, vol. 30, no. 2, pp. 412–415, Mar. 1992.

[19] S. L. Durden, J. J. V. Zyl, and H. A. Zebker, "Modeling and observation of the radar polarization signature of forested areas," *IEEE Trans. Geosci. Remote Sensing*, vol. 27, no. 3, pp. 290–301, May 1989.

[20] R. L. Eigel Jr., P. J. Collins, J. Andrew J. Terzuoli, G. Nesti, and J. Fortuny, "Bistatic scattering characterization of complex objects," *IEEE Trans. Geosci. Remote Sensing*, vol. 38, no. 5, pp. 2078–2092, Sept. 2000.

[21] J. Flusser and T. Suk, "Degraded image analysis: An invariant approach," *IEEE Trans. Pattern Anal. Machine Intell.*, vol. 20, no. 6, pp. 590–603, June 1998.

[22] L. L. Foldy, "The multiple scattering of waves. I. General theory of isotropic scattering by randomly distributed scatterers," *Phys. Rev.*, vol. 67, no. 3-4, pp. 107–119, Feb. 1945.

[23] V. S. Frost, J. A. Stiles, K. S. Shanmugan, and J. C. Holtzman, "A model for radar images and its application to adaptive digital filtering of multiplicative

noise," *IEEE Trans. Pattern Anal. Machine Intell.*, vol. 4, no. 2, pp. 157–166, Mar. 1982.

[24] S. Geman and D. Geman, "Stochastic relaxation, Gibbs distributions and the Bayesian Restoration of images," *IEEE Trans. Pattern Anal. Machine Intell.*, vol. 6, no. 6, pp. 721–745, Nov. 1984.

[25] J. W. Goodman, *Statistical Properties of Laser Speckle Patterns.* Heidelberg, Germany: Springer-Verlag, 1980.

[26] H. D. Griffiths, C. J. Baker, J. Baubert, N. Kitchen, and M. Treagust, "Bistatic radar using satellite-borne illuminators," *Radar*, pp. 1–5, Oct. 2002.

[27] W. Hagg and M. Sties, "Efficient speckle filtering of SAR images," in *Int. Geosci. Remote Sens. Symp.*, vol. 3, Pasadena, CA, USA, Aug. 1994, pp. 2140–2142.

[28] R. M. Haralic, "Statistic and structural approaches to texture," *Proceedings of the IEEE*, vol. 67, pp. 786–804, May 1979.

[29] G. Harrington, "Estimation of above ground biomass of trees and shrubs in eucalyptus populnea (F. Muell.) woodland by regression of mass on trunk diameter and plant height," *Aust. J. Bot.*, vol. 2, pp. 135–143, 1979.

[30] B. Hauck, F. Ulaby, and R. DeRoo, "Polarimetric bistatic-measurement facility for point and distributed targets," *IEEE Antennas Propagat. Mag.*, vol. 40, no. 1, pp. 31–41, Feb. 1998.

[31] B. K. P. Horn, *Robot Vision.* New York: McGraw-Hill, 1986.

[32] R. A. Houghton, "Global effects of tropical deforestation," *Environmental Science and Technology*, vol. 24, no. 4, Apr. 1998.

[33] M. L. Imhoff, "Theoretical analysis of the effect of forest structure on synthetic aperture radar backscatter and the remote sensing of biomass," *IEEE Trans. Geosci. Remote Sensing*, vol. 33, no. 2, pp. 341–352, Mar. 1992.

[34] M. A. Karam and A. K. Fung, "Electromagnetic scattering from a layer of finite length, randomly oriented, dielectric, circular cylinders over a rough interface with application to vegetation," *Int. J. Remote Sensing*, vol. 9, no. 6, pp. 1109–1134, June 1988.

[35] D. T. Kuan, A. A. Sawchuk, T. C. Strand, and P. Chavel, "Adaptive restoration of images with speckle," *IEEE Trans. Acoust., Speech, Signal Processing*, vol. ASSP-35, no. 3, pp. 373–382, Mar. 1987.

[36] D. Kundur and D. Hatzinakos, "Blind image deconvolution," *IEEE Signal Processing Magazine*, pp. 43–62, May 1996.

[37] T. Kurosu, S. Uratsuka, H. Maeno, and T. Kozu, "Texture statistics for classification of land use with multitemporal JERS-1 SAR single-look imagery," *IEEE Trans. Geosci. Remote Sensing*, vol. 1, no. 37, pp. 227–236, Jan. 1999.

[38] R. H. Lang and J. S. Sidhu, "Electromagnetic backscattering from a layer of vegetation: A discrete approach," *IEEE Trans. Geosci. Remote Sensing*, vol. 21, no. 1, pp. 177–186, Jan. 1993.

[39] N. F. Law and R. G. Lane, "Blind deconvolution using least squares minimization," *Optical Communications*, vol. 128, pp. 341–352, July 1996.

[40] T. Le Toan, A. Beaudoin, J. J. Riom, and D. Guyon, "Relating forest biomass to SAR data," *IEEE Trans. Geosci. Remote Sensing*, vol. 30, no. 2, pp. 403–411, Mar. 1992.

[41] J. S. Lee, "Speckle suppression and analysis for synthetic aperture radar images," *Optical Engineering*, vol. 25, no. 5, pp. 636–643, May 1986.

[42] S. Z. Li, *Markov random field modeling in image analysis.* New York: Springer, 2001.

[43] Y.-C. Lin, "A fractal-based coherent scattering and propagation model for forest canopies." Ph.D. dissertation, The University of Michigan, Ann Arbor, Michigan, 1997.

[44] Y.-C. Lin and K. Sarabandi, "Electromagnetic scattering model for a tree trunk above a tilted ground plane," *IEEE Trans. Geosci. Remote Sensing*, vol. 33, no. 4, pp. 1063–1070, July 1995.

[45] S. Y. Lu and K. S. Fu, "A syntactic approach to texture analysis," *Computer Graphics and Image Processing*, vol. 7, pp. 303–330, 1978.

[46] R. M. Lucas, A. Milne, N. Cronin, C. Witte, and R. Denhan, "The potential of synthetic aperture radar (SAR) for quantifying the biomass of Australia's woodlands," *The Rangeland Journal*, vol. 22, no. 1, pp. 124–140, 2000.

[47] R. M. Lucas, P. Tickle, A. Lee, J. Austin, C. Witte, K. Jones, N. Cronin, M. Moghaddam, and A. K. Milne, "Use of AIRSAR (POLSAR) data for quantifying the biomass of woodlands, Queensland, Australia," *AIRSAR Workshop*, Mar. 2002.

[48] R. Lucas and M. Moghaddam, "Microwave scattering from mixed species forest, Queensland, Australia," *IEEE Trans. Geosci. Remote Sensing*, In press.

[49] A. J. Luckman, J. R. Baker, M. Honzak, and R. Lucas, "Tropical forest biomass density estimation using JERS-1 SAR: Seasonal variation, confidence limits, and application to image mosaics," *Remote Sens. Environ.*, vol. 63, no. 2, pp. 126–139, Feb. 1998.

[50] K. C. McDonald, "Modeling microwave backscatter from tree canopies," Ph.D. dissertation, The University of Michigan, Ann Arbor, Michigan, 1991.

[51] K. C. McDonald, M. C. Dobson, and F. T. Ulaby, "Using MIMICS to model l-band multiangle and multitemporal backscatter from a walnut orchard," *IEEE Trans. Geosci. Remote Sensing*, vol. 28, no. 4, pp. 477–491, July 1990.

[52] ——, "Modeling multi-frequency diurnal backscatter from a walnut orchard," *IEEE Trans. Geosci. Remote Sensing*, vol. 29, no. 6, pp. 852–863, Nov. 1991.

[53] D. J. McLaughlin, Y. Wu, W. G. Stevens, X. Zhang, M. J. Sowa, and B. Weijers, "Fully polarimetric bistatic radar scattering behavior of forested hills," *IEEE Trans. Antennas Propagat.*, vol. 50, no. 2, pp. 101–100, Feb. 2002.

[54] G. M.Henebry and H. J. H. Kux, "Lacunarity as a texture measure for SAR imagery," *Int. J. Remote Sensing*, vol. 16, no. 3, pp. 565–571, Feb. 1995.

[55] M. Moghaddam, S. Durden, and H. Zebker, "Radar measurements of forested area during OTTER," *Remote Sens. Environ.*, vol. 47, no. 2, pp. 154–166, Feb. 1994.

[56] M. Moghaddam and S. S. Saatchi, "Monitoring tree moisture using an estimation algorithm applied to sar data from BOREAS," *IEEE Trans. Geosci. Remote Sensing*, vol. 37, no. 2, pp. 901–916, Mar. 1999.

[57] Z. Mou-Yan and R. Unbehauen, "New algorithms of two-dimensional blind deconvolution," *Optical Engineering*, vol. 34, no. 10, pp. 2945–2954, Oct. 1995.

[58] S. V. Nghicm, R. Kwok, S. I. Yueh, J. A. Kong, C. C. Hsu, M. A. Tassoudji, and R. T. Shin, "Polarimetric scattering from layered media with multiple species of scatterers," *Radio Science*, vol. 30, no. 4, pp. 835–852, Jul-Aug 1995.

[59] H. Noda, M. N. Shirazi, and E. Kawaguchi, "MRF-based texture segmentation using wavelet decomposed images," *Pattern Recognition*, vol. 35, pp. 771–782, 2002.

[60] C. J. Oliver, "Rain forest classification based on sar texture," *IEEE Trans. Geosci. Remote Sensing*, vol. 2, no. 38, pp. 1095–1104, Mar. 2000.

[61] C. J. Oliver and S. Quegan, *Understanding Synthetic Aperture Radar Images.* Norwood, Massachusetts: Artech House, 1998.

[62] G. Picard, T. L. Toan, S. Quegan, Y. Caraglio, and T. Castel, "Radiative transfer modeling of cross-polarized backscatter from a pine forest using the discrete ordinate and eigenvalue method," *IEEE Trans. Geosci. Remote Sensing*, vol. 42, no. 8, pp. 1720–1730, Aug. 2004.

[63] R. E. Plotnick, R. H. Gardner, and R. V. O'Neill, "Lacunarity indices as measure of landscape texture," *Landscape Ecology*, vol. 8, pp. 202–211, 1993.

[64] A. R. Rao, “A taxonomy for texture description and identification,” Ph.D. dissertation, The University of Michigan, Ann Arbor, Michigan, 1989.

[65] J. A. Richards, “Radar backscatter modeling of forests: A review of current trends,” *Int. J. Remote Sensing*, vol. 11, no. 7, pp. 1299–1312, July 1990.

[66] J. A. Richards, G. Q. Sun, and D. S. Simonett, “L-band radar backscattering modeling of forest stands,” *IEEE Trans. Geosci. Remote Sensing*, vol. 25, no. 4, pp. 487–498, July 1987.

[67] E. Rignot, W. A. Salas, and D. L. Skole, “Mapping deforestation and secondary growth in Rondonia, Brazil, using imaging radar and thematic mapper data,” *Remote Sens. Environ.*, vol. 59, no. 2, pp. 167–179, Feb. 1997.

[68] A. Rosenqvist, A. Milne, R. Lucas, M. Imhoff, and C. Dobson, “A review of remote sensing technology in support of the kyoto protocol,” *Environ. Sci. Policy*, vol. 6, no. 5, pp. 441–455, Oct. 2003.

[69] G. T. Ruck, D. E. Barrick, W. D. Stuart, and C. K. Krichbaum, *Radar Cross Section Handbook*. New York, NY: Plenum Press, 1970, vol. 1.

[70] S. S. Saatchi and M. Moghaddam, “Estimation of crown and stem water content and biomass of boreal forest using polarimetric SAR imagery,” *IEEE Trans. Geosci. Remote Sensing*, vol. 38, no. 2, pp. 697–709, Mar. 2000.

[71] S. S. Saatchi, D. M. L. Vine, and R. H. Lang, “Microwave backscattering and emission model for grass canopies,” *IEEE Trans. Geosci. Remote Sensing*, vol. 32, no. 1, pp. 177–186, Jan. 1994.

[72] S. S. Saatchi and K. C. McDonald, “Coherent effects in microwave backscattering models for forest canopies,” *IEEE Trans. Geosci. Remote Sensing*, vol. 35, no. 4, pp. 1032–1044, July 1997.

[73] K. Sarabandi and Y.-C. Lin, “Simulation of interferometric sar response for characterizing the scattering phase center statistics of fores canopies,” *IEEE Trans. Geosci. Remote Sensing*, vol. 38, no. 1, pp. 115–125, Jan. 2000.

[74] K. Sarabandi and A. Nashashibi, “A novel bistatic scattering matrix measurement technique using a monostatic radar,” *IEEE Trans. Antennas Propagat.*, vol. 44, no. 1, pp. 41–50, Jan. 1996.

[75] M. Schroder, H. Rehrauer, K. Seidel, and M. Datcu, “Spatial information retrieval from remote-sensing images - Part II: Gibbs-Markov random fields,” *IEEE Trans. Geosci. Remote Sensing*, vol. 36, no. 5, pp. 1446–1455, Sept. 1998.

[76] M. Soumekh, “Bistatic synthetic aperture radar inversion with application in dynamic object imaging,” *IEEE Trans. Signal Processing*, vol. 39, no. 9, pp. 2044–2055, Sept. 1991.

[77] ——, *Fourier Array Imaging.* Englewood Cliffs, N.J: Prentice Hall, 1994.

[78] ——, *Synthetic Aperture Radar Signal Processing.* New York: Wiley-Intersience, 1999.

[79] S. Stan, G. Palubinskas, and M. Datcu, “Bayesian selection of the neighborhood order of gauss markov texture models,” *Pattern Recong. Lett.*, vol. 23, pp. 1229–1238, 2002.

[80] G. Sun and K. J. Ranson, “A three-dimensional radar backscatter model of forest canopies,” *IEEE Trans. Geosci. Remote Sensing*, vol. 33, no. 2, pp. 373–382, Mar. 1995.

[81] G. Sun, D. S. Simonett, and A. H. Strahler, “A radar backscattering model for discontinuous coniferous forests,” *IEEE Trans. Geosci. Remote Sensing*, vol. 29, no. 4, pp. 639–650, July 1991.

[82] P. K. Tickle, A. Lee, R. M. Lucas, J. Austin, and C. Witte, “Quantifying Australian forest and woodland structure and biomass using large scale photography and small footprint LIDAR,” *Remote Sens. Environ.*, submitted.

[83] F. T. Ulaby, T. E. V. Deventer, J. R. East, T. F. Haddock, and M. E. Coluzzi, “Bistatic scattering characterization of complex objects,” *IEEE Trans. Geosci. Remote Sensing*, vol. 26, no. 3, pp. 229–243, May 1988.

[84] F. T. Ulaby, C. Elachi, and editors, *Radar Polarimetry for Geoscience Application.* Norwood, Massachusetts: Artech House, 1989.

[85] F. T. Ulaby, R. K. Moore, and A. K. Fung, *Microwave Remote Sensing: Active and passive, Vol. III: Volume Scattering and Emission Theory, Advanced System and Applications.* Dedham, Massachusetts: Artech House, 1986.

[86] F. T. Ulaby, K. Sarabandi, K. McDonald, M. Whitt, and M. C. Dobson, “Michigan microwave canopy scattering model (MIMICS),” The University of Michigan, Ann Arbor, Michigan, Tech. Rep. 022486-T-1, July 1988.

[87] H. Xie, “Multiresolution statistical techniques for synthetic aperture radar speckle reduction and image registration,” Ph.D. dissertation, The University of Michigan, Ann Arbor, Michigan, 2002.

[88] A. E. Yagle and S. Shah, “2-d blind deconvolution of even point spread-functions from compact support images,” in *Proc. IEEE Trans. Image Processing*, Submitted.

[89] D. Zahn and K. Sarabandi, “Simulation of bistatic scattering for assessing the application of existing communication satellites to remote sensing of rough surfaces,” in *Int. Geosci. Remote Sens. Symp.*, vol. 4, Honolulu, HI, USA, July 2000, pp. 1528–1530.